

## **CP Violation in tau to K\* Decays**

M. Hodgkinson

Stanford Linear Accelerator Center  
Stanford University  
Stanford, CA 94309

SLAC-Report-800

Prepared for the Department of Energy  
under contract number DE-AC02-76SF00515

Printed in the United States of America. Available from the National Technical Information Service, U.S. Department of Commerce, 5285 Port Royal Road, Springfield, VA 22161.

This document, and the material and data contained therein, was developed under sponsorship of the United States Government. Neither the United States nor the Department of Energy, nor the Leland Stanford Junior University, nor their employees, nor their respective contractors, subcontractors, or their employees, makes an warranty, express or implied, or assumes any liability of responsibility for accuracy, completeness or usefulness of any information, apparatus, product or process disclosed, or represents that its use will not infringe privately owned rights. Mention of any product, its manufacturer, or suppliers shall not, nor is it intended to, imply approval, disapproval, or fitness of any particular use. A royalty-free, nonexclusive right to use and disseminate same of whatsoever, is expressly reserved to the United States and the University.

# CP Violation in $\tau$ to $K^*$ Decays

Mark Hodgkinson



THE UNIVERSITY  
*of* MANCHESTER

Department of Physics and Astronomy High Energy Physics Group  
University of Manchester

2004

*Thesis submitted for the Degree of Doctor of Philosophy in the  
University of Manchester*

# Contents

Abstract . . . . .	13
Declaration . . . . .	14
The Author . . . . .	14
BaBar Disclaimer . . . . .	15
<b>Acknowledgements</b>	<b>16</b>
<b>1 Introduction</b>	<b>18</b>
<b>2 The Standard Model</b>	<b>20</b>
2.1 Quantum Electrodynamics . . . . .	20
2.2 Quantum Chromodynamics . . . . .	22
2.3 Weak Dynamics . . . . .	24

2.4	The Weinberg-Salam Electroweak Model . . . . .	25
2.5	The Gauge Boson Kinetic Energies and Self-Interactions . . . . .	26
2.6	The Lepton and Quark Kinetic Energies and their Couplings to the Gauge Bosons . . . . .	27
2.7	Gauge Boson Masses and Higgs Mass and Couplings . . . . .	28
2.8	Fermion Masses and Couplings to Higgs Boson . . . . .	30
2.9	Summary . . . . .	31
<b>3</b>	<b>C, P and CP Violation</b>	<b>32</b>
3.1	CP Violation in $K^0$ Mixing . . . . .	33
3.2	CP Violation in Kaon Decay . . . . .	36
3.3	The CKM Matrix . . . . .	39
<b>4</b>	<b>CP Violation Beyond the Standard Model</b>	<b>44</b>
4.1	Scalar Boson Models . . . . .	46
<b>5</b>	<b>Tau Lepton Physics</b>	<b>51</b>
5.1	CP Violation in Tau Production . . . . .	52
5.2	CP Violation in Tau Decays . . . . .	52

<b>6</b>	<b>Experimental Apparatus</b>	<b>57</b>
6.1	The Silicon Vertex Tracker (SVT) . . . . .	61
6.2	The Drift Chamber . . . . .	66
6.3	Charged Particle Tracking Performance . . . . .	70
6.4	Detector of Internally Reflected Cherenkov Light . . . . .	74
6.5	The Electromagnetic Calorimeter . . . . .	80
6.6	The Instrumental Flux Return Barrel (IFR) . . . . .	87
6.7	Trigger System . . . . .	93
6.8	Summary . . . . .	99
<b>7</b>	<b>The BaBar Software Framework</b>	<b>100</b>
7.1	Online Reconstruction Software . . . . .	101
7.2	Offline Analysis Software . . . . .	102
7.3	Simulation Software . . . . .	103
7.4	Summary . . . . .	104
<b>8</b>	<b>The kk2f Generator</b>	<b>105</b>
8.1	Summary . . . . .	110

<b>9</b>	<b>Event Selection</b>	<b>111</b>
9.1	Event Selection . . . . .	114
9.1.1	Signal Event Selection . . . . .	114
9.2	Cut Summary . . . . .	130
<b>10</b>	<b>Monte Carlo Corrections and the <math>K_S^0</math> Mass Spectrum</b>	<b>135</b>
10.1	PID Efficiency Corrections . . . . .	136
10.2	$K_S^0$ Efficiency Corrections . . . . .	136
10.3	Tracking Efficiency Corrections . . . . .	137
10.4	Total Correction . . . . .	137
10.5	Summary . . . . .	137
10.6	The $K_S^0\pi$ Mass Spectrum . . . . .	138
<b>11</b>	<b>CP Observable</b>	<b>140</b>
11.1	Summary . . . . .	143
<b>12</b>	<b>Systematic Checks</b>	<b>144</b>
12.1	Systematic Uncertainties on PID Weights . . . . .	144

12.2	Systematic Uncertainties on $K_S^0$ Corrections . . . . .	145
12.3	Systematic Uncertainty on $K_S^0$ Candidate Selection . . . . .	146
12.4	Errors on Tracking Efficiency Corrections . . . . .	147
12.5	Errors due to background subtraction . . . . .	147
12.6	Uncertainties due to Selection Criteria . . . . .	148
12.7	Errors on $c_1$ . . . . .	149
12.8	Summary . . . . .	150
<b>13</b>	<b>Measurement of CP Asymmetry</b>	<b>151</b>
<b>14</b>	<b>Conclusions</b>	<b>153</b>
<b>A</b>	<b>Calculation of CP Optimal Observable</b>	<b>155</b>
<b>B</b>	<b>Definitions of Nano Level TagBits</b>	<b>159</b>
	<b>Bibliography</b>	<b>161</b>

# List of Figures

2.1	Scaling of Coupling Constants with Energy . . . . .	26
3.1	The Unitarity Triangle . . . . .	42
4.1	Tau Decays via Vector and Scalar Bosons . . . . .	45
4.2	Higgs Diagrams . . . . .	50
6.1	Integrated Luminosity Collected by BaBar . . . . .	58
6.2	The PEP rings at SLAC . . . . .	60
6.3	The BaBar Detector . . . . .	61
6.4	The SVT Layers . . . . .	63
6.5	Longitudinal Cross-Section of SVT . . . . .	63
6.6	SVT Hit Resolution in (a) $z$ and (b) $\phi$ . . . . .	66
6.7	Longitudinal section of the DCH . . . . .	68

6.8	Measurement of $dE/dx$ as a function of track momenta . . . . .	69
6.9	Difference in Mass of $K\pi\pi$ and $K\pi$ systems for all events (points) and events in which the low momentum pion is reconstructed in both the SVT and DCH (histogram) . . . . .	72
6.10	Comparison of slow pion momentum spectrum in data and MC (a) and the SVT efficiency (b) . . . . .	73
6.11	Dependence of $d_0$ and $z_0$ on $p_t$ using multi-hadron events . . . . .	74
6.12	Geometry of the DIRC . . . . .	76
6.13	Pion/Kaon Separation in the DIRC as a function of momentum . . . . .	79
6.14	The measured energy resolution for various processes. . . . .	85
6.15	The measured angular resolution for various processes. . . . .	86
6.16	The reconstructed $\pi^0$ mass from two photons events in $B\bar{B}$ Monte Carlo . . . . .	87
6.17	The IFR: Barrel Sector and Forward and End Doors . . . . .	88
6.18	Cross section of Planar RPC . . . . .	89
6.19	Muon efficiency (left scale) and pion mis-id probability (right scale) as functions of momentum and polar angle. . . . .	92
6.20	Single track $z_0$ for all Level 1 tracks reconstructed by Level 3 . . . . .	97

8.1	Rho Resonance from a1 Decay . . . . .	107
8.2	Cosine of Opening Angle and Energy distributions weighted by Energy for Photons in KORALB(Red) and kk2f(Blue) . . . . .	107
8.3	Cosine of Theta and Phi distributions weighted by Energy for Photons in KORALB(Red) and kk2f(Blue) . . . . .	108
8.4	Comparison of Mass Plots for kk2f and KORALB using the default kk2f TAUOLA and kk2f using the CLEO TAUOLA . . . . .	108
9.1	Event Hemispheres . . . . .	115
9.2	Neutral Energy with all other cuts applied. . . . .	117
9.3	$\cos \theta_{Miss}$ . . . . .	118
9.4	One Prong Momentum Spectrum . . . . .	119
9.5	Cross-sections for Pion-Proton Interactions [1] . . . . .	121
9.6	Distance from Positive $K_S^0$ Daughter to Nearest Neutral . . . . .	121
9.7	Distance from Negative $K_S^0$ Daughter to Nearest Neutral . . . . .	122
9.8	Distance from Bachelor Track to Nearest Neutral . . . . .	122
9.9	Neutral Asymmetry for Bachelor Track in Data . . . . .	123
9.10	Neutral-Track Distance (cm) for Bachelor Track in Data . . . . .	123

9.11	Neutral Asymmetry for $K_S^0$ Daughter Tracks in Data . . . . .	124
9.12	Neutral-Track Distance (cm) for $K_S^0$ Daughter Tracks in Data . . . . .	124
9.13	Tracking Asymmetry for Fitted $K_S^0$ Daughter Tracks in Data . . . . .	125
9.14	Momentum (GeV) for Fitted $K_S^0$ Daughter Tracks in Data . . . . .	125
9.15	Tracking Asymmetry for Bachelor Track in Data . . . . .	126
9.16	Momentum (GeV) for Bachelor Track in Data . . . . .	126
9.17	Fit of difference between the Reconstructed Momentum and the True Momentum for KsDefault (Red) and KsTight (Black) Candidates . . . . .	128
9.18	$K_S^0$ Mass and Lifetime Significance for Vertex Fitted Ks0 Candidates . . . . .	129
9.19	The $K_S^0$ mass spectrum and lifetime significance with all cuts applied except the quantity plotted . . . . .	130
10.1	The $K_S^0\pi$ mass spectrum with all cuts applied. . . . .	138
10.2	The $K_S^0\pi$ mass spectrum with all cuts applied. . . . .	139
11.1	$\langle \epsilon \rangle$ Vs $K_S^0\pi$ Mass for $\mathfrak{S}\Lambda = 1$ (Red represents $\tau^-$ decays and black $\tau^+$ decays) . . . . .	142
11.2	$\langle \epsilon \rangle$ Vs $\mathfrak{S}\Lambda$ . . . . .	142
12.1	Effect of varying $K^*(1430)$ parameters . . . . .	149

14.1 Summary of current measurements of  $\mathfrak{S}\Lambda$  . . . . . 154

# List of Tables

5.1	Measured CP Asymmetries in Signal and Sideband [2,3]	53
6.1	Cross-sections of Different Processes [4]	59
8.1	Comparison of KORALB and KK 4.13	106
8.2	Branching Fractions used in kk2f in SP5 [1]	110
9.1	Parameters of Fit to Momenta Spectra of Pions	128
9.2	Efficiencies (%), Purities (%) and Significance of Selection Criteria	133
9.3	Efficiencies of Selection Criteria	134
12.1	Summary of Systematic Errors on MC corrections	150
12.2	Summary of Systematic Errors on $\Im(\Lambda)$	150

## Abstract

A sample of  $\tau^\pm \rightarrow K^{*\pm}$  decays with  $K^{*\pm} \rightarrow K_S^0 \pi^\pm$  and  $K_S^0 \rightarrow \pi^+ \pi^-$ , using  $123.4 \text{ fb}^{-1}$  of data collected by the BaBar detector at the Stanford Linear Accelerator Center, is used to search for a direct CP violation effect in the charged Higgs sector. No evidence of CP violation is found and the imaginary part of the charged Higgs coupling,  $\Im(\Lambda)$ , in the Multi-Higgs-Doublet-Model is found to be at  $-0.284 < \Im(\Lambda) < 0.200$  at 90 % Confidence Level. In addition the installation of the kk2f Monte Carlo generator into the BaBar software framework is described.

# Declaration

No portion of the work referred to in this thesis has been submitted in support of an application for another degree or qualification of this or any other university or other institute of learning.

Copyright in text of this thesis rests with the Author. Copies (by any process) either in full, or of extracts, may be made only in accordance with instructions given by the Author and lodged in the John Rylands University Library of Manchester. Details may be obtained from the Librarian. This page must form part of any such copies made. Further copies (by any process) of copies made in accordance with such instructions may not be made without the permission (in writing) of the Author.

The ownership of any intellectual property rights which may be described in this thesis is vested in the University of Manchester, subject to any prior agreement to the contrary, and may not be made available for use by third parties without the written permission of the University, which will prescribe the terms and conditions of any such agreement.

Further information on the conditions under which disclosures and exploitation may take place is available from the Head of the Department of Physics and Astronomy.

## The Author

Mark Hodgkinson was educated at Reigate Grammar School, Surrey and went on to obtain a MPhys in Physics with Theoretical Physics at the University of Manchester. The research in this thesis was undertaken jointly at the University of Manchester and the Stanford Linear Accelerator Centre.

## BaBar Disclaimer

BaBar theses are not reviewed by the BaBar collaboration and are therefore not official BaBar publications.

# Acknowledgements

There are a large number of people who I would like to thank. In particular I owe a lot to my parents who financed my first degree without which I would not be here. My supervisor, Dr John Allison, has been a great help over the years providing constant encouragement and advice - I wish him a long and happy retirement.

Whilst at SLAC I came into contact with many physicists. I wish to single out both Dr Swagato Bannerjee whose encyclopedic knowledge of everything BaBar and analysis was invaluable to me, and Dr Abi Soffer who taught me a lot about the BaBar software framework necessary to complete my work on the tau MC studies. In addition I would like to thank (in no particular order) Dr Olga Igonkina, Professor Mike Roney, Dr Helmut Marsiske, Dr Fred Loebinger, Professor George Lafferty and Professor Roger Barlow who have all provided guidance over the years.

I made many friends during my PhD so I'll thank you all now (again in no special order): Jamie Boyd (thanks for pushing me down the blue ski slope..), Sophie Mallows (thanks for organising the trip to S.America), Andy Lyon, Jamie Gaillard, Jenny Williams, Tom Latham, Kelly Ford, Paul Jackson, Sian Morgan, Henning Flaecher, Wahid Bhimji, Eric Charles, Nick Barlow, Mitchell Naisbit, Phil Clarke, Alessandra

Forti, Steve Dallison, Sabah Salih, Gary Taylor, Emannuele Olaiya, Steve Malloy, Girish Hullati (thanks for Mt Dana), Debbie Bard, Jim Weatherall, Rob Flack, Ed Hill, Marc Kelly, Sylvie Brunet, David Cote-Ahern and Frank Jackson. I would also like to thank my sister Eleanor.

Finally I would like to thank all my uni friends for putting up with the physics over the years: Tom Robson, Mike Hodgson, Pete Tubby, Chris Waugh, Dan Hartley, Amy Turner, David Pape and Neil Milbourne.

# Chapter 1

## Introduction

One of the long standing puzzles in experimental particle physics and cosmology is the absence of anti-matter in the Universe. Everything we see is made of matter. The Big Bang theory requires there were equal amounts of matter and anti-matter at the start of the universe. Given anti-matter and matter annihilate (into a pure energy state) when they come into contact it would be expected that the Universe should not currently contain any stable matter or anti-matter. At some point a mechanism led to an excess of matter over anti-matter. The only explanation to date is the phenomenon of CP violation.

CP violation has been observed in the kaon and B meson particle systems. However calculations indicate that the CKM triangle, which describes CP violation in these particle systems, does not contain enough CP violation to account for the observed asymmetry in matter and anti-matter [5]. Thus there must either be more sources of CP violation in nature or a further mechanism to produce the asymmetry.

The main three candidate areas for further possible CP violation are the neutrino sector, the charged Higgs sector and the neutral Higgs sector. All measurements in the Higgs sectors are consistent with no CP violation being present [6], but all the measurements are very difficult, and are statistically limited because they usually involve rare processes. This thesis contains details of a search in the charged Higgs sector using a high statistics sample of semileptonic tau decays.

The tau is the heaviest of the three charged leptons (electron, muon and tau) and was discovered in 1975 [7]. The Standard Model also contains three generations of quarks, and currently there is no evidence for the existence of further generations of quarks and leptons. In addition to the quarks and leptons there exist the gauge bosons which mediate the electromagnetic, strong and weak forces. Amongst all the particles in the Standard Model there is only one that has yet to be discovered, namely the (neutral) Higgs boson [8]. This was sought after at the four experiments of the Large Electron Positron collider at CERN, is being actively sought at the Tevatron at Fermilab, and will be the subject of extensive searches (assuming the Tevatron does not find it first) at the three experiments located on the Large Hadron Collider (LHC) which is scheduled to start running in 2007.

In this thesis the Standard Model of particle interactions is first introduced, followed by descriptions of CP violation in the Standard Model, CP violation in the Higgs sector and a chapter on the experimental situation with regard to CP violation in tau physics. The thesis then proceeds to describe the BaBar detector, the BaBar software (including the authors contributions to the tau Monte Carlo software), and finally the search for CP violation in tau decays with the BaBar detector is described.

# Chapter 2

## The Standard Model

The model used to describe interactions between particles is known as the Standard Model of Particle Physics which is more often referred to simply as the Standard Model. The model will be shown starting with an overview of Quantum Electrodynamics followed by Quantum Chromodynamics, weak dynamics and finally the Weinberg-Salam model of electroweak interactions will be introduced. [8]

### 2.1 Quantum Electrodynamics

A Lagrangian that produces the Dirac equations of motion of the electron is

$$\mathcal{L} = \bar{\psi}(i\gamma^\mu\partial_\mu - m)\psi \tag{2.1}$$

where  $\psi$  is a Dirac spinor,  $\bar{\psi}$  is the adjoint spinor and is defined as  $\psi^\dagger\gamma^0$ ,  $\gamma^\mu$  are the Dirac gamma matrices and  $m$  is a mass. In order to conserve charge the Lagrangian

is required to be invariant under an  $U(1)$  transformation. The  $U(1)$  group is a group of phase transformations,

$$U(\alpha) \equiv e^{i\alpha}, \quad (2.2)$$

where  $\alpha$  is a real number. The group is known as an Abelian group because the multiplicative algebra is commutative. The physical implication of an Abelian group is that the gauge bosons in the theory do not interact with other gauge bosons of the same type.

The Lagrangian in (2.1) is not invariant under local  $U(1)$  transformations, and so requires modification. When we perform the transformation

$$\psi(x) \rightarrow e^{i\alpha(x)}\psi(x) \quad (2.3)$$

the form of (2.1) is changed. Hence the ordinary derivative,  $\partial_\mu$ , is replaced with a covariant derivative

$$D_\mu \equiv \partial_\mu - ieA_\mu \quad (2.4)$$

where  $A_\mu$  transforms under a  $U(1)$  transformation as:

$$A_\mu \rightarrow A_\mu + \frac{1}{e}\partial_\mu\alpha. \quad (2.5)$$

The  $A_\mu$  field is the photon field and so one more term needs to be added to the Lagrangian to describe the kinetic energy of the photon. The kinetic term must be invariant under (2.5) and so it is constructed from the gauge invariant field strength tensor

$$F_{\mu\nu} = \partial_\mu A_\nu - \partial_\nu A_\mu. \quad (2.6)$$

The Lagrangian describing QED is therefore

$$\mathcal{L}_{QED} = \bar{\psi}(i\gamma^\mu\partial_\mu - m)\psi + e\bar{\psi}\gamma^\mu A_\mu\psi - \frac{1}{4}F_{\mu\nu}F^{\mu\nu}. \quad (2.7)$$

This Lagrangian is the same as (2.1) with the addition of the second term, resulting from the use of the covariant derivative, and the third term which represents the kinetic energy of the new field introduced by the covariant derivative. This Lagrangian has no mass term for the gauge boson, and it cannot, for if one were added the gauge invariance would be broken.

## 2.2 Quantum Chromodynamics

Once again we can start with a Lagrangian for Quantum Chromodynamics (QCD) in the same way as we did for QED so that

$$\mathcal{L} = \bar{q}_i(i\gamma^\mu\partial_\mu - m)q_i \quad (2.8)$$

where  $q_i$  are the three colour fields for a given quark flavour, only one of which need be considered in this description because there are no flavour changing transitions, and the  $\bar{q}_i$  are the adjoint fields. This Lagrangian must be locally invariant under SU(3) transformations of the colour fields. The form of these transformations is

$$q(x) \rightarrow Uq(x) \equiv e^{i\alpha_j(x)T_j}q(x). \quad (2.9)$$

$U$  is an arbitrary 3 x 3 unitary matrix,  $T_j$  are linearly independent traceless 3 x 3 matrices which are the generators of the group, and  $\alpha_j$  are the group parameters.

Due to the fact that not all the  $T_j$ , known as the Gell-Mann matrices, commute with each other,  $SU(3)$  is a non-Abelian group.

The next step is to introduce a covariant derivative in order to make the Lagrangian locally gauge invariant under  $SU(3)$ . This is

$$D_\mu = \partial_\mu + igT_j G_\mu^j \quad (2.10)$$

where  $g$  is a coupling constant. The gauge fields transform as

$$G_\mu^j \rightarrow G_\mu^j - \frac{1}{g} \partial_\mu \alpha_j(x). \quad (2.11)$$

Thus the Lagrangian becomes

$$\mathcal{L} = \bar{q}(i\gamma^\mu \partial_\mu - m)q - g(\bar{q}\gamma^\mu T_j q)G_\mu^j. \quad (2.12)$$

The above Lagrangian is not gauge invariant using the form of  $G_\mu^j$  in (2.11). This problem arises because the generators  $T_j$  do not all commute with each other and so the gauge transformation of  $q(x)$  introduces an extra term into the Lagrangian. To maintain gauge invariance the transformation of the gauge fields must be modified to enforce the removal of the extra term, and so

$$G_\mu^j \rightarrow G_\mu^j - \frac{1}{g} \partial_\mu \alpha_j(x) - f_{jkl} \alpha_k(x) G_\mu^l. \quad (2.13)$$

where  $f_{jkl}$  are real constants known as the structure constants of the group. Finally adding a kinetic term for the gauge fields the QCD Lagrangian is given by

$$\mathcal{L}_{QCD} = \bar{q}(i\gamma^\mu \partial_\mu - m)q - g(\bar{q}\gamma^\mu T_j q)G_\mu^j - \frac{1}{4} G_{\mu\nu}^j G_j^{\mu\nu}, \quad (2.14)$$

where

$$G_{\mu\nu}^j = \partial_\mu G_\nu^j - \partial_\nu G_\mu^j - gf_{jkl}G_\mu^k G_\nu^l. \quad (2.15)$$

The third term (2.15) leads to a self interaction of the gauge fields, known as gluons, which carry the colour charge. This situation has occurred because the SU(3) group is non-Abelian in nature. Conversely the photons of QED have no electric charge and no self interactions due to the Abelian nature of the U(1) group.

## 2.3 Weak Dynamics

The third interaction described in the Standard Model is the weak one. Thus the Standard Model encompasses the electromagnetic, weak and strong interactions, but not the gravitational interaction (Einstein's classical General Theory of Relativity is the current theory used to describe gravity, and it has yet to be satisfactorily quantised let alone included in the Standard Model).

To conserve weak charge the SU(2) symmetry must be conserved. A field undergoing a SU(2) transformation does so as follows:

$$\psi(x) \rightarrow \psi'(x) = e^{i\tau_j \omega_j(x)} \psi(x) \quad (2.16)$$

where  $\tau_j$  are the Pauli matrices, which are the generators of the SU(2) group, and  $w_j$  are the group parameters. The Pauli matrices are identical to three of the Gell-Mann matrices, and so SU(2) is a sub-group of SU(3). Again the covariant derivative must be formed and used:

$$D_\mu = \partial_\mu + ig\tau_j W_\mu^j. \quad (2.17)$$

Therefore the gauge field must transform as

$$W_\mu^j \rightarrow W_\mu^j - \partial_\mu \omega_j(x) - g \epsilon_{jkl} \omega_l(x) W_\mu^k. \quad (2.18)$$

The weak interaction Lagrangian is given by

$$\mathcal{L}_{weak} = \bar{\psi}(i\gamma^\mu \partial_\mu - m)\psi - g(\bar{\psi}\gamma^\mu \tau_j \psi)W_\mu^j - \frac{1}{4}W_{\mu\nu}^j W_j^{\mu\nu} \quad (2.19)$$

where

$$W_{\mu\nu}^j = \partial_\mu G_\nu^j - \partial_\nu G_\mu^j - g \epsilon_{jkl} W_\mu^k W_\nu^l. \quad (2.20)$$

## 2.4 The Weinberg-Salam Electroweak Model

This model unifies the weak and electromagnetic forces into one electroweak force. It does not unify this with the strong or gravitational force. This is illustrated in Figure 2.1 where the coupling constants of the U(1), SU(2) and SU(3) groups are plotted as functions of energy. At very high energies, at the GUT mass  $M_X$ , it is expected that  $SU(2) \otimes U(1)$  will unify with SU(3).

The Lagrangian for this model will now be explained in four steps due to the large number of components.

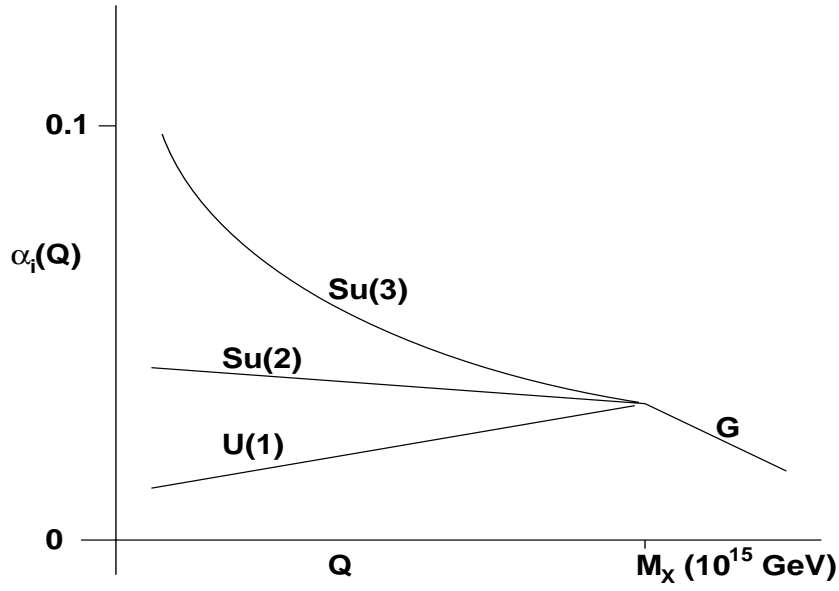


Figure 2.1: Scaling of Coupling Constants with Energy

## 2.5 The Gauge Boson Kinetic Energies and Self-Interactions

The term describing the gauge boson kinetic energies and self-interactions is given by

$$-\frac{1}{4}W_{\nu\mu}\cdot W^{\nu\mu} - \frac{1}{4}B_{\nu\mu}\cdot B^{\nu\mu} \quad (2.21)$$

where

$$W_{\nu\mu} = \partial_\mu W_\nu - \partial_\nu W_\mu - gW_\mu \times W_\nu. \quad (2.22)$$

and

$$B_{\nu\mu} = \partial_\mu B_\nu - \partial_\nu B_\mu. \quad (2.23)$$

The physical  $W$ , photon and  $Z$  fields are built from  $B_\mu$  and  $W_\mu$  as follows:

$$W_\mu^\pm = \sqrt{\frac{1}{2}}(W_\mu^1 \mp iW_\mu^2); \quad (2.24)$$

$$A_\mu = B_\mu \cos \theta_W + W_\mu^3 \sin \theta_W; \quad (2.25)$$

$$Z_\mu = -B_\mu \sin \theta_W + W_\mu^3 \cos \theta_W. \quad (2.26)$$

The angle  $\theta_W$  is known as the weak mixing angle. Equation (2.21) represents the kinetic energy of the  $W^\pm$ ,  $Z$  and photon kinetic energies and self-interactions of the  $W$ -Bosons.

## 2.6 The Lepton and Quark Kinetic Energies and their Couplings to the Gauge Bosons

This part of the Lagrangian is given by

$$\bar{L}\gamma^\mu \left( i\partial_\mu - g\frac{1}{2}\tau \cdot W_\mu - g'\frac{Y}{2}B_\mu \right) L + \bar{R}\gamma^\mu \left( i\partial_\mu - g'\frac{Y}{2}B_\mu \right) R \quad (2.27)$$

where  $\gamma^\mu$  are the Dirac  $\gamma$ -matrices,  $\tau$  are the Pauli spin matrices,  $Y$  is the weak hypercharge,  $g$  and  $g'$  are couplings dependent on the electric charge,  $e$ , as follows:

$$e = g \sin \theta_W = g' \cos \theta_W. \quad (2.28)$$

Equation (2.29) represents the fermion kinetic energies ( $L$  is a left-handed fermion doublet and  $R$  is a right-handed fermion singlet) and fermion interactions with  $W$  bosons,  $Z$  bosons or photons. It has been experimentally observed that the

weak interaction couples to left-handed particles and right-handed anti-particles only, which is why there is no term of the form  $\bar{R}W_\mu R$ .

## 2.7 Gauge Boson Masses and Higgs Mass and Couplings

This term is given by

$$\left| \left( i\partial_\mu - g\frac{1}{2}\tau \cdot W_\mu - g' \frac{Y}{2} B_\mu \right) \phi \right|^2 - V(\phi). \quad (2.29)$$

The four  $\phi$  fields are contained in an isospin doublet

$$\phi = \begin{pmatrix} \phi^+ \\ \phi^0 \end{pmatrix} \quad (2.30)$$

where

$$\phi^+ = \frac{\phi_1 + i\phi_2}{\sqrt{2}} \quad (2.31)$$

and

$$\phi^0 = \frac{\phi_3 + i\phi_4}{\sqrt{2}}. \quad (2.32)$$

The Higgs potential is given by

$$V(\phi) = \mu^2 \phi^\dagger \phi + \lambda (\phi^\dagger \phi)^2. \quad (2.33)$$

The interesting case is one in which  $\mu^2 < 0$  and  $\lambda > 0$ . Then the value of  $|\phi|$  that minimises  $V(\phi)$  is given by

$$\phi^\dagger \phi = -\frac{\mu^2}{2\lambda} = \frac{v^2}{2}. \quad (2.34)$$

The  $SU(2)_L \otimes U(1)_Y$  symmetry is spontaneously broken when  $|\phi|$  acquires a non-zero value. The values of the complex scalar fields,  $\phi$ , that break the symmetry are infinite in number. The choices are reduced when one demands that the photon remains massless as observed experimentally. The choice turns out to be

$$\phi^0 = \frac{v}{\sqrt{2}}. \quad (2.35)$$

and

$$\phi^\pm = 0. \quad (2.36)$$

All the fields, except  $\phi_4$ , are set to zero with this choice. If we operate on  $\phi_0$  with all combinations of the four  $SU(2)_L \otimes U(1)_Y$  generators, only the combination  $Q$ ,

$$Q = T^3 + \frac{Y}{2}, \quad (2.37)$$

preserves the  $U(1)$  symmetry:

$$Q\phi_0 = 0. \quad (2.38)$$

Thus the photon remains massless and the other gauge bosons acquire masses because the other three combinations of generators do not give a value of zero when operating on  $\phi_0$ . It can be shown that, by substituting the value of  $\phi$

$$\phi(x) = \sqrt{\frac{1}{2}} \begin{pmatrix} 0 \\ v + h(x) \end{pmatrix} \quad (2.39)$$

into this part of the Lagrangian, the other gauge boson masses are given by

$$M_W = \frac{37.3}{\sin\theta_W} GeV. \quad (2.40)$$

and

$$M_Z = \frac{74.6}{\sin 2\theta_W} GeV. \quad (2.41)$$

These predictions were confirmed at CERN in 1983 when the  $W$  [9] and  $Z$  [10] bosons were discovered.

## 2.8 Fermion Masses and Couplings to Higgs Boson

The final part of the Electroweak Lagrangian is given by

$$-(G_1 \bar{L}\phi R + G_2 \bar{L}\phi_c R + h.c.) \quad (2.42)$$

where the  $G$ 's are coupling constants,  $L$  are again the left-handed fermion doublets,  $R$  are right-handed fermion singlets,  $\phi$  is as defined in 2.1.3,  $h.c$  refers to the hermitian conjugate term and  $\phi_c$  is given by:

$$\phi_c = \begin{pmatrix} -\phi^0 \\ \phi^- \end{pmatrix}. \quad (2.43)$$

Again the masses of the fermions are obtained by substituting equation 2.39 into the Lagrangian. Unfortunately the values of  $G_1$  and  $G_2$  are arbitrary, and so the masses of the fermions and the Higgs are not predicted by the Standard Model.

## 2.9 Summary

The Standard Model of particle physics includes quantum theories of the electromagnetic, strong and weak forces. It includes a unified theory of two of the forces, the weak and electromagnetic, in the Weinberg-Salam Electroweak model. The masses of the gauge bosons are acquired by electroweak symmetry breaking instead of inserting mass terms into the Lagrangian by hand which would break the gauge invariance of the Standard Model.

The next chapter describes why CP violation had to be inserted by hand in the 1960's, leading up to the cosmological need for further sources, the effects of which may be observable in semileptonic  $\tau$  particle decays.

# Chapter 3

## C, P and CP Violation

The parity operator reverses the sign of any spatial coordinates of a wavefunction:

$$P\psi(\vec{r}, t) \equiv \psi(-\vec{r}, t). \quad (3.1)$$

Parity is conserved by the strong and electromagnetic interactions, but not the weak interaction. One of the first experiments to observe this effect looked at  $\beta$ -transitions of polarised Cobalt nuclei. These undergo



The experimental data showed that the electron was preferentially emitted in a direction opposite to the nuclear spin axis. The explanation for this is that the electron is left-handed and the anti-neutrino right-handed. This led to the Weinberg-Salam model which only includes a weak coupling to left-handed particles and right-handed anti-particles (described in section 1.0.6).

Charge-conjugation changes a particle into its anti-particle. C operating on a left-handed neutrino gives

$$C|\nu_L \rangle = |\bar{\nu}_L \rangle . \quad (3.3)$$

Charge conjugation is violated when parity is violated because parity violation suppresses left-handed anti-neutrinos. For a short time it was thought C and P violation canceled each other out such that under the CP operation processes are invariant, but it was soon found that this was not always the case.

### 3.1 CP Violation in $K^0$ Mixing

Neutral kaons exist in definite quark states consisting of a down and strange quark. In weak interactions strangeness is not conserved allowing the  $K^0$  state to transform into the  $\bar{K}^0$  state. The result of this mixing is two mass eigenstates  $K_S^0$  and  $K_L^0$  which have different CP quantum numbers and lifetimes

$$\tau_{K_S^0} = (0.8935 \pm 0.0008) \times 10^{-10} \text{ s}$$

and

$$\tau_{K_L^0} = (5.17 \pm 0.04) \times 10^{-8} \text{ s}.$$

It was originally thought that the  $K_1^0$  and  $K_2^0$  states,

$$|K_1^0 \rangle = \sqrt{\frac{1}{2}}(|K^0 \rangle + |\bar{K}^0 \rangle) \quad (3.4)$$

and

$$|K_2^0 \rangle = \sqrt{\frac{1}{2}}(|K^0 \rangle - |\bar{K}^0 \rangle), \quad (3.5)$$

were the two mass eigenstates. In 1964 Christenson and Cronin et al published a paper demonstrating that the  $K_2^0$  decayed to a 2 charged pion final state sometimes. [11] The  $K_1^0$  state has a CP eigenvalue of +1 (CP even) and the  $K_2^0$  state has a CP eigenvalue of -1 (CP odd). The 2 pion final state is CP even, and the presence of a decay from a CP even state to a CP odd state means CP violation is occurring. Hence the  $K_S^0$  and  $K_L^0$  states must both be a mixture of CP even and CP odd states, and therefore they do not correspond to the  $K_1^0$  and  $K_2^0$  states. Instead they are

$$|K_S^0 \rangle = \sqrt{\frac{1}{1 + |\tilde{\epsilon}|^2}}(|K_1^0 \rangle + \tilde{\epsilon}|K_2^0 \rangle) \quad (3.6)$$

and

$$|K_L^0 \rangle = \sqrt{\frac{1}{1 + |\tilde{\epsilon}|^2}}(\tilde{\epsilon}|K_1^0 \rangle + |K_2^0 \rangle). \quad (3.7)$$

This effect is known as mixing and  $\tilde{\epsilon}$  is the mixing parameter. CP violation is occurring because the mass eigenstates are mixtures of different CP eigenstates. This type of CP violation is known as indirect CP violation. If (3.6) and (3.7) are rewritten as

$$|K_S^0 \rangle = p|K^0 \rangle + q|\bar{K}^0 \rangle \quad (3.8)$$

and

$$|K_L^0 \rangle = p|K^0 \rangle - q|\bar{K}^0 \rangle, \quad (3.9)$$

$\tilde{\epsilon}$  is given by

$$\tilde{\epsilon} = \frac{q - p}{q + p}. \quad (3.10)$$

The mixing parameter represents the CP asymmetry between  $K^0$  and  $\bar{K}^0$  states and is approximated by the ratio of amplitudes

$$\epsilon = \frac{\langle (\pi\pi)_{I=0} | H | K_L^0 \rangle}{\langle (\pi\pi)_{I=0} | H | K_S^0 \rangle} \quad (3.11)$$

via

$$\epsilon = \tilde{\epsilon} + i \left( \frac{\Im A_0}{\Re A_0} \right) \quad (3.12)$$

where

$$A_I = \langle (\pi\pi)_I | H | K^0 \rangle \quad (3.13)$$

and  $\pi\pi$  denotes the 2 pion state with charges (00) or (+-). The values of the isospin (I) are governed by the empirical  $\Delta I = \frac{1}{2}$  rule which states that the isospin may change by a value of one half in the decay. The kaon has isospin one half and so by the  $\Delta I = \frac{1}{2}$  rule the final state may be in a I=1 or I=0 state. The  $\Delta I = \frac{1}{2}$  rule is not exact and it is possible that  $\Delta I = \frac{3}{2}$  transitions can occur leading to  $I = 2$  final states.

The isospin of  $\pi\pi$  systems may only take the values 0 and 2, however. This is because pions are bosons, and Bose-Einstein statistics requires that the two pion state wavefunction must be symmetric. The overall wavefunction is a product of an isospin and spatial wavefunction. The two pions have zero total orbital angular momentum (because they are spin zero with total angular momentum zero), and therefore the spatial wavefunction is spherically symmetric forcing the isospin wavefunction to be symmetric. The  $I = 1$  wavefunction is antisymmetric and so is forbidden to exist for these types of decays.

A theoretical paper [12] was published in 1964 in response to the discovery of CP

violation in the kaon system. Wu and Yang showed that the phase of the  $K^0$  can be chosen such that  $\Im A_0$  is zero. The phase of the  $K^0$  can be changed because when the phase of the strange quark is changed,

$$|s\rangle \rightarrow |s\rangle e^{i\theta}, \quad (3.14)$$

all observable quantities are unchanged. The implication of this Wu-Yang phase convention is that  $\epsilon$  is the same as the mixing parameter of CP violation in the kaon system. The Particle Data Group (PDG) in their 2002 review [1] give the mixing parameter as

$$|\epsilon| = (2.282 \pm 0.017) \times 10^{-3}.$$

## 3.2 CP Violation in Kaon Decay

As described above CP violation in the  $K^0$  system due to mixing is parameterised by  $\epsilon$ . A further parameter  $\epsilon'$  is introduced to describe CP violation in kaon decays, and this is known as direct CP violation. This occurs if the amplitude for a decay is not the same as the amplitude for the CP conjugate decay. The ratio of the  $K_S^0$  and  $K_L^0$  amplitudes depends on both  $\epsilon$  and  $\epsilon'$ .

$$\eta_{+-} = \frac{A(K_L \rightarrow \pi^+ \pi^-)}{A(K_S \rightarrow \pi^+ \pi^-)} \simeq \epsilon + \epsilon' \quad (3.15)$$

The decay amplitudes of the kaons are parameterised by

$$\langle (\pi\pi)_I | H | K^0 \rangle = a_I e^{i\delta_I} \quad (3.16)$$

and

$$\langle (\pi\pi)_I | H | \bar{K}^0 \rangle = a_I^* e^{i\delta_I} \quad (3.17)$$

where the  $\delta$ 's are the strong phase shifts due to interactions between the two pions.

If CP is conserved in kaon decays then the following relations hold [13]

$$a_0 = a_0^* \quad (3.18)$$

and

$$a_2 = a_2^*. \quad (3.19)$$

Parameterising the  $a_I$  in terms of a weak phase,

$$a_I = |a_I| e^{i\theta_I}, \quad (3.20)$$

CP is conserved when the  $\theta_I$  are 0 or  $\pi$ . The  $\theta_I$  may be redefined in an arbitrary way and in the Wu-Yang convention

$$\theta_0 = 0. \quad (3.21)$$

Due to the possibility of arbitrary phase redefinitions the relation

$$\theta_2 - \theta_0 = n\pi \quad (3.22)$$

needs to be tested to confirm CP violation, where  $n$  is an integer.

Using this formalism 3.15 can be rewritten as

$$\eta_{+-} = \frac{(1 - \eta)[1 + w \cos(\theta_2 - \theta_0)] + i(1 + \eta)w \sin(\theta_2 - \theta_0)}{(1 + \eta)[1 + w \cos(\theta_2 - \theta_0)] + i(1 - \eta)w \sin(\theta_2 - \theta_0)}, \quad (3.23)$$

where

$$\eta \equiv \frac{q}{p} e^{-2i\theta_0} \quad (3.24)$$

and

$$w \equiv \frac{1}{\sqrt{2}} \left| \frac{a_2}{a_0} \right| e^{i(\delta_2 - \delta_0)}. \quad (3.25)$$

The suppression inherent in the  $\Delta I = \frac{1}{2}$  rule allows the use of the approximation

$$\frac{a_2}{a_0} \ll 1. \quad (3.26)$$

Therefore [13] the amplitude ratio reduces to

$$\eta_{+-} = \epsilon + \epsilon', \quad (3.27)$$

where

$$\epsilon' = \frac{i}{\sqrt{2}} e^{i(\delta_2 - \delta_0)} \left| \frac{a_2}{a_0} \right| \sin(\theta_2 - \theta_0). \quad (3.28)$$

Similarly a second ratio of amplitudes,

$$\eta_{00} = \frac{A(K_L \rightarrow \pi^0 \pi^0)}{A(K_S \rightarrow \pi^0 \pi^0)}, \quad (3.29)$$

can be reduced to

$$\eta_{00} = \epsilon - 2\epsilon'. \quad (3.30)$$

These are the standard definitions used by practicing particle physicists [1]. Clearly

if  $\epsilon'$  is zero, equation 3.22 is valid and there is no direct CP violation in kaon decays. In this case the ratios  $\eta_{+-}$  and  $\eta_{00}$  will take the same value. Thus the ratio of the two amplitude ratios is a measure of whether direct CP violation occurs or not. The PDG 2002 gives

$$\Re\left(\frac{\epsilon'}{\epsilon}\right) = (1.8 \pm 0.4) \times 10^{-3} \quad (3.31)$$

where

$$\left|\frac{\eta_{00}}{\eta_{+-}}\right|^2 \approx 1 - 6\Re\left(\frac{\epsilon'}{\epsilon}\right). \quad (3.32)$$

Thus, there appears to be a small amount of direct CP violation in the  $K^0$  system which is accommodated in the Standard Model, and is expressed in the Cabbibo-Kobayashi-Maskawa (CKM) matrix. The origins of this matrix are still not known, leaving the CP violation allowed in the Standard Model, but not arising from any known fundamental principle.

### 3.3 The CKM Matrix

The V-A theory of weak interactions forbids weak currents coupling quarks from different generations. For example the vertex where a W interacts with an up-strange quark pair is forbidden, but it has been observed in nature. The V-A theory was set up to couple quarks to the W bosons in analogy with the way leptons were known to couple to the W bosons, meaning vertices involving quarks from different generations were possible.<sup>1</sup> The solution to this problem is to introduce the rotated

---

<sup>1</sup>The implications of the discovery of neutrino mass is that vertices involving leptons from different generations occur

quark states  $d'$  and  $s'$

$$\begin{pmatrix} d' \\ s' \end{pmatrix} = V_C \begin{pmatrix} d \\ s \end{pmatrix} \quad (3.33)$$

where

$$V_{KM} = \begin{pmatrix} \cos \theta_c & \sin \theta_c \\ -\sin \theta_c & \cos \theta_c \end{pmatrix} \quad (3.34)$$

and  $\theta_c$  is known as the Cabbibo angle. The primed quarks represent the weak eigenstates that interact with the W bosons, and the unprimed quarks represent the physical mass eigenstates. The KM matrix is real because any complex parameters can be removed by redefinition of the quark phases.

The addition of the third doublet leads to a 3 x 3 matrix known as the Cabbibo-Kobayashi-Maskawa mixing matrix. In an  $n \times n$  matrix there must be  $n^2$  complex parameters [8]. The  $2n$  quark states can have their phases redefined. Performing these transformations for all but one of the quark states, so as to not leave the matrix invariant,  $n^2 - (2n - 1)$  parameters are left over. In an  $n \times n$  orthogonal matrix there are only  $\frac{1}{2}n(n - 1)$  real parameters. So there will always be

$$n^2 - (2n - 1) - \frac{1}{2}n(n - 1) \quad (3.35)$$

complex phases left over. For  $n = 3$  this gives one left-over phase. Therefore one complex phase factor cannot be removed in the unitary and orthogonal CKM matrix meaning 3 generations of quarks provides CP violation in the quark sector.

The CKM matrix can be parameterised by

$$V_{CKM} = \begin{pmatrix} c_{12}c_{13} & s_{12}c_{13} & s_{13}e^{-i\delta_{13}} \\ -s_{12}c_{23} - c_{12}s_{23}s_{13}e^{i\delta_{13}} & c_{12}c_{23} - s_{12}s_{23}s_{13}e^{i\delta_{13}} & s_{23}c_{13} \\ s_{12}s_{23} - c_{12}c_{23}s_{13}e^{i\delta_{13}} & -c_{12}s_{23} - s_{12}c_{23}s_{13}e^{i\delta_{13}} & c_{23}c_{13} \end{pmatrix}, \quad (3.36)$$

where  $s_{ij} = \sin\theta_{ij}$ ,  $c_{ij} = \cos\theta_{ij}$ , and  $\delta_{ij}$  is a phase. The index  $i(j)$  runs from 1 to 3 corresponding to the three generations of quarks. The other commonly used parameterisation is the Wolfenstein approximation, valid for small  $\theta_{ij}$ :

$$V_{CKM} = \begin{pmatrix} 1 - \frac{\lambda^2}{2} & \lambda & A\lambda^3(\rho - i\eta) \\ -\lambda & 1 - \frac{\lambda^2}{2} & A\lambda^2 \\ A\lambda^3(1 - \rho - i\eta) & -A\lambda^2 & 1 \end{pmatrix}. \quad (3.37)$$

The parameters  $\lambda$ ,  $A$ ,  $\rho$  and  $\eta$  parameterise the mixing in this scheme. This parameterisation is good for  $\lambda \ll 1$  ( $\lambda$  is 0.2). The naming convention of the elements is given by

$$V_{CKM} = \begin{pmatrix} V_{ud} & V_{us} & V_{ub} \\ V_{cd} & V_{cs} & V_{cb} \\ V_{td} & V_{ts} & V_{tb} \end{pmatrix} \quad (3.38)$$

At 90% Confidence Level (CL) these are measured to be [1]

$$V_{CKM} = \begin{pmatrix} 0.9739 \text{ to } 0.9751 & 0.221 \text{ to } 0.227 & 0.0029 \text{ to } 0.0045 \\ 0.221 \text{ to } 0.227 & 0.9730 \text{ to } 0.9744 & 0.039 \text{ to } 0.044 \\ 0.0048 \text{ to } 0.014 & 0.037 \text{ to } 0.043 & 0.9990 \text{ to } 0.9992 \end{pmatrix}. \quad (3.39)$$

The unitary nature of this matrix leads to some interesting relations. The most interesting one is

$$V_{ud}V_{ub}^* + V_{cd}V_{cb}^* + V_{td}V_{tb}^* = 0 \quad (3.40)$$

due to the fact it is one of only two relations that are not dominated by one large term. It can be represented in the complex plane geometrically as a triangle, known as the Unitarity Triangle, shown in Figure 3.1.

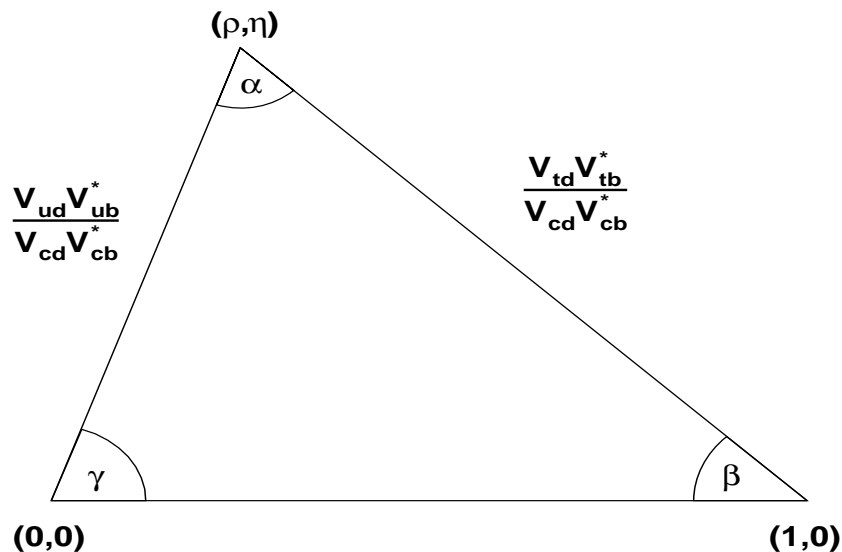


Figure 3.1: The Unitarity Triangle

The Unitarity Triangle has all the sides normalised to  $V_{cd}V_{cb}^*$  so that the lowest side has unit length. In addition a phase convention is usually chosen so that  $V_{cd}V_{cb}^*$  is real, thus aligning the lower side with the real axis. The upper vertex has the coordinates of  $\rho$  and  $\eta$ .

The primary goal of the BaBar experiment, and the rival Belle experiment at the KEK laboratory in Japan, is to measure  $\sin 2\beta$ . The experiments are in agreement giving measurements of

$$\sin 2\beta = 0.741 \pm 0.067 \pm 0.034 \text{ (BaBar) [14]}$$

and

$$\sin 2\beta = 0.733 \pm 0.057 \pm 0.028 \text{ (Belle). [15]}$$

CP violation has been observed in both the  $K^0$  and B meson systems to date. However it seems there is not enough CP violation manifest in the CKM matrix to account for the cosmic baryon-antibaryon asymmetry. It is therefore widely believed that further sources of CP violation will be part of any extension of the Standard Model. The next chapter will give an overview of the relation between the cosmic baryon-antibaryon asymmetry and CP violation, followed by a discussion of the types of extensions that lead to observable CP violating effects in semi-leptonic tau decays.

# Chapter 4

## CP Violation Beyond the Standard Model

To date no antimatter has been observed in nature except as a product of the interactions of matter particles with each other in cosmic ray air showers. Thus it appears the entire Universe is made up of matter rather than anti-matter. It can be shown that for a matter dominated Universe there must be:

- baryon number violation;
- CP violation at the relevant epoch;
- a departure from thermal equilibrium.

These conditions are known as the Sakharov conditions [16]. The first one is clearly needed to allow processes that produce more baryons (anti-baryons) than anti-baryons (baryons). CP violation is required in order that the process producing

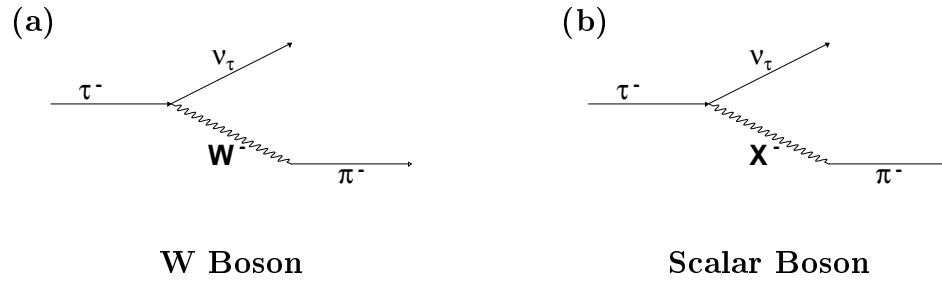


Figure 4.1: Tau Decays via Vector and Scalar Bosons

an excess of baryons does not occur at the same rate as the process producing an excess of anti-baryons. Finally, because it can be shown [16] that, in thermal equilibrium, baryon number ( $B$ ) is not sensitive to the difference between the number of baryons and anti-baryons, a departure from thermal equilibrium is also required.

CP violation has been observed in the  $K^0$  and  $B$  meson systems. The models including the Sakharov conditions typically require larger amounts than that contained in the CKM matrix. It is important, therefore, to look for CP violation from non-CKM sources from, for example, mixing in the neutrino sector or hypothetical scalar bosons that can be added to the Standard Model.

If there are further scalar bosons in nature it opens the possibility of interference between Standard Model processes and those involving scalar bosons. Figure 4.1 shows, on the left, how the tau decay proceeds in the Standard Model. It decays into a neutrino and a  $W$  vector boson. The boson then decays into final state particles illustrated by a single pion state here. On the right the corresponding diagram for an extension to the Standard Model is shown. The only difference is that the  $W$  boson is replaced by a charged scalar boson,  $X$ .

Each process has a weak phase associated with it denoted by  $\delta_W$  and  $\delta_X$  respectively. If the final state contains multiple mesons then each diagram will also have strong phase factors,  $\phi_W$  and  $\phi_X$ , due to the interactions between the mesons. (The strong phases are dependent on the angular momentum of the final state and therefore differ in the scalar and vector currents). The full decay amplitude is given by

$$|A_W|e^{i\phi_W}e^{-i\delta_W} + |A_X|e^{i\phi_X}e^{-i\delta_X}. \quad (4.1)$$

The square of this amplitude and its CP conjugate are

$$|A_W|^2 + |A_X|^2 + 2|A_W||A_X|\cos((\phi_X - \phi_W) - (\delta_W - \delta_X)) \quad (4.2)$$

and

$$|A_W|^2 + |A_X|^2 + 2|A_W||A_X|\cos((\phi_X - \phi_W) + (\delta_W - \delta_X)). \quad (4.3)$$

The CP violation manifests itself in the interference term of the probability distribution. If there were no strong phase factors the interference term would be identical in both distributions and there would be no observable CP violation. It is therefore a requirement to have more than one meson in the final state in order to observe CP violation.

## 4.1 Scalar Boson Models

There are many different ways to add scalars to the Standard Model. However if one is to conserve the known symmetries in the Standard Model, and be able to observe CP violation via interference between Standard Model and non-Standard

Model diagrams in tau decays, then the number of models is reduced to four [17]. One model is the Multi Higgs Doublet Model (MHDM model) and the other three models involve Scalar Leptoquarks (SQL models).

Only the MHDM model is considered in this thesis primarily because the calculations and Monte Carlo simulations of the model already exist. This allows efforts to be concentrated on the measurement of the CP violating effect.

The MHDM extends the Standard Model by adding two extra Higgs doublets, and the Lagrangian for the Yukawa couplings, which in the Standard Model is given by equation 2.29, is

$$\mathcal{L}_{MHD} = \bar{Q}_{L_i} F_{ij}^D \Phi_d D_{R_j} + \bar{Q}_{L_i} F_{ij}^U \tilde{\Phi}_u U_{R_j} + \bar{L}_{L_i} F_{ij}^E \Phi_e E_{R_j} + h.c \quad (4.4)$$

where  $Q_{L_i}$  are left-handed quark doublets,  $L_{L_i}$  are left-handed lepton doublets,  $D_{R_i}$  are right-handed down quark singlets,  $U_{R_i}$  are right-handed up quark singlets and  $E_{R_i}$  are right-handed charged lepton singlets. The index  $i$  runs from 1 to 3 and labels the particle generation. The  $\Phi$  are the Higgs doublets where  $\Phi_d$  couples to down quarks,  $\Phi_u$  couples to up quarks and  $\Phi_e$  couples to charged leptons. The  $F$  matrices are standard Yukawa coupling matrices.

The MHDM Lagrangian is invariant under the simultaneous transformations

$$\phi_d \rightarrow -\phi_d \quad (4.5)$$

and

$$D_{R_j} \rightarrow -D_{R_j}. \quad (4.6)$$

The equivalent transformations in the latter two terms of 4.4 also leave the Lagrangian unaltered.

In analogy with the quark sector the interacting eigenstates rotate into the mass eigenstates via a mixing matrix,

$$\begin{pmatrix} \Phi_d^+ \\ \Phi_u^+ \\ \Phi_e^+ \end{pmatrix} = \begin{pmatrix} c'_1 & s'_1 c'_3 & s'_1 s'_3 \\ -s'_1 c'_2 & c'_1 c'_2 c'_3 + s'_2 s'_3 e^{i\delta'} & c'_1 c'_2 s'_3 - s'_2 c'_3 e^{i\delta'} \\ -s'_1 s'_2 & c'_1 s'_2 c'_3 - c'_2 s'_3 e^{i\delta'} & c'_1 s'_2 s'_3 + c'_2 c'_3 e^{i\delta'} \end{pmatrix} \begin{pmatrix} G^+ \\ H_1^+ \\ H_2^+ \end{pmatrix} = U \begin{pmatrix} G^+ \\ H_1^+ \\ H_2^+ \end{pmatrix}, \quad (4.7)$$

where  $c'_i$  is  $\cos\theta'_i$ ,  $s'_i$  is  $\sin\theta'_i$  and  $\delta'$  is a CP violating phase. The two H fields are charged Higgs bosons and  $G^\pm$  is the Goldstone Boson absorbed by the W boson.

In general one can add N Higgs doublets to the Standard Model. For CP violation to occur in the Higgs sector at least two doublets need to be added. In analogy with equation (3.35) one can perform phase transformations on the  $\phi_i$  and the  $H_i$  leaving one complex phase in the matrix that is responsible for CP violation. The number of phases left over is zero in the case of two Higgs doublets, and so three doublets are required to allow CP violating effects originating in a complex phase in this matrix.

Once the electroweak symmetry is broken and the mass matrices diagonalised the Lagrangian for the charged scalar fields is

$$\mathcal{L}(\phi_i^\pm) = \bar{U}_L V_{CKM} M_d D_R \frac{\phi_1^+}{v_1} - \bar{U}_R M_u V_{CKM} D_L \frac{\phi_2^+}{v_2} + \bar{N}_L M_E E_R \frac{\phi_3^+}{v_3} + h.c. \quad (4.8)$$

where, in accordance with the literature, the neutrinos are assumed massless.  $v_i$  are vacuum expectation values for the  $\phi_i^0$  fields,  $\bar{N}_L$  is the neutrino row vector and  $M_u$ ,  $M_d$  and  $M_E$  are diagonalised mass matrices for up, down and lepton type fermions respectively. After rotating the interacting scalar states into the mass states the Lagrangian is

$$\begin{aligned} \mathcal{L}(H_1^\pm, H_2^\pm) = \sqrt{2\sqrt{2}G_F} \sum_i (\bar{U}_L V_{ckm} M_d D_R X_i H_i^\pm - \bar{U}_R M_u V_{ckm} D_L Y_i H_i^\pm \\ + \bar{N}_L M_E E_R Z_i H_i^\pm) + h.c. \end{aligned} \quad (4.9)$$

where  $G_F$  is the Fermi coupling and the phase factors are given in terms of elements of the mixing matrix  $U$ :

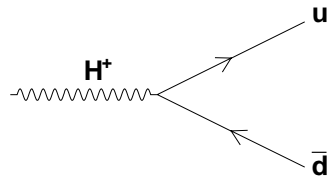
$$X_i = \frac{U_{1i+1}}{U_{11}} \quad (4.10)$$

$$Y_i = \frac{U_{2i+1}}{U_{21}} \quad (4.11)$$

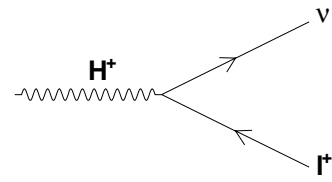
$$Z_i = \frac{U_{3i+1}}{U_{31}} \quad (4.12)$$

Both  $Y$  and  $Z$  contain the complex phase  $\delta$  and so any diagram involving  $Y$  or  $Z$  is CP violating. Making the assumption that only the lightest Higgs couples to fermions we are lead to two new Feynman diagrams describing the charged Higgs interactions illustrated in Figure 4.2. Any tau decay diagram in this scheme involves both  $Y$  and  $Z$ , as can be seen in Figure 4.2, and is therefore CP violating.

New sources of CP violation can appear in extensions to the Standard Model by adding the minimum number of Higgs doublets required to introduce a complex phase. The next chapter will describe the current state of tau lepton physics, concentrating on investigations of CP violating phenomenon.



$$\frac{ig}{2\sqrt{2}m_W}(m_d X(1 + \gamma_5) + m_u Y(1 - \gamma_5))V_{ud}$$



$$\frac{ig}{2\sqrt{2}m_w}m_l Z(1 + \gamma_5)$$

Figure 4.2: Higgs Diagrams

# Chapter 5

## Tau Lepton Physics

The tau lepton was the last of the three charged leptons discovered when it was found in 1975 by the MARK 1 experiment [7]. Martin Perl was awarded the Nobel Prize for this work. Unlike the muon and electron the tau lepton can decay to hadronic final states. Most of these states have low multiplicities providing a clean laboratory to do physics research. In particular the tau is better suited to searches for CP violation in the charged Higgs sector than the corresponding searches in  $B$  meson decays because one is guaranteed to be free of CKM asymmetries in the tau decays.

The tau mass is  $1776.99_{-0.26}^{+0.29}$  MeV and it has a lifetime  $(290.6 \pm 1.1)$  fs. [18] Previously many searches for CP violation in the production of tau pairs have been undertaken.

## 5.1 CP Violation in Tau Production

A stable particle  $N$  has a dipole moment [6]

$$dN = \int x \rho(x) d^3x \quad (5.1)$$

which is even under  $T$  transformations and odd under  $P$  transformations. A particle at rest has the dipole moment orientation proportional to the spin orientation. The spin is odd under  $T$  and even under  $P$ . Therefore if the tau has an electric dipole moment both  $T$  and  $P$  are violated which means  $CP$  is violated if  $CPT$  is conserved. A measure of the tau electric dipole moment therefore provides a measure of  $CP$  violation. New  $CP$  violating interactions at the production vertex involve radiative corrections that induce the tau electric dipole moment. All previous measurements are consistent with a dipole moment, and therefore  $CP$  violation in production, not existing.

## 5.2 CP Violation in Tau Decays

The CLEO collaboration has developed several analysis techniques to study direct  $CP$  violation in tau decays. The first method [2,3] involves measuring asymmetries in the decay mode  $\tau \rightarrow K_S^0 \pi$  where  $K_S^0 \rightarrow \pi^+ \pi^-$ . These asymmetries are given by the expressions

$$A_{CP}^+ = \frac{N^+(\cos \beta \cos \psi > 0) - N^-(\cos \beta \cos \psi > 0)}{N^+(\cos \beta \cos \psi > 0) + N^-(\cos \beta \cos \psi > 0)} \quad (5.2)$$

and

$$A_{CP}^- = \frac{N^+(\cos \beta \cos \psi < 0) - N^-(\cos \beta \cos \psi < 0)}{N^+(\cos \beta \cos \psi < 0) + N^-(\cos \beta \cos \psi < 0)} \quad (5.3)$$

where  $\beta$  is the angle in the  $K_S^0$  rest frame between one of the charged pions from the  $K_S^0$  decay and the  $K_S^0$ , and it is given by

$$\cos \beta = \frac{m_{K_S^0}}{\sqrt{m_{K_S^0}^2 - 4m_\pi^2}} \frac{E_{\pi^-} - E_{\pi^+}}{|\vec{P}_{\pi^-} + \vec{P}_{\pi^+}|} \quad (5.4)$$

The other angle,  $\psi$ , is the angle in the  $3\pi$  (i.e.  $K_S^0\pi$ ) rest frame between the direction of the laboratory frame,  $\vec{n}_L$ , and  $\vec{n}_\perp$ .

$N^+$  and  $N^-$  are the number of  $\tau^+$  and  $\tau^-$  decays respectively. The measured asymmetries in the  $\tau \rightarrow K_S^0\pi$  with  $K_S^0 \rightarrow \pi^+\pi^-$  are shown in Table 5.1 where the signal

	$A_{CP}^+$	$A_{CP}^-$
Signal	$0.058 \pm 0.023$	$0.024 \pm 0.021$
Sideband	$0.049 \pm 0.030$	$0.034 \pm 0.033$

Table 5.1: Measured CP Asymmetries in Signal and Sideband [2, 3]

is defined to be the region of the  $\pi^+\pi^-$  mass spectrum within 20 MeV of the  $K_S^0$  mass and the two sidebands the outer regions each spanning 30 - 100 MeV above and below the  $K_S^0$  mass. Although a CP asymmetry is found in the signal region it is also present in the sidebands suggesting an unknown detector effect is responsible.

Another method is to construct a CP odd observable which will have a sign change between  $\tau^+$  and  $\tau^-$  decays if CP violation is present. The sensitivity of the observable can be maximised if the relative statistical error is minimised. The statistical

error on such an observable  $\epsilon$  for  $N$  events is [19]

$$\sigma_{\langle\epsilon\rangle} = \sqrt{\frac{\langle\epsilon^2\rangle - \langle\epsilon\rangle^2}{N}} \quad (5.5)$$

The sensitivity is defined to be

$$S = \frac{\langle\epsilon\rangle}{\sigma_{\langle\epsilon\rangle}} = \frac{\int \epsilon P dLIPS}{\sqrt{\frac{\langle\epsilon^2\rangle - \langle\epsilon\rangle^2}{N}}} \quad (5.6)$$

where  $dLIPS$  is the Lorentz Invariant Phase Space (LIPS) and  $P$  is the probability density. Dividing the probability density into CP odd and even terms ( $P = P_{odd} + P_{even}$ ) the sensitivity is given by

$$S = \sqrt{N\Gamma R} \quad (5.7)$$

where  $\Gamma$  is  $\int P dLIPS$  and  $R$  is

$$R = \frac{(\int \epsilon P_{odd} dLIPS)^2}{\int \epsilon^2 (P_{even} + P_{odd}) dLIPS}. \quad (5.8)$$

However  $\epsilon^2 P_{odd}$  is an odd function and so the integral over this vanishes and  $R$  simplifies to

$$R = \frac{(\int \epsilon P_{odd} dLIPS)^2}{\int \epsilon^2 P_{even} dLIPS}. \quad (5.9)$$

In the expression for the sensitivity only  $R$  depends on the CP observable. Therefore the optimal observable is the one which maximises  $R$  and using the calculus of variations it can be shown that [19] the optimal observable is

$$\epsilon = \frac{P_{odd}}{P_{even}}. \quad (5.10)$$

The calculation of such an observable for  $K_S^0\pi$  decays is described in Appendix A. CLEO found using the Optimal Observable method, applied to  $K_S^0\pi$  decays with  $K_S^0 \rightarrow \pi^+\pi^-$ , that the imaginary part of the Higgs coupling is in the range [20]

$$-0.172 < \Im(\Lambda) < 0.067 \quad (5.11)$$

at 90 % Confidence Level (CL). In addition the measurement was done using correlated  $\rho$  decays (i.e both taus decay into the  $\rho$  resonance), thereby increasing the sensitivity of the  $\rho$  channel because the spin dependent terms in the observable are retained in the intergration over dLIPS. The result was

$$-0.046 < \Im(\Lambda) < 0.022 \quad (5.12)$$

at 90 % CL. A third method was employed using the helicity angles of the decays. The helicity angle ( $\theta_{\pi\pi}$ ) is the angle between the direction of the charged pion in the  $\pi\pi^0$  rest frame and the direction of the  $\pi\pi^0$  in the tau rest frame. In the Standard Model this has a distribution

$$\frac{dN}{d \cos \theta_{\pi\pi}} \sim a + b \cos^2 \theta_{\pi\pi} \quad (5.13)$$

and in the presence of scalar mediated tau decays this becomes

$$\frac{dN}{d \cos \theta_{\pi\pi}} \sim a + c_1 \Re(\Lambda) \cos \theta_{\pi\pi} + c_2 \Im(\Lambda) \cos \theta_{\pi\pi} + b \cos^2 \theta_{\pi\pi}. \quad (5.14)$$

Using this method the coupling is constrained as

$$-0.033 < \Im(\Lambda) < 0.089 \quad (5.15)$$

at 90 % CL.

The CLEO collaboration has performed several CP violation measurements using tau decays and these show no evidence of CP violation. No other collaboration has published these measurements to date. The next chapter describes the BaBar experiment which is the detector used to make the CP violation measurement in this thesis.

# Chapter 6

## Experimental Apparatus

The BaBar experiment located at the Stanford Linear Accelerator Center (SLAC) has collected an unprecedented number of tau decays. The analysis described in this thesis uses  $124 \text{ fb}^{-1}$  of data, and BaBar is rapidly heading beyond  $200 \text{ fb}^{-1}$  of data. The integrated luminosity as a function of time is shown in Figure 6.1.

BaBar [21] is a detector placed at the collision focus of the PEP-II colliding beam facility which consists of a two mile linear accelerator and two storage rings one on top of the other. This is illustrated in Figure 6.2. One ring carries the 9 GeV electron beam and the other the 3.1 GeV positron beam. The energies of the beams are dissimilar so that the resulting particles are boosted in the laboratory, allowing the decay lengths, lifetimes and time dependence of decay rates of  $B$  mesons to be measured. The time dependent decay rates of  $B$  mesons provide an important test of CP symmetry.

Magnets are used to bend the beams from the end of the linear accelerator around

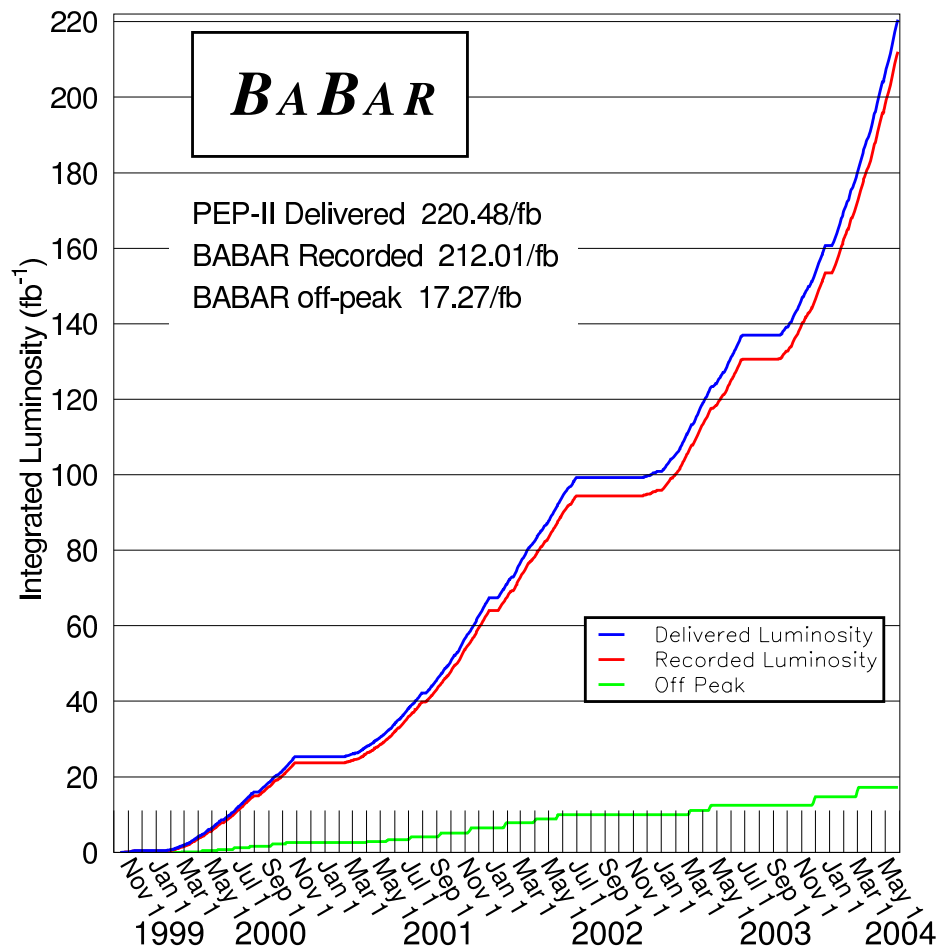


Figure 6.1: Integrated Luminosity Collected by BaBar

the storage rings to a collision point inside the BaBar detector. By the time of the collision the beams are focused into a very narrow beam so increasing the density of particles and hence the luminosity at the BaBar detector. The beams are designed

to collide at 10.58 GeV in the center of mass frame producing a  $\Upsilon(4s)$  resonance which decays to a pair of  $B$  mesons with a branching fraction of 96% [22]. The cross-section for tau pair production at an energy of 10.58 GeV is almost as high as that for  $B$  meson production leading to the production of a large tau pair sample. The cross-sections for production of fermion pairs at a centre of mass energy of 10.58 GeV are shown in Table 6.

The PEP II facility was designed to provide a luminosity of  $3 \times 10^{33} \text{ cm}^{-2} \text{ s}^{-1}$  and has achieved  $9.213 \times 10^{33} \text{ cm}^{-2} \text{ s}^{-1}$ . In 2004 PEP II started running using double trickle [23] injection. In the initial four years when the bunches of electrons (positrons) in the beams were depleted the BaBar detector had to stop taking data whilst further bunches were injected, a strategy known as topping off the beams, because the beam backgrounds were too high. Now, when PEP II is run in trickle injection mode bunches are continuously injected into the beams, and the backgrounds brought under control quickly allowing data to be taken continuously.

Data Sample	Cross-section (nb)
$\tau^+\tau^-$	0.89
$\mu^+\mu^-$	1.16
$B^+B^-$	0.525
$B^0B^0$	0.525
$\bar{c}c$	1.30
$\bar{u}u, \bar{d}d, \bar{s}s$	2.09

Table 6.1: Cross-sections of Different Processes [4]

The BaBar detector consists of several components which have to take into account the physics requirements of the experiment. The main design goals of the

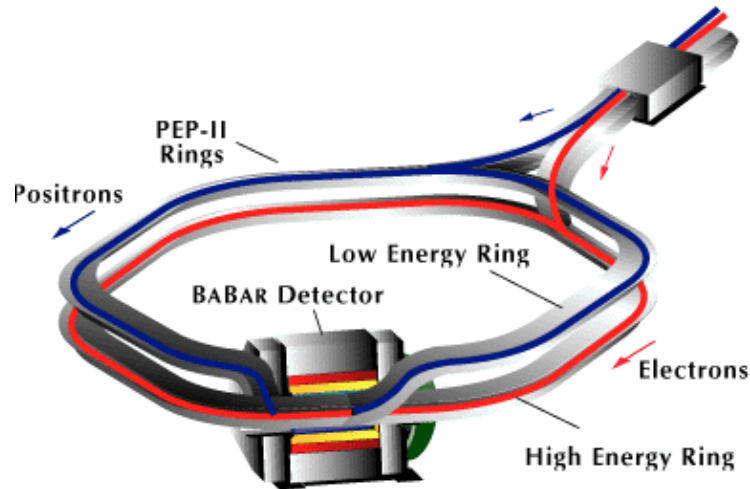


Figure 6.2: The PEP rings at SLAC

detector are:

- to fully reconstruct the decay products of particle decays which requires a large, uniform acceptance down to low polar angles relative to the boost direction. In addition a high reconstruction efficiency is needed for charged particles down to 60 MeV and photons down to 20 MeV;
- to have good energy and angular resolution in the detection of photons from  $\pi^0$  and  $\eta^0$  decays, and from radiative decays in the range from 20 MeV to 4 GeV;
- to have excellent vertex resolution in the  $z$  and  $x$  directions (the coordinate system is defined such that the  $z$ -axis runs almost parallel to the beam axis, being displaced in the phi direction by 2.6 mrad, and the  $x$  and  $y$  directions orthogonal to the  $z$ -axis)
- to have a high efficiency in electron and muon identification. This is particularly important for analysis of tau decays because typically one tau is required

to decay into an electron or muon to suppress hadronic backgrounds;

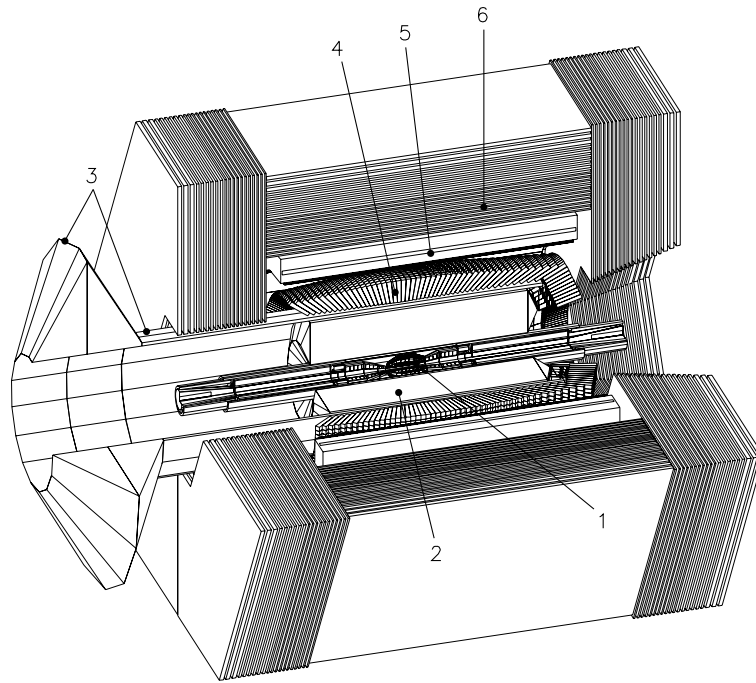


Figure 6.3: The BaBar Detector

1. Silicon Vertex Tracker (SVT)
2. Drift Chamber (DCH)
3. Detector of Internally Reflected Cherenkov Light (DIRC)
4. Electromagnetic Calorimeter (EMC)
5. Superconducting Coil
6. Instrumented Flux Return (IFR)

To achieve these design goals 5 sub-detector components are employed, as shown in Figure 6.3 together with the superconducting coil.

## 6.1 The Silicon Vertex Tracker (SVT)

This is used to find the position of tracks and can detect charged particles to below a  $P_t$  (transverse momentum) of 120 MeV (unlike the drift chamber which cannot

detect particles in this low energy regime). Therefore the SVT is the sole tracking device for tracks below a  $P_t$  of 120 MeV.

The tracks from neutral decays (e.g.,  $B^0 \rightarrow D^+D^-$  and  $K_S^0 \rightarrow \pi^+\pi^-$ ) must have their production vertices measured accurately. The typical distance to the  $D$  production vertex in the  $x-y$  plane is  $270 \mu m$  and so the SVT must provide a resolution better than  $100 \mu m$ .

This sort of detector works using the fact that incident charged particles cause ionisation in the form of electron-hole pairs. The detector contains many layers of arrays of double sided silicon strip sensors, arranged in five concentric layers, which detect the pairs. Each sensor has phi measuring strips on one side running parallel to the beam axis, and z measuring strips on the other side running transverse to the beam axis.

Each layer is divided by azimuth angle into modules. The inner three layers have six barrel modules each. The next layer has 16 arch modules and the outer layer 18 arch modules. The outer layers have an arch design to increase solid angle coverage without increasing the amount of silicon required, and increase the crossing angle for tracks near the edge of the acceptance. The differing shapes of modules are illustrated in Figure 6.4 and a longitudinal cross-section of the SVT is shown in Figure 6.5.

The inner three layers provide position and angular information to be used for vertexing. These layers are mounted very close to the beam-pipe so that the vertex can be extrapolated from genuine tracks, and not tracks due to multiple scattering, as

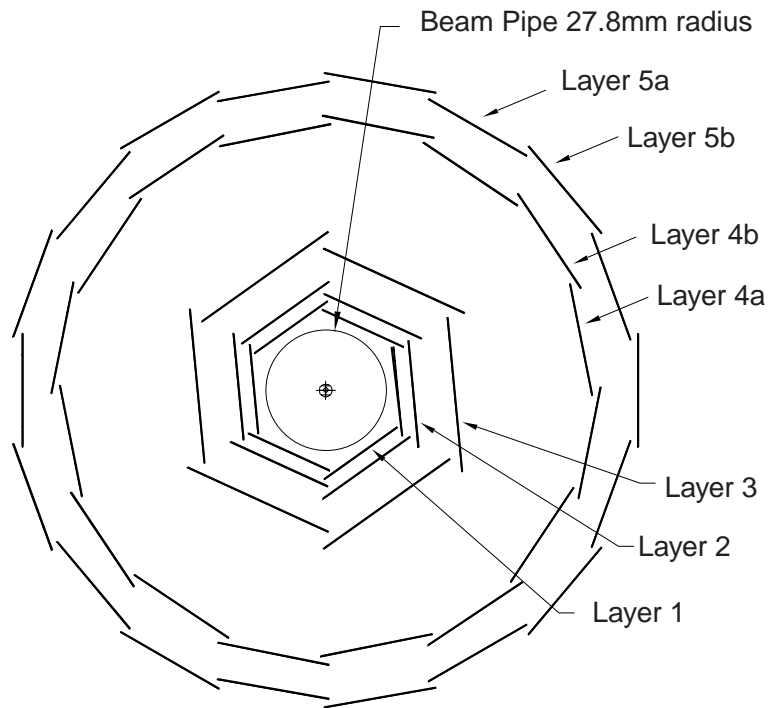


Figure 6.4: The SVT Layers

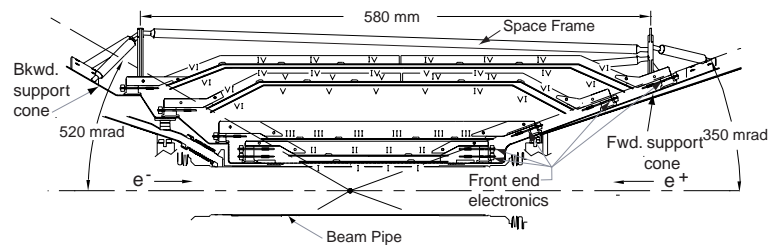


Figure 6.5: Longitudinal Cross-Section of SVT

far as possible. These layers are overlapping to ensure complete azimuthal coverage. The remaining two outer layers are placed much further from the beam-pipe, and measure position and angular information used to link tracks measured in the SVT and DCH.

The front end electronics of the SVT are known as a Time Over Threshold Machine (ATOM). The signals from these chips are compared with a threshold and the time interval - the time over threshold (TOT) - during which the signal exceeds the threshold is proportional to the logarithm of the induced charge. The TOT is stored in a buffer and is read by the data acquisition system (DAQ) on receipt of a read command from the DAQ at which point the data (4 bits for the TOT, 5 bits for the time-stamp and 7 bits for the strip position) is sent to the readout modules (ROMs). The data acquisition, digitisation, buffering and readout occur simultaneously due to the high BaBar trigger rate.

### **Alignment of the SVT**

In order to study the alignment of the SVT two analyses are undertaken. First the positions of the strips are measured relative to each other to perform the local alignment which is relatively stable. This means that the alignment need only be updated after events such as a detector access or magnet quench. Di-muon events, cosmic rays and isolated high momentum tracks (from hadronic decays) are used to do this calibration. The cosmic rays ensure the systematic due to imprecise knowledge of the beam momenta is reduced. This alignment is independent of the DCH as no information from the DCH is used. Information from an optical survey of the SVT, undertaken prior to assembly, is used to constrain the positions of sensors in the sensor plane relative to one another. The hit residuals from the tracks in the event and the optical survey information are used to form a  $\chi^2$  for each sensor which is minimised with respect to the sensors parameters. The constraints from the overlapping sensor regions, the di-muon fit, the cosmic rays and the optical survey are used to form the alignment constants

Secondly the global alignment, in which the whole SVT is aligned with respect to the DCH coordinate system, is performed. This is less stable, needing to be updated run by run, but less complex. Tracks with enough SVT and DCH hits are fit twice: once with SVT only information and once with DCH only information. By minimising the difference between the track parameters in the two fits, the six global alignment parameters (three translations and three rotations) are determined. This alignment is performed once per run, and a given run will use the global alignment constants from the previous run in the track reconstruction. This is known as a rolling calibration. The global alignment is stable to within  $100 \mu m$  over several weeks, although sudden changes can occur during a detector access for example.

### **Performance of the SVT**

The efficiency of the SVT is calculated for each half module by taking the ratio of the number of hits to the number of tracks crossing the active area of the module. The efficiency in working readout sections is 97%. Single dead channels will not affect the efficiency because tracks usually deposit charge in more than one strip.

The distance, in the plane of the sensor, between the track trajectory and hit of high momentum tracks in two prong events is used to determine the spatial resolution. The hit resolution is determined by subtracting the uncertainty due to the track trajectory from the width of the residual distribution. The measured hit resolutions in  $z$  and  $\phi$  for the 5 layers is shown in Figure 6.6.

The SVT provides more accurate angular information than the DCH. This is impor-

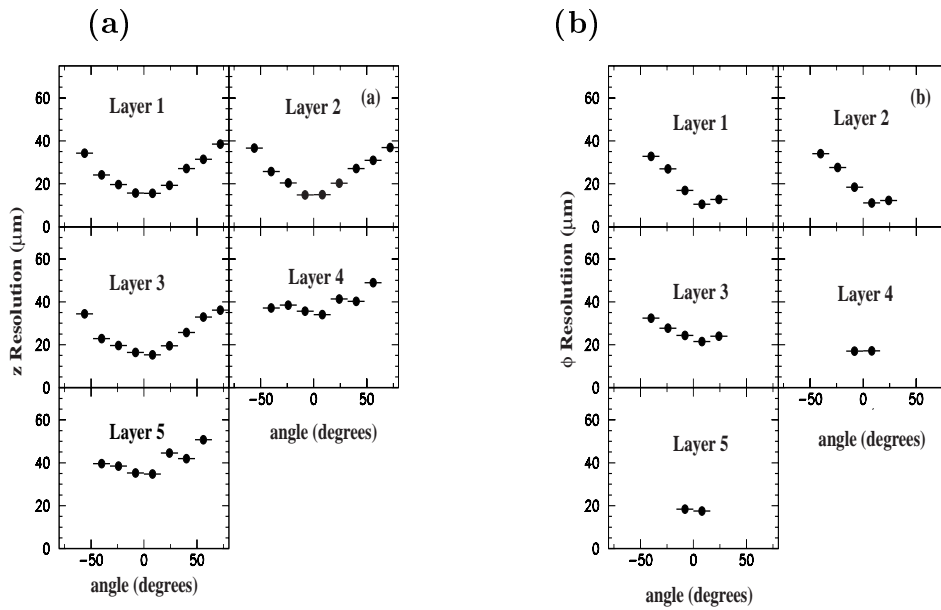


Figure 6.6: SVT Hit Resolution in (a)  $z$  and (b)  $\phi$

tant for the DIRC which relies on an accurate measurement of the angles of tracks intersecting the DIRC. This is because the Cherenkov angle is calculated from the track parameters, as measured in the SVT/DCH, and the photon angles inside the DIRC.

## 6.2 The Drift Chamber

This is used to provide most of the information on particle momentum and can also be used in particle identification (PID) using energy loss measurements. It uses the same principle as the SVT, and the main difference is that the DCH uses electron-ion

pairs rather than electron-hole pairs.

The electrons released in ionisation processes cause secondary ionisation, leading to an avalanche of electrons which is collected on the anodes, some of 35000 wires strung the length of this cylindrical detector, as a signal. The main component of the gas that fills the DCH is helium, an inert gas of low atomic number, to minimise multiple scattering. Isobutane is also added to the chamber to quench secondary ionisation that would otherwise cause runaway avalanches. Low mass (aluminium) wires are used to minimise multiple scattering. The curvature of a track in the magnetic field gives a measure of the track momentum.

For low momentum tracks the DCH dominates the error on the extrapolation of tracks to the EMC, IFR and DIRC. It must be able to measure the transverse momentum and position, including the longitudinal position with a precision of 1 mm, in order to reconstruct longer lived  $K_S^0$  particles. At lower momentum the  $dE/dx$  measurement in the DCH is used for particle identification (PID). A 7% resolution is required to achieve  $\pi/K$  separation up to 700 MeV which complements the DIRC measurement in the barrel region. At the far forward and backward regions the DCH is the sole provider of energy loss information. The layout of the DCH is illustrated in Figure 6.7.

The DCH electronics records the drift time, the integrated charge and an address for each wire (with a signal). The position of the primary ionisation clusters corresponds to the leading edge of the amplified signal which is caused by the charge arriving at the wire, and this is digitised with a 1 ns resolution. A feature extraction algorithm, developed for the drift chamber, converts the raw data into a drift time, the total charge and a status word. Both the time and charge are corrected on an individual

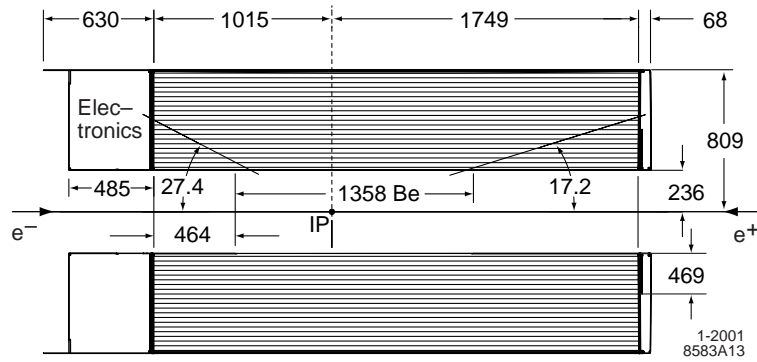


Figure 6.7: Longitudinal section of the DCH

channel basis for time offsets, pedestals and gain constants. A threshold of 2-3 electrons is used to reduce noise. This all takes around  $1 \mu\text{s}$  reducing the data to a quarter of its size.

### DCH Performance

Cosmic-ray data are used to calibrate the time-to-distance (the relation between drift time and drift distance) and  $dE/dx$  measurements. Di-muon data are used to determine the time-to-distance relationship. The drift signal for each particle is estimated by calculating the distance of closest approach between the track and the wire. Any bias is removed by not using the hit on the wire in consideration. The estimated drift distances and times are averaged over all wires in a layer, and a sixth-order Chebychev polynomial is fitted. An additional correction, a tenth order Chebychev polynomial of the drift distance with coefficients varying with entrance angle, is used to account for varying track entrance angle.

The energy loss,  $dE/dx$ , for charged particles is derived from the total charge deposited in each cell of the drift chamber. The energy loss per track is defined to be

the mean of the lower 80% of all the individual  $dE/dx$  measurements. Corrections must be applied to account for changes in gas pressure and mixture; differences in cell geometry and charge collection; signal saturation due to space charge buildup; non-linearities in the most probable energy loss at large track dip angles; and changes in cell charge collection as a function of track entrance angle. The corrections are all done once for a given High-Voltage (HV) setting and a given gas mixture whilst the gain correction must be updated run by run. Although corrections at the cell level can be large compared to the  $dE/dx$  resolution for a single cell the effects of the corrections are reduced on the averaged  $dE/dx$  measurement used for the track. The distribution of corrected  $dE/dx$  measurements as a function of track momenta are shown in Figure 6.8. The predicted Bethe-Bloch curves, determined from control samples, are superimposed.

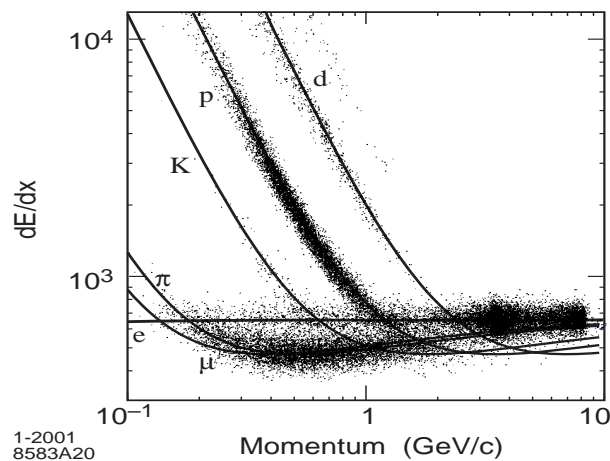


Figure 6.8: Measurement of  $dE/dx$  as a function of track momenta

## 6.3 Charged Particle Tracking Performance

Together the measurements in the SVT and the DCH are used to track the charged particles. This has been studied using cosmic ray muons, di-muon events and tau pair events. Five parameters, and their associated error matrix, are used to describe a charged track:

- the distance of closest approach to the z-axis from the origin of the coordinate system in the x-y plane -  $d_0$
- the distance of closest approach to the z-axis from the origin of the coordinate system in z -  $z_0$
- the azimuthal angle of the track -  $\phi_0$
- the dip angle relative to the transverse plane -  $\lambda$
- the curvature of the track -  $\omega\alpha\frac{1}{p_t}$

A Kalman fitter algorithm [24], that takes into account the detailed distribution of material in the detector and the map of the magnetic field, is used to do the track finding and fitting. The offline track reconstruction uses the information from the Level3 (L3) trigger and the tracking algorithm. First the event start time is refined by performing a fit to  $d_0$ ,  $\phi_0$  and  $t_0$  which is calculated from the four-hit track segments in the DCH superlayers. Helix fits are then performed to the hits found by the L3 track finding algorithm. Additional hits belonging to these tracks are searched for, and  $t_0$  is further improved by only using hits associated with the track. After all the tracks are found any left over tracking segments are used to check for remaining tracks that do not pass through the whole DCH, or not originating at the

IP. Finally the tracks are fit once again using a Kalman filter method.

The tracks are then extrapolated into the SVT, and SVT track segments are added provided the errors on the SVT segments are consistent with the extrapolation. Only those segments with the smallest residuals and largest number of SVT layers are retained. A Kalman fit is then performed to the full set of SVT and DCH hits. Remaining SVT hits are used by two more track finding algorithms. The first reconstructs tracks using triplets of space points (matching  $\phi$  and  $z$  hits) in layers 1, 3 and 5. Consistent space points from other layers are added and if 4 space points (including the initial three) are found the track is considered good. This is efficient over a large range of  $d_0$  and  $z_0$ . The second algorithm takes as input circle trajectories from  $\phi$  hits and adds  $z$  hits to form helices. This is less sensitive to large combinatorics and missing  $z$  information. An attempt is also made to combine tracks only present in the SVT or DCH allowing the recovery of tracks scattered in the material.

### Tracking Efficiency

The absolute DCH tracking efficiency is calculated, using multi-hadron events, by taking the ratio of the number of reconstructed tracks in the DCH to the number of reconstructed tracks in the SVT that are within the DCH acceptance. At 1960 V the efficiency is  $98 \pm 1\%$  per track for tracks above 200 MeV and with  $\theta > 500\text{mrad}$ . At 1900 V the efficiency is reduced by 5%. The error is dominated by the correction for fake tracks in the SVT.

The SVT efficiency is calculated using a sample of  $D^{*+} \rightarrow D^0\pi^+$  decays. These

are selected by reconstructing the decay  $B \rightarrow D^{*+} X$  where  $D^{*+} \rightarrow D^0 \pi^+ \rightarrow k^- \pi^+ \pi^-$ . The difference in mass between the  $K\pi\pi$  system and the  $K\pi$  system, where the low momentum pion is not included, is used to study the SVT efficiency. Figure 6.9 shows a clear enhancement of events when removing the restriction that the low momentum pion was reconstructed in both the DCH and SVT. The resolution of these slow pions is adversely affected by multiple scattering and limited track length. By comparing the pion spectrum in the simulation, using the same event selection as in the data, a comparison may be made and hence the SVT efficiency may be calculated from the simulation because of the good agreement. Both the agreement between data and MC and the SVT efficiency are shown in Figure 6.10.

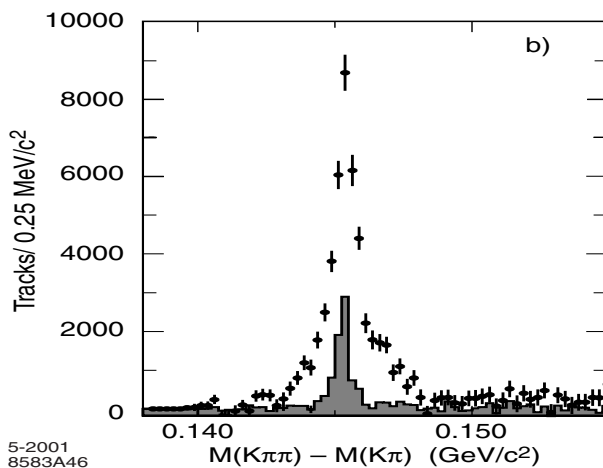


Figure 6.9: Difference in Mass of  $K\pi\pi$  and  $K\pi$  systems for all events (points) and events in which the low momentum pion is reconstructed in both the SVT and DCH (histogram)

### Track Parameter Resolutions

The resolution for the five parameters is monitored in Online Reprocessing (OPR) using Bhabha and di-muon events. Tracks in multi-hadron events and muons in

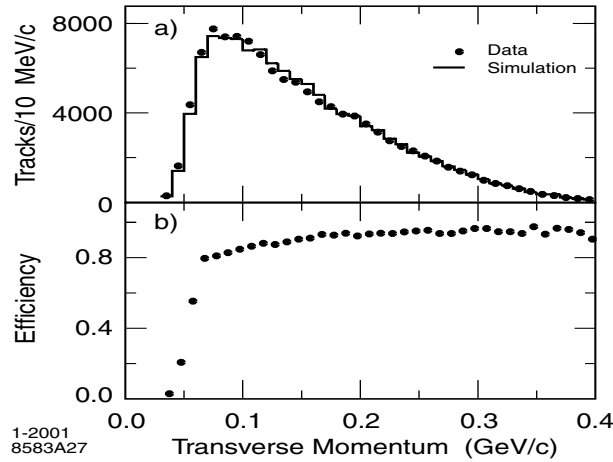


Figure 6.10: Comparison of slow pion momentum spectrum in data and MC (a) and the SVT efficiency (b)

cosmic ray events are used for further analysis offline. The upper and lower halves of cosmic ray tracks traversing both the SVT and DCH are fit separately. The resolution can then be derived from the difference in the measured track parameters for the halves. Resolutions of 23 microns for  $d_0$ , 29 microns for  $z_0$ , 0.43 mrad for  $\phi_0$  and  $0.53 \times 10^{-3}$  for  $\tan \lambda$  are found.

In addition the resolution of  $d_0$  and  $z_0$  are obtained from multi-hadron events. The measured value of the parameter is compared with the coordinates of the vertex constructed from the remaining tracks in the event. These distributions have a positive tail due to the effects of particle decays and so the resolution is extracted from the negative part of this distribution. The resolutions are found to be (at a  $p_t$  of 3 GeV) 25 microns for  $d_0$  and 40 microns for  $z_0$  which are compatible with results obtained from the cosmic ray data. Both the  $d_0$  and  $z_0$  resolutions have a  $p_t$  dependence. Figure 6.11 illustrates this using the multi-hadron data.

Although the SVT dominates angular and position measurements near the IP

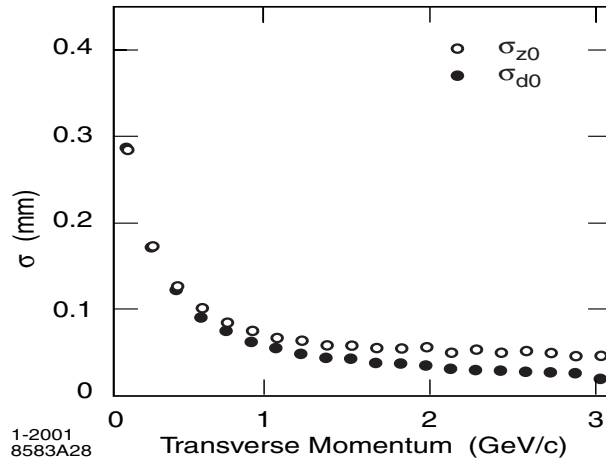


Figure 6.11: Dependence of  $d_0$  and  $z_0$  on  $p_t$  using multi-hadron events

the  $p_t$  measurement is dominated by the DCH and is parameterised by

$$\sigma_{p_t} = (0.13 \pm 0.01)\% \times p_t^2 + (0.45 \pm 0.03)\% \times p_t \text{ GeV} \quad (6.1)$$

where  $p_t$  has units of GeV.

## 6.4 Detector of Internally Reflected Cherenkov Light

BaBar uses a Detector of Internally Reflected Cherenkov Light (DIRC), which contains 156 rectangular quartz bars, to distinguish between different types of particles. This is important because in CP violation studies one of the  $B$  mesons must have its flavour tagged via the decay  $b \rightarrow c \rightarrow s$  whilst the other  $B$  decay is fully reconstructed. Most of the kaons used for flavour tagging are below 1 GeV although some may have momenta as high as 2 GeV. In addition it is important to be able

to, for example in  $B \rightarrow K\pi$  decays, separate kaons and pions. In these types of rare B decays the pions typically have momenta in the range 1.7 to 4.2 GeV which is strongly correlated to polar angle.

The BaBar Particle Identification (PID), i.e the DIRC, system was designed to be thin and uniform in radiation lengths so as to minimise the degradation of the energy resolution in the Electromagnetic Calorimeter (EMC) (because the DIRC is located inside the EMC). To keep the cost of the calorimeter down the DIRC must have a small volume. The DIRC was designed to be able to provide pion/kaon separation at the four sigma level, for all tracks originating from B decays, from the pion Cherenkov threshold up to 4 GeV. Below 700 MeV PID relies on the  $dE/dx$  measurements made in the SVT and DCH.

A charged particle traveling through a dispersive medium causes excited atoms in the charged particle's vicinity to become polarised. If the velocity of the particle,  $v$ , is greater than the speed of light in that medium,  $c/n$ , some of the excitation energy will reappear as coherent radiation at an angle  $\theta$  to the direction of motion. The condition for Cherenkov radiation can be written as

$$\beta n > 1 \tag{6.2}$$

where  $\beta = v/c$ . The Cherenkov light will travel at the speed of light,  $c/n$ , and the particle travels at speed  $v$  or  $\beta c$ . Thus the angle between the particle and the Cherenkov light is

$$\cos\theta = \frac{1}{\beta n} \tag{6.3}$$

The angle measures the velocity of the particle. The medium is chosen so that only certain particles travel faster than the speed of light (in the medium). The Cherenkov light is passed down the quartz bars, using the optical process of total internal reflection (TIR), onto photomultiplier tubes. The magnitude of the angles of the photons will be preserved on reflection from a flat surface. This is illustrated in Figure 6.12 showing the layout and trajectories of photons in the DIRC.

Long thin bars, with rectangular cross section, of synthetic fused silica are used

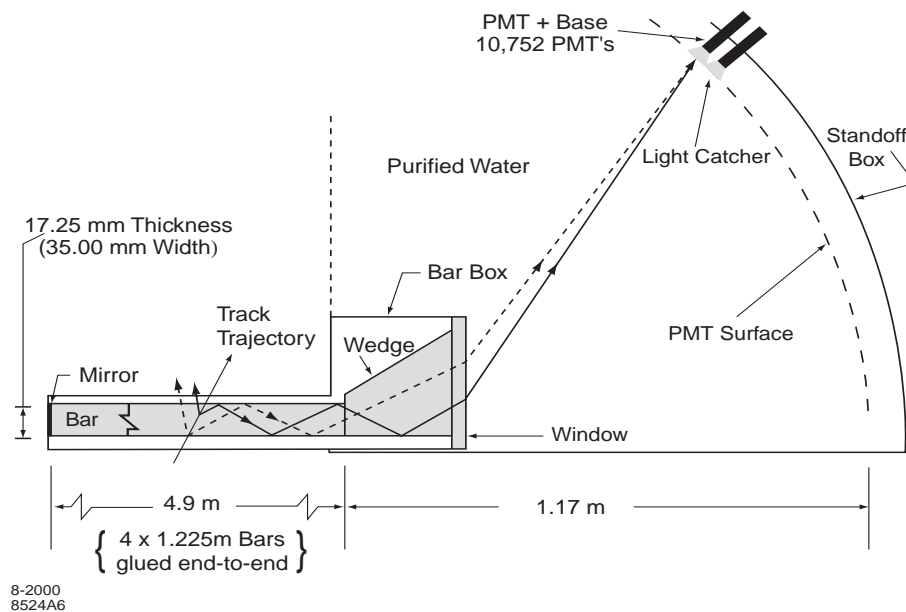


Figure 6.12: Geometry of the DIRC

as the radiator material. The bars are used as radiators and light pipes for the part of the light trapped in the silica. The choice of fused silica is motivated by its resistance to ionising radiation, its long attenuation length, large refractive index, low chromatic dispersion (within the DIRC acceptance) and the high quality optical finish that can be achieved.

The Front End Electronics (FEE), which are mounted on the outside of the stand-off box, are designed to measure the arrival time of a photon with an accuracy only limited by the 1.5 ns transit time spread of the PMTs. The design can cope with the 12  $\mu$ s L1 trigger latency, and can handle background rates of up to 200 kHz/PMT with zero dead time. The DIRC FEE are made up of 168 DIRC Front End Boards (DFBs) each of which processes 64 PMT inputs. The raw data from the DFBs is passed to the ROMs to be processed by a feature extraction algorithm which halves the amount of data passed on. Any data containing errors, typically caused by damaged DFBs that were immediately replaced, is discarded. If a DFB reaches 56% occupancy the dataflow system cannot cope with the amount of data passing through the system. In this case a summary of the occupancy for each DFB is passed through the data system as well as a flag alerting the system to the fact the data was truncated.

### **Calibration of the DIRC**

Two independent analyses are performed to determine the calibration of the PMT time response and the time delays caused by the FEE and fast control system. First a pulser calibration is performed online using a light pulser system. This produces precisely timed light pulses, 1 ns in length, from twelve blue LEDs: one in each sector of the DIRC. To avoid crosstalk pulses in adjacent sectors are set off with a 50 ns separation. Histograms of the recorded PMT times for each pulse are stored in the ROMs and fit to an asymmetric peak function. Typically 65000 light pulses are used to determine the time delay to within an accuracy of 0.1 ns. Secondly reconstructed tracks from the collision data are used. The observed (uncalibrated) arrival time is compared with the expected arrival time. Data equivalent to 100000

tracks are collected and then a calibration is performed with respect to each DIRC channel in which the measured time difference is fit. The second method has a timing resolution 15% better than in the light pulsar method although both methods yield compatible calibrations. The time delay values per channel have rms values stable to within 0.1 ns over a 1 year period.

### **DIRC Performance**

The vector connecting the center of the bar end to the center of the PMT is taken to define the photon propagation angles  $\alpha_x$ ,  $\alpha_y$  and  $\alpha_z$ . The track position and angles are known from the SVT and DCH systems, and so the Cherenkov angles  $\theta_c$  and  $\phi_c$  can be determined up to a 16 fold ambiguity: top or bottom, left or right, forward or backward and wedge or no-wedge reflection. The arrival time of the signal can also be related to the photon propagation angles and serves as a cross-check. The timing information is not as good as the position information, but nevertheless can be used to suppress background from beam induced hits (by a factor of 40) and other tracks in the event.

To distinguish signal and background photons the difference between the measured and expected arrival time is used. It is calculated using the time-of-flight of a track with pion mass hypothesis, the measured time of the PMT signal and the photon propagation time through the bar and standoff box. The time information and restriction on only using physically possible photon paths usually reduces the ambiguities to three-fold.

When a track passes through the DIRC the reconstruction software calculates a like-

likelihood ratio for each particle type ( $e, \mu, \pi, K, P$ ) by maximising the likelihood value for the entire event. If enough photons are found a fit of  $\theta_c$  and the number of signal and background photons is performed for each track.

The resolution on the track Cherenkov angle is given by

$$\sigma_{C,track} = \frac{\sigma_{C,\gamma}}{\sqrt{N_{pe}}} \quad (6.4)$$

where  $\sigma_{C,\gamma}$  is the single photon Cherenkov angle resolution and  $N_{pe}$  is the number of photons detected. The photon Cherenkov angle resolution is calculated to be 10.2 mrad using a di-muon sample. The timing resolution is found to be 1.7 ns and the track Cherenkov angle resolution to be 2.5 mrad. Using the measured single track resolution versus momentum and the expected Cherenkov angles for pions and kaons the pion/kaon separation is  $4.2\sigma$  at 3 GeV as shown in Figure 6.13. A sample of

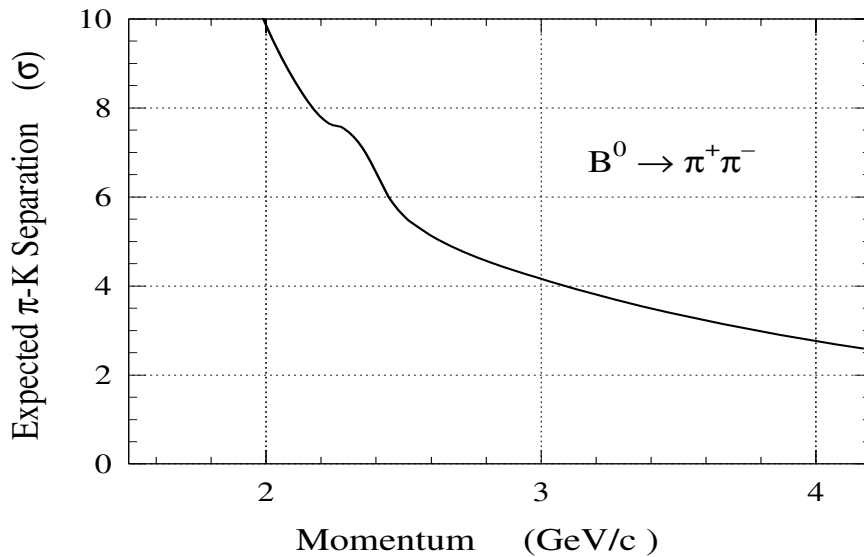


Figure 6.13: Pion/Kaon Separation in the DIRC as a function of momentum

$D^0 \rightarrow K^- \pi^+$  is used to determine the kaon selection efficiency and pion mis-id rate. These are found to be  $96.2 \pm 0.2\%$  (stat.) and  $2.1 \pm 0.1\%$  (stat.) respectively.

## 6.5 The Electromagnetic Calorimeter

A CsI Electromagnetic Calorimeter (EMC) is used to identify and measure electromagnetic showers with high efficiency, good energy and angular resolutions over the range of energies 20 MeV to 9 GeV. This upper bound is determined by the need to measure QED processes, such as  $e^+e^- \rightarrow e^+e^- \gamma$  and  $e^+e^- \rightarrow \gamma\gamma$ , for calibration and luminosity determination. The lower bound results from the requirement to be able to reconstruct  $B$  meson decays, containing multiple  $\pi^0$ s and  $\eta^0$ s, with a high efficiency. Below 2 GeV the  $\pi^0$  resolution is dominated by the energy resolution, whilst at higher energies it is dominated by the angular resolution which is required to be at the few mrad level.

The EMC consists of a cylindrical barrel and a conical forward endcap. It is surrounded by a double Faraday cage, consisting of two 1mm thick Aluminium sheets, to reduce the effects of outside noise on the electronics. The EMC fully covers the azimuthal angle, and the polar angle coverage lies in the range  $15.8^\circ$  to  $141.8^\circ$ . The barrel region contains 5760 Thallium doped Caesium Iodide crystals, trapezoidal in shape, in 48 separate rings each containing 120 crystals. The endcap has 820 crystals in 8 rings.

Data from groups of 24 crystals are sent down a fibre optic cable, one for each group, to the ROM at a 1.5 GB/s rate. The ROM passes the data stream to a

digital pipeline in which pedestal and gain corrections are applied. The calorimeter trigger extracts the output from the pipeline, and upon receipt of a L1 accept signal data samples within a  $1 \mu s$  window are passed to the feature extraction algorithm.

The EMC is maintained at constant temperature because the photodiode leakage current rises exponentially with temperature. In addition the diode-crystal joints suffer stress at higher temperatures caused by thermal expansion. The main causes of heat inside the calorimeter are the preamplifiers and the digitising electronics. The heat from the preamplifiers in the barrel is conducted to a surface directly cooled by Fluorinert. Chilled water is used to cool the digitising electronics. In the endcap a separate Fluorinert system is used to cool both the preamplifiers and the digitising electronics.

### **EMC Calibration**

The light yield of individual crystals varies significantly, is non-uniform and varies with time due to beam generated radiation. The amount of radiation damage is greater at the front of the EMC and therefore a calibration must be performed at different energies, corresponding to different depths in the EMC, to track the effects of radiation damage.

At low energies a flux of low energy neutrons is used to irradiate fluorinert producing 6.13 MeV photons. The fluorinert is pumped from the neutron generator to a thin walled aluminium pipe mounted on front of the crystals. Photons are produced at the rate of 40 kHz per crystal. A fit is done to the produced energy spectrum to obtain the calibration. This is performed each week.

At high energies, in the range 3 to 9 GeV, single crystal calibration is performed using a Bhabha data sample. The deposited cluster energy, as a function of polar angle, is constrained to match the predictions of the Monte Carlo simulation of the EMC. For large numbers of crystals a set of simultaneous linear equations relates the measured energy to the expected energy and so a gain constant is determined for each crystal. This is performed once per month.

The light response of the crystals is monitored on a daily basis using a xenon flash lamp whose light is transmitted down optical fibers to the rears of the crystals. This pulse is similar in spectrum, rise-time and shape to the scintillated light in the crystals. By varying the pulse intensity precise measurements of the linearity of light-collection, conversions to charge, amplification and digitisation are made. The system is stable to 0.15% over a period of one week.

In addition to these calibrations a correction for energy loss due to shower leakage and absorption must be calculated. At low energies less than 0.8 GeV the correction is derived from  $\pi^0$  decays. The true energy of a photon is parameterised as the product of the measured energy and a correction function which depends on  $\ln E$  and  $\cos\theta$ . The two photon mass is constrained to the  $\pi^0$  mass and the coefficients of the correction function are found iteratively. Typically a correction of  $6 \pm 1\%$  is applied where the error is due to uncertainty in the background estimation and the fitting technique.

At higher energies, 0.8 to 9 GeV, single photon Monte Carlo is used. The beam energy, the track momenta of the  $e^+$  and  $e^-$  and the direction of the radiative pho-

ton are used to fit the photon energy. This fitted value is compared to the measured value to extract correction coefficients as a function of  $\cos\theta$  and  $\ln E$ .

### EMC Reconstruction Software

If a group of adjacent crystals scintillate, identified by pattern recognition algorithms, it is indicative of an energy deposit and the group of crystals are labeled a cluster. If there is more than one local energy maximum the cluster is split up and attributed to two deposits close together. Each cluster must have a seed crystal with energy at least 10 MeV. Nearby crystals are added to the cluster if their energy exceeds 1 MeV or if they are contiguous neighbours with at least 3 MeV energy.

To identify a local energy maximum the candidate crystal is required to have an energy,  $E_{LocalMax}$ , which exceeds each of its neighbours and satisfies the condition

$$0.5(N - 2.5) > \frac{E_{NMax}}{E_{LocalMax}}, \quad (6.5)$$

where  $E_{NMax}$  is the energy of one of the neighbouring crystals that has the highest energy above 2 MeV. Clusters are then divided into as many bumps as there are local maxima. Each crystal is given a weight,  $w_i$ , and the bump energy is defined as

$$E_{bump} = \sum_i w_i E_i, \quad (6.6)$$

where  $i$  runs over all the crystals in the cluster. A cluster with a single bump will have all the  $w_i$  equal to one. If there are multiple bumps  $w_i$  is given by

$$w_i = E_i \frac{e^{-\frac{2.5r_i}{r_M}}}{\sum_j E_j e^{-\frac{2.5r_j}{r_M}}}, \quad (6.7)$$

where  $j$  runs over all the crystals in the cluster,  $r_M$  is the Moliere radius, and  $r_i$  is the distance of the  $i$ th crystal from the centroid of the bump. Initially all the weights are set to unity, and then an iterative process is undertaken. In each iteration the centroid position used to calculate  $r_i$  is calculated from the weights of the previous iteration. The iterations continue until the bump centroid position is stable to within 1 mm.

The position of a bump is calculated using logarithmic weights, and the weights are

$$W_i = 4.0 + \ln \frac{E_i}{E_{bump}} \quad (6.8)$$

where only crystals with  $E > 0.0184E_{bump}$  are used (i.e those with positive weights). This ensures only crystals making up the core of the cluster are used. A systematic bias of the calculated polar angle of the crystals is caused by the non-projectivity of the crystals. This is corrected by shifting the polar angle by  $-2.6$  mrad for  $\theta < 90^\circ$  and  $+2.6$  mrad for  $\theta > 90^\circ$ .

By extrapolating tracks from the DCH it is possible to see if the tracks point at any clusters in the EMC. If this is so then the track can be matched with the energy deposit in the EMC. This is known as a charged track. Any other clusters in the EMC are considered to be due to neutral particles.

## EMC Performance

At low energy (6.13 MeV) the EMC energy resolution is measured using the radioactive source. Below 2 GeV the mass resolution of  $\pi^0$  mesons and  $\eta$  mesons, both decaying to two photons of approximately equal energy, is used to deduce the EMC energy resolution. The final measurement is made at 500 MeV using the decay  $\chi_{c1} \rightarrow J/\psi\gamma$ . A fit is performed to the energy dependence giving

$$\frac{\sigma_E}{E} = \frac{(2.32 \pm 0.30)\%}{\sqrt[4]{E}} \oplus (1.85 \pm 0.12)\% \quad (6.9)$$

where E is in units of GeV. These parameters agree with detailed Monte Carlo simulations although they are slightly higher than design expectations. The measured energy resolutions are shown in Figure 6.14.

The angular resolution, the measured values being shown in Figure 6.15, is de-

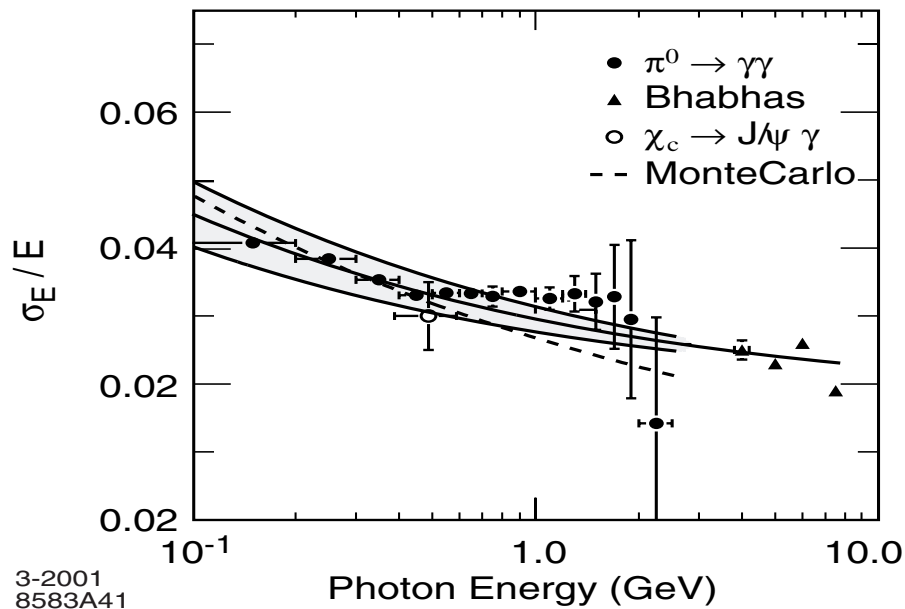


Figure 6.14: The measured energy resolution for various processes.

terminated using  $\pi^0$  and  $\eta$  decays to two photons of approximately equal energy. The

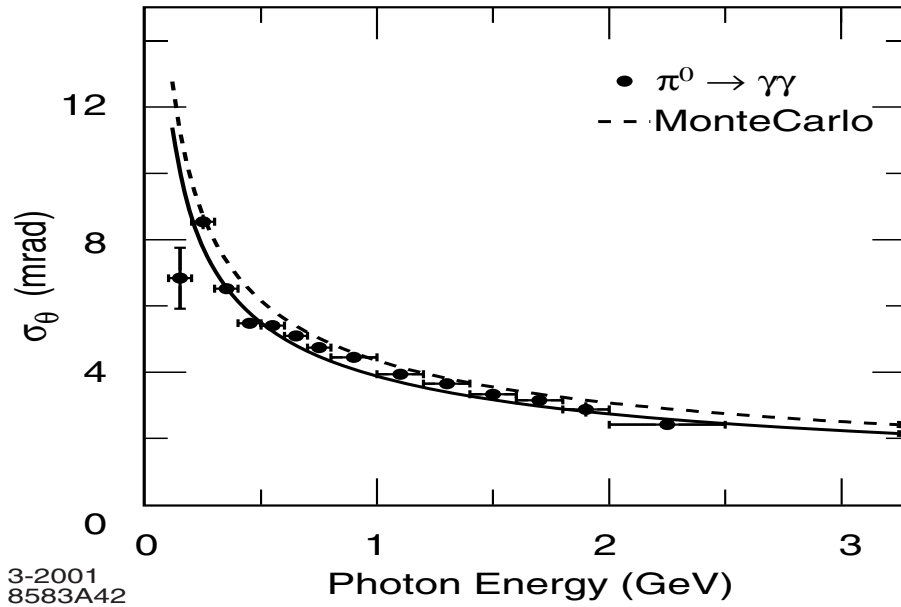


Figure 6.15: The measured angular resolution for various processes.

resolution varies from 3 mrad to 12 mrad over the energy range of the EMC. A fit to the energy dependence leads to the result

$$\sigma_{\theta} = \sigma_{\phi} \left( \frac{3.87 \pm 0.07}{\sqrt{E}} + 0.00 \pm 0.04 \right) \text{ mrad} \quad (6.10)$$

These values are a bit better than is expected from the Monte Carlo simulation.

The two photon mass from  $B\bar{B}$  events is measured, shown in Figure 6.16, to be  $135.1 \text{ MeV}/c^2$ . It is stable to more than 1% over the entire photon energy range. The measured width is  $6.9 \text{ MeV}/c^2$  which agrees well with the Monte Carlo simulation.

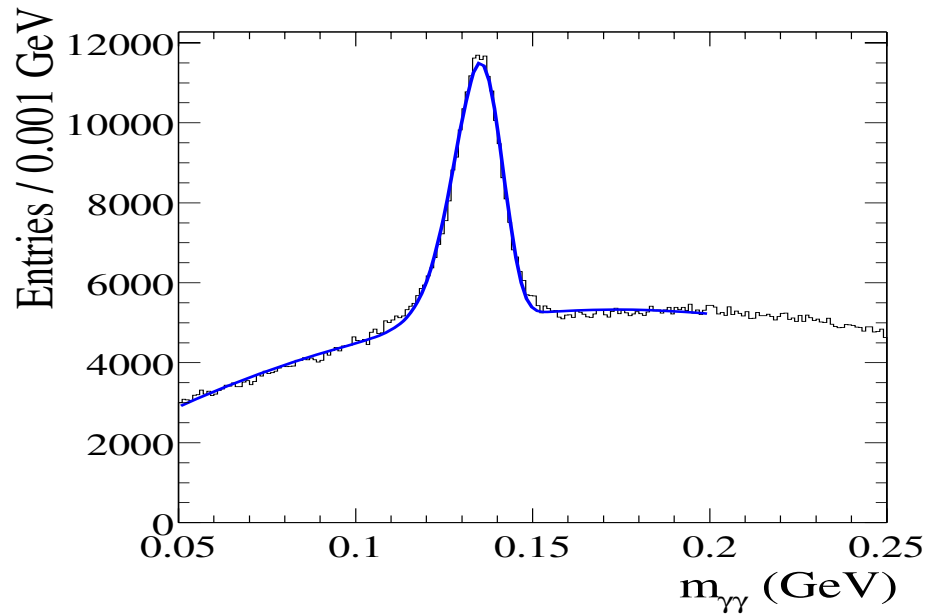


Figure 6.16: The reconstructed  $\pi^0$  mass from two photons events in  $B\bar{B}$  Monte Carlo

## 6.6 The Instrumental Flux Return Barrel (IFR)

This detector is designed to detect muons, with a high efficiency and purity, and neutral hadrons over a wide range of momenta and angles. Muons are important for tagging the flavour of semileptonic neutral  $B$  meson decays, for the reconstruction of vector mesons (eg  $J/\psi$ ), and for the study of rare leptonic  $B$ ,  $D$  and  $\tau$  decays. The detection of  $K_L^0$  allows exclusive  $B$  decays to be studied and the IFR is useful for vetoing charm decays and improving reconstructed neutrinos. The IFR is designed to have a large solid angle coverage, good efficiency, and high background rejection for muons down to below 1 GeV.

The IFR uses the steel flux return of the magnet to filter muons and absorb hadrons. Single gap resistive plate chambers (RPCs) with two-coordinated readout are used

as detectors. The RPCs are placed in between the finely segmented steel layers of the barrel and end doors of the flux return illustrated in Figure 6.17. The segmentation is based on Monte Carlo studies of muon penetration and charged and neutral hadron interactions. The steel is segmented into 18 plates increasing in thickness

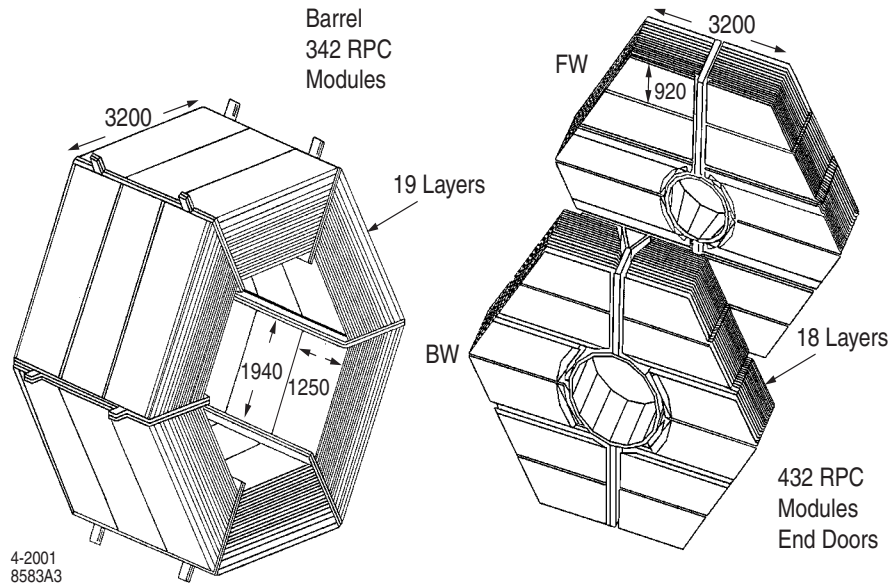


Figure 6.17: The IFR: Barrel Sector and Forward and End Doors

from 2cm at the inner plates to 10 cm for the farthest out plates. The gap between the steel plates is 3.5 cm in the inner layers and 3.2 cm everywhere else. The barrel contains 19 RPC layers and the endcap has 18. Two additional layers are installed between the EMC and the magnetic cryostat so as to detect particles exiting the EMC. In total there are 806 RPC modules, 57 in each of the six barrel sectors, 108 in each of the four half end doors and 32 in the two cylindrical layers. More than 25 different shaped modules were built to fit the modules in with little dead space.

RPCs, one of which is illustrated in Figure 6.18, can detect streamers from ionising particles using capacitive readout strips. The position resolution depends on

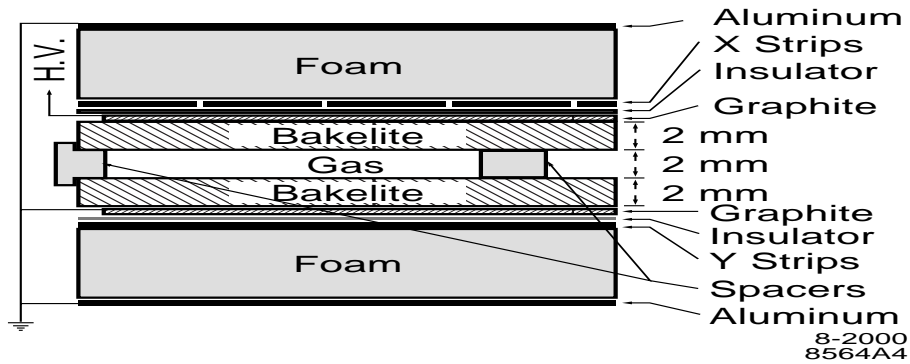


Figure 6.18: Cross section of Planar RPC

the segmentation of the readout, and a precision of a few mm may be achieved.

The planar RPCs have two Bakelite sheets 2 mm thick separated from each other by 2 mm. The gap width remains uniform because polycarbonate spacers are glued to the Bakelite every 10 cm. The gap is filled with a mixture of Argon (57.6%), isobutane (4.5%), and Freon 134a.

The Bakelite is not available in pieces larger than  $320 \times 130 \text{ cm}^2$  and so multiple RPC modules are joined, forming a gap sized chamber. Each module has 32 strips running orthogonal to the beam axis used to measure the  $z$  coordinate. In addition 96 strips run parallel to the beam axis over the three modules which are used to measure  $\phi$ .

The strips are connected to the readout electronics at one end and a  $2 \text{ k}\Omega$  resistor at the other end. In order to minimise signal loss even and odd numbered strips are connected to different front end cards (FECs) because particles usually generates signals on at least two adjacent strips.

The cylindrical RPC is built from four sections each covering a quarter of the circumference. Each section has four sets of two single gap RPCs with perpendicular readout strips. The inner RPC has helical u-v strips running parallel to the diagonals of the module. The outer module has strips parallel to  $\phi$  and z. In each section the strips of the four sets of RPCs in a readout plane are connected to traverse the whole chamber.

### Performance of the IFR

Once a week the efficiency of a chamber is measured chamber by chamber as a function of the applied voltage for cosmic ray muon data sets recorded at several different voltages. The absolute efficiency for the current working voltage is then stored for use by the reconstruction software.

Hits from a given layer and several nearby layers form clusters which are analysed by two algorithms. The first algorithm starts with one-dimensional IFR clusters which are defined to be a group of adjacent hits in one of the two readout coordinates. The cluster position is the centroid of the strips on the cluster. Two-dimensional clusters are then formed from one-dimensional clusters, from the same readout strip, in different layers. Finally in each sector two-dimensional clusters in different coordinates are combined into three-dimensional clusters as long as there are fewer than three layers missing on one of the two coordinates.

The other algorithm also forms one-dimensional clusters whilst defining the position in the same way. Tracks in the DCH are extrapolated to the IFR, and clusters within 12 cm of the extrapolated track are used to form two-dimensional or three-

dimensional clusters.

Straight line fits are done to the two-dimensional clusters. An RPC is efficient if a signal is detected at less than 10 cm from the fitted line in either of the readout planes. Cosmic rays were used to measure the efficiency, once the IFR was installed in BaBar, and 75% exceed an efficiency of 90%. Currently large numbers of RPCs are dead and it is not understood what has caused this. In the summer 2004 shutdown all the dead RPCs will be replaced with Limited Streamer Tubes (LSTs). [25]

To reconstruct muons the charged tracks are required to leave a minimum ionisation energy deposit in the EMC. Charged tracks reconstructed in the tracking system are extrapolated to the IFR taking into account the non-uniform magnetic field, multiple scattering and the average energy loss. The projected intersections with RPC readout planes are computed, and any cluster within a certain distance of this intersection is associated to the track. Several variables are used to distinguish muons from neutral hadrons:

- The total number of interaction lengths traversed from the IP to the last RPC layer with an associated cluster;
- The difference between the measured number of interaction lengths and the predicted number for muons with the same momentum and angles as the charged track;
- The average number and rms value of the distribution of RPC strips per layer;
- The  $\chi^2$  for the geometric match between the projected track and the centroids of clusters in different RPC layers;

- The  $\chi^2$  of a polynomial fit to the two-dimensional IFR clusters.

The performance of muon identification can be evaluated using several control samples, selected with variables not used in the muon identification algorithms, consisting of  $\mu\mu ee$  final states,  $\mu\mu\gamma$  final states, and charged pions from three-prong  $\tau$  decays and  $K_S^0$  decays. In the momentum range 1.5 GeV to 3 GeV the efficiency

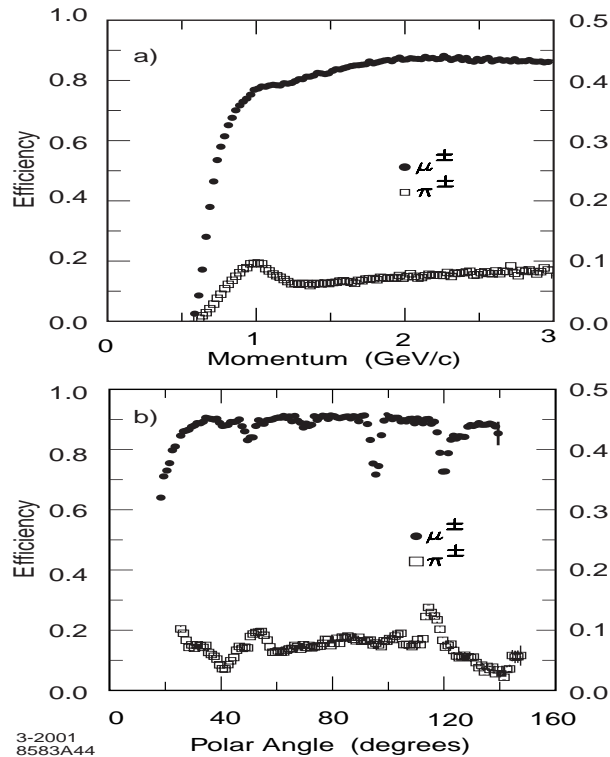


Figure 6.19: Muon efficiency (left scale) and pion mis-id probability (right scale) as functions of momentum and polar angle.

for muon identification is around 90%, shown in Figure 6.19, with a pion fake rate of 6-8%. This can happen because of decays in flight for example. If the muon detection efficiency is relaxed to 80%, by using tighter selection criteria, then the fake rate can be halved.

Neutral hadrons, such as  $K_L^0$ 's, interact in the steel of the IFR and can be identified as clusters that are not associated to a charged track. It is predicted by Monte Carlo simulations that 64 % of  $K_L^0$ 's above 1 GeV will produce a cluster in the cylindrical RPC, or a cluster with hits in at least two planar RPC layers. Unassociated clusters within 0.3 radians of each other are combined into a composite cluster. This joins clusters from showers that have spread into adjacent sectors of the barrel, several sections of the end doors and/or the cylindrical RPC. The direction of the neutral hadron is determined from the event vertex and the centroid of the neutral cluster. It is not possible to measure the energy of the cluster.

Many neutral hadrons interact with the EMC prior to reaching the IFR. Therefore neutral showers in the EMC are associated with the neutral hadrons detected in the IFR, and if a good match in production angles is found the  $\chi^2$  of the match is required to be at least 1%.

A sample of  $K_L^0$ s, produced via  $e^+e^- \rightarrow \phi\gamma \rightarrow K_L^0 K_S^0 \gamma$ , is used to estimate the angular resolution of neutral hadron clusters. The  $K_L^0$  direction is deduced from the missing momentum information in the final state. The resolution is found to be 60 mrad. If the  $K_L^0$  interacts in the EMC then the resolution is doubled. The  $K_L^0$  detection efficiency varies from 20% to 40% over the momentum range 1 GeV to 4 GeV.

## 6.7 Trigger System

The trigger system is designed to select events of interest with a high, stable and well-understood efficiency whilst vetoing background events. The total event rate

must be less than 120 kHz. At the BaBar design luminosity a background rate of 20 kHz is expected for a group of tracks, each having a  $p_t > 120$  GeV, in the DCH or at least one cluster in the EMC with  $E > 100$  MeV. For  $B\bar{B}$  events the total trigger efficiency is required to be at least 99%, and at least 95% for continuum events. For  $\tau^+\tau^-$  the efficiency is required to be between 90% and 95% depending on the tau decay channel considered. The trigger should not contribute more than 1% to dead time and it must be able to cope with dead or noisy electronics.

The trigger system has two main triggers known as the level 1 trigger (hardware based) and the level 3 trigger (software based). The system is designed to cope with up to ten times the projected background at design luminosity. The current BaBar operating luminosity is as much as three times the design luminosity. Therefore a trigger upgrade project is underway so that the level 1 trigger will veto more backgrounds. In particular the new level 1 trigger will make use of the  $z_0$  information, which the current level 1 trigger does not, in order to veto events with tracks originating away from the IP. [26]

### Level 1 Trigger

Normally the level 1 trigger has an output rate of 1 kHz. Triggers are produced within a fixed time of 11-12  $\mu s$  after the electron-positron collision using information from the DCH, EMC and IFR.

The DCH trigger uses the Drift Chamber Trigger (DCT) algorithms. First track segments, their  $\phi$  positions and drift time estimates are found using a set of 24 Track Segment Finder (TSF) modules. The data are passed to the Binary Link Tracker in

which segments are joined to form complete tracks. At the same time the  $\phi$  information from the axial superlayers is used by 8 transverse momentum discriminator (PTD) modules in order to search for tracks above the  $p_t$  threshold.

The Electromagnetic Calorimeter Trigger (EMT) considers the EMC to be divided into 280 towers each covering an area of  $7 \times 40$  theta and phi crystals. All the crystal energies above 20 MeV are summed in each tower, and the result of this is sent to the EMT every 269 ns. The tower data are converted into  $\phi$  maps readable by the Global Trigger (GLT) using ten Trigger Processor Boards (TPBs). The TPBs determine energies in the 40  $\phi$  sectors, summing over various  $\theta$  ranges, compare these energies against thresholds of the eight trigger primitives (types of track (DCH) or types of energy deposit (EMC) ), estimate the time of energy deposition, correct for timing jitter, and finally transmit the result to the GLT.

The IFR Trigger (IFT) triggers in di-muon and cosmic ray events. The IFT considers the IFR to be divided into ten sectors: the six barrel sextants and four half end doors. The inputs to the IFT are the logical OR (Fast OR) of the  $\phi$  readout strips in eight selected layers in each sector. A majority logic algorithm defines trigger objects for every sector in which at least four of the eight selected layers have hits within a 134 ns time frame. The IFR trigger synchronisation module then processes the ten trigger objects constructing a three-bit trigger word (U). U encodes seven exclusive trigger conditions.

The GLT receives the trigger primitives in the form of  $\phi$  maps in addition to data from the IFT. These are combined to form further trigger bits which are passed to the Fast Control and Timing System (FCTS) for the final trigger decision. There

is a different latency for the different primitives, and so the GLT must undertake a time alignment using configurable delays. Next the GLT forms additional combined  $\phi$  maps from the DCT and EMT data. All 16  $\phi$  maps are compared against GLT look-up tables which return three-bit counts of trigger objects within those maps. To be counted as distinct trigger objects the map bits are required to have a separation of more than one  $\phi$  bin. A trigger line is set as the logical AND of the operations, which can be set to always pass or to be compared against a threshold, on the 16 counts and the IFT hit pattern. This is performed for each of the 24 trigger lines. The time of the trigger is derived from the centroid of the highest priority timing distribution.

Typically, for a 1 kHz trigger rate, Bhabha and annihilation events contribute 130 Hz. Cosmic rays contribute a further 100 Hz and random beam crossing triggers 20 Hz. The remaining triggers are due to lost particles in the beam pipe or other components. The distribution of single track  $z_0$  values reconstructed by Level 3 for all Level 1 triggers, shown in Figure 6.20, has prominent peaks at  $z = \pm 20$  cm corresponding to flanges in the beam pipe.

### Level 3 Trigger

The Level 3 trigger software, which runs on the online computer farm in the Online Event Processing (OEP) framework, consists of event reconstruction and classification, a set of event selection filters, and monitoring. The filters have access to the complete event data including the output of the Level 1 trigger processors and FCTS trigger scalars.

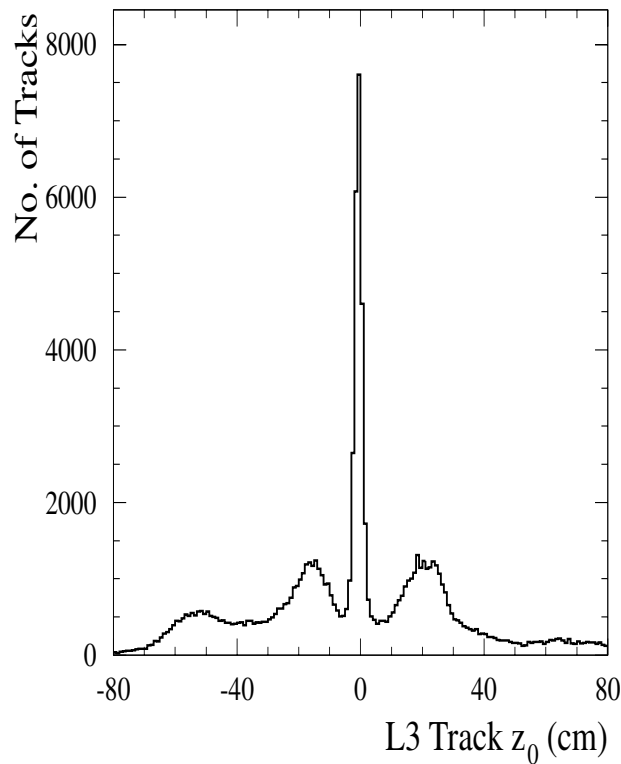


Figure 6.20: Single track  $z_0$  for all Level 1 tracks reconstructed by Level 3

The Level 3 drift chamber algorithm (L3DCH) must reject beam-induced charged particle background produced in material close to the IP. These cannot be rejected by the Level 1 trigger because it does not have sufficient tracking resolution. L3DCH performs track finding (using pattern recognition) and track fitting allowing the 5 helix track parameters to be determined for tracks with  $p_t > 250$  MeV. To maintain a high algorithm speed the track segments from the TSF are used in conjunction with actual DCH data.

The fitting algorithm uses both the matched segments and the actual hits of those segments to fit the helix parameters. The fit is iterated by dropping hits with large residuals and adding hits close to the initially fitted track. The final fit does not demand the track originate at the IP.

The neutral trigger in Level 3 uses EMC information, and is known as L3EMC. L3EMC identifies energy clusters with a sensitivity sufficient to find minimum ionising particles. In order to do this first of all lists of crystals with significant energy deposits are made and clusters are then identified. Typically the EMC will send data (including the peak energy and crystal waveform) for around 1400 crystals most of which are due to electronics noise and beam-induced background. To reduce noise crystals with energy deposits less than 20 MeV or lying outside the  $1.3 \mu s$  event time are rejected. The remaining crystals have their raw energies and times converted to physical units and are added to the L3EMC crystal list. Clusters are formed using a look-up table technique, and any clusters with energy above 100 MeV are retained. The clusters' energy weighted centroid and average time, the number of crystals, and a lateral moment describing the shower shape for particle identification are calculated.

Based on the track and cluster information a number of filters can perform event classification and background reduction. The logging decision is primarily made by two orthogonal filters: one based exclusively on DCH data and one exclusively on EMC data. The output of both these filters is dominated by Bhabha events. These events are rejected using a Bhabha veto filter that selects one-prong (only a positron in the backward part of the detector) and two-prong events (both electron and positron detected). Stringent criteria on EMC energy deposits are imposed relying on the track momenta and on E/p. The two-prong veto requires either collinearity in between the two tracks in the Center of Mass (CM) system or an collinearity consistent with initial state radiation (ISR).

## 6.8 Summary

The BaBar experiment, using beams in the PEP-II rings, consists of a Silicon Vertex Chamber, a Drift Chamber, an Electromagnetic Calorimeter, a Detector of Internally Reflected Cherenkov Light and a Instrumented Flux Return to detect muons. The data output is first of all analysed by the Level 1 and Level 3 trigger systems before the filtered data set is stored ready to be input to the reconstruction software. The BaBar software framework is described in the next chapter.

# Chapter 7

## The BaBar Software Framework

The BaBar software is almost entirely written in C++ (the exception being the physics generators which are written in FORTRAN by theorists who are not BaBar collaborators). C++ is an Object-Oriented (OO) language, and was selected on the basis of the cost of compilers, support for different platforms, available development and debugging tools and interfaces to databases. Today some would support Java as a strong contender to be the language used on BaBar. [27]

C++ typically consists of a series of classes each of which consists of functions to build and destroy a particular object and other functions, known as member functions, that may be accessed by that object. Groups of similar classes are grouped into packages, and in turn the packages are grouped into a particular release. The OO aspect of C++ encourages the dependencies between classes to be minimised thereby reducing the time it takes to build a release because much of the code need not be recompiled. On BaBar this is important because a nightly build is done each day and this would be too time consuming if all the code were to be recompiled.

The majority of the computing infrastructure uses the Linux Red Hat [28] operating system, although the Sun Solaris [29] system is also used. Both the Andrew File System (AFS) [30] and the Network File System (NFS) [31] are used. The AFS system allows users to edit files from a remote location, but the NFS system only allows local editing of files.

To add new code to the BaBar software the Concurrent Version System (CVS) [32] is used. The BaBar software framework is maintained at multiple Tier A sites: SLAC, Rutherford Appleton Laboratory (RAL), Institut National de Physique Nucleaire et de Physique des Particules (IN2P3) and Istituto Nazionale di Fisica Nucleare (INFN). Many universities also maintain copies of the Framework for local use.

## 7.1 Online Reconstruction Software

The OPR software uses the ELF [33] package to run reconstruction algorithms and persist the interesting events to the database. The Objectivity [34] database is used for this purpose. Currently Objectivity is being phased out in favour of the Kinder ANd Gentle Analysis (KANGA) [35] format which is used in the New Computing Model (CM2) [36]. The analysis described in this thesis only uses the data stored in the Objectivity database.

The database contains five levels: Raw, in which the raw digitisations (hits in the EMC for example) are stored; Reco, which contains , in addition processed Raw

data (reconstructed tracks etc); Mini, in which the data are stored more efficiently to reduce disk usage and access speed; Micro which is a subset of the Mini used in BaBar physics analyses and the Nano level which contains yes or no answers to complex algorithms run on the database enabling analysts to bypass running many of the algorithms required for a typical physics analysis. The analysis in this thesis used both the Micro and Nano database levels.

Groups of Nano level quantities are often used to form skimmed datasets which are selected common sets of events that different groups of analysts might be interested in. In the TauQED Analysis Working Group (AWG) the stream19 skim is often used. It was not used for the analysis described in this thesis, however, due to its hard cuts against interesting tau events. In CM2 the Mini is envisaged as being the level of choice for typical analyses.

## 7.2 Offline Analysis Software

The Framework [37] allows physicists to deploy code and combine it with code developed by others. The Framework employs a top down approach to software engineering whereby the overall structure is more important than low level details. In the offline software BaBar code is built from modules (C++ classes) which take an event from the database, run an algorithm on it and put the results back into the event. Users typically base their code on the BetaUser package, and the analysis in this thesis used such a package called TauNtuple [38], which uses both standard modules and modules written specifically for tau analyses.

The modules are grouped into sequences which are run when events from the database are analysed. The Tool Command Language (Tcl) [39] is used to control the sequences used in a particular analysis as well as set various other flags such as that controlling the output format of the selected events in the analysis.

### 7.3 Simulation Software

The simulation consists of physics generators and the detector level simulation. BaBar uses a number of physics generators - the main ones being EvtGen [40] for  $B\bar{B}$  events and continuum events (via JetSet [41]), GamGam for two photon events and  $kk2f$  [42] (described in detail in the next chapter) for both tau and mu pair production. These generate the physics of the Standard Model interactions.

The output of the generators is passed to the detector level simulation [43]. This is based on the GEANT4 [44] toolkit and is part of the Monolithic Object-Oriented Simulation Executable (MOOSE). MOOSE performs several tasks. First the four-vectors, representing the particles, from the generators are tracked through the detector by the BaBar Object-Oriented Geant4 based Unified Simulation (BOGUS) during which energy loss, production of secondaries, multiple scattering and decay can occur. Energy, charge and angular information is used to calculate simulated energy deposits, known as GHits, in the sensitive parts of the detector. The GHits are persisted into the database for later use, allowing the GHits to be digitised by SimApp so as to represent realistic signals that are a simulation of the output from the real detectors electronics. Finally the BEAR application performs the reconstruction, in the same way as ELF does for real data, to make the final events

stored in the database.

## 7.4 Summary

The BaBar software, mostly written in Object-Oriented `c++`, consists of Reconstruction software to analyse the data and Simulation software to simulate the data set. The Simulation is made up of event generators to create the 4-vectors of the particles which are passed to the full GEANT4 based simulation. Finally the output is digitised and passed to BEAR which reconstructs the simulated data. The next chapter will describe in detail the event generator software used to generate tau events.

# Chapter 8

## The kk2f Generator

The kk2f [42](also known as KKMC) generator has replaced the KORALB [45] generator in BaBar. This was done because kk2f calculates QED up to higher orders in  $\alpha$  and uses the Coherent Exclusive Exponentiation (CEEX) [46] [47] instead of Exclusive Exponentiation (EEX) [47] (which is retained as a back up test). The difference is that CEEX calculates spin amplitudes explicitly and EEX simply sums and averages them. Therefore in the EEX scheme interference between ISR and FSR had to be neglected.

In addition kk2f has moved toward a FORTRAN Object-Oriented structure, allowing modules to be more easily replaced than in KORALB. Eventually kk2f will be migrated to a full Object-Oriented implementation in C++. KORALB and kk2f are compared in Table 8.1 [42]. The kk2f generator simulates the beam collisions and fermion production (e.g.,  $e^+e^- \rightarrow \tau^+\tau^-$ ), TAUOLA [49] the tau decays, PHOTOS [49] the radiation and Pythia [50] any non-tau hadronic decays. All of these generators are contained in the KKMC package [51]. Subsequently in BaBar these

Feature	KORALB	KK 4.13
QED Type	$O(\alpha)$	CEEX,EEX
CEEX (ISR and FSR)	none	$\alpha, \alpha L, \alpha^2 L^2, \alpha^2 L$
EEX (ISR and FSR)	none	$\alpha, \alpha L, \alpha^2 L^2, \alpha^3 L^3$
ISR-FSR Interference	$O(\alpha)$	$\alpha, \alpha L_{CEEX}$
Exact Bremsstrahlung	1 $\gamma$	1,2,3 Collinear $\gamma$
Electroweak	No Z Bosons	Dizet 6 [48]
Tau Decay	TAUOLA	TAUOLA

Table 8.1: Comparison of KORALB and KK 4.13

have been made into standalone packages because both KORALB and kk2f use TAUOLA; in addition PHOTOS is used by KORALB, kk2f and EvtGen. Eventually Pythia may be used by EvtGen as well as kk2f.

Initially kk2f 4.14 was installed for potential usage in the simulation of muon pair production. Currently kk2f 4.19 is being used for production because it includes modifications to the  $\rho$  resonances form factors (used in  $q\bar{q}$  production and decay) that were required by the Inclusive Hadronic AWG. It was verified that the change in the  $\rho$  form factor does not affect tau decays by comparing the  $\rho$  (from a1 decays) mass distribution in kk 4.16 and kk 4.19 shown in Figure 8.1. In addition a standard set of plots were checked using the GqaTauHisto<sup>1</sup> analysis module which is always done whenever a change is made to kk2f.

To validate changes between KORALB and kk2f a series of energy weighted plots (because kk2f generates more photons due to higher order calculations in the QED matrix elements) of quantities related to photon radiation were made and they show good agreement.

---

<sup>1</sup>A quality control module written by the author with contributions from Dr O.Igonkina (olya@slac.stanford.edu) and Dr S.Banerjee (swaban@slac.stanford.edu). The module is part of the GeneratorsQA package and may be checked out from the BaBar CVS repository

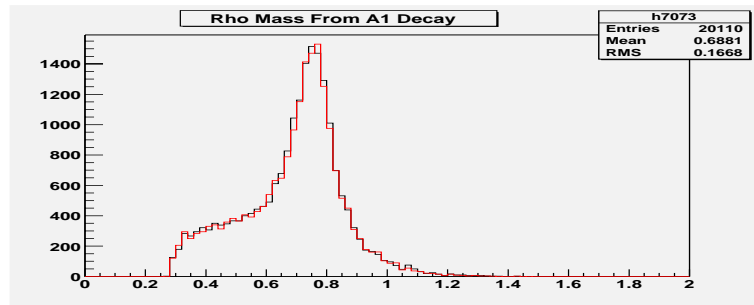
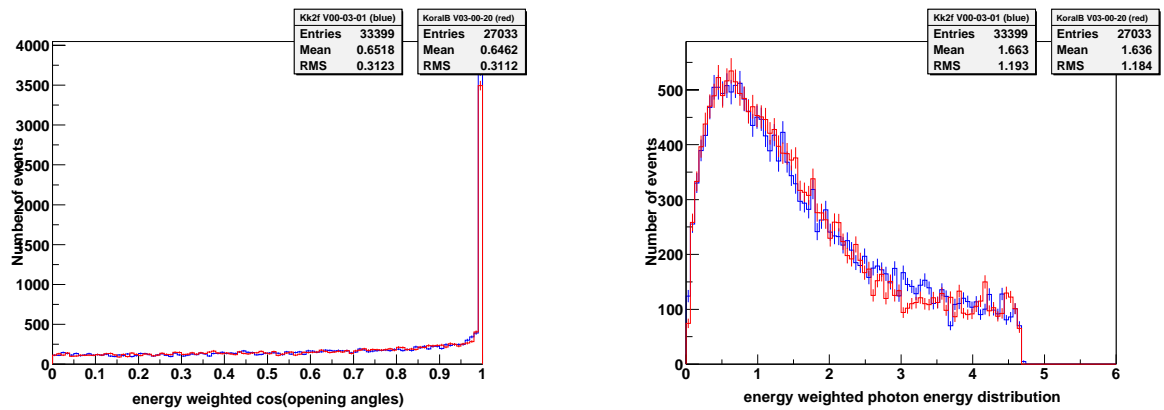


Figure 8.1: Rho Resonance from a1 Decay



(a) Cos(Opening Angle)

(b) Energy

Figure 8.2: Cosine of Opening Angle and Energy distributions weighted by Energy for Photons in KORALB(Red) and kk2f(Blue)

Several versions of TAUOLA are available each containing different parameterisations of the tau decay modes. Initial comparisons of KORALB using the kk2f default TAUOLA, kk2f using the kk2f default TAUOLA and kk2f using the CLEO TAUOLA were made. Figure 8.4 clearly shows the  $\pi^+\pi^-\pi^+$  mass, dominated by the a1 resonance, is shifted between the three scenarios. This reflects the poor understanding of the a1 mass. The shift between KORALB and kk2f occurs because the a1 mass is an input parameter to TAUOLA and KORALB and kk2f do not input the same value. The  $\pi^+\pi^-\pi^0$  distribution shows an excess of the  $\omega$  resonance in the CLEO TAUOLA.

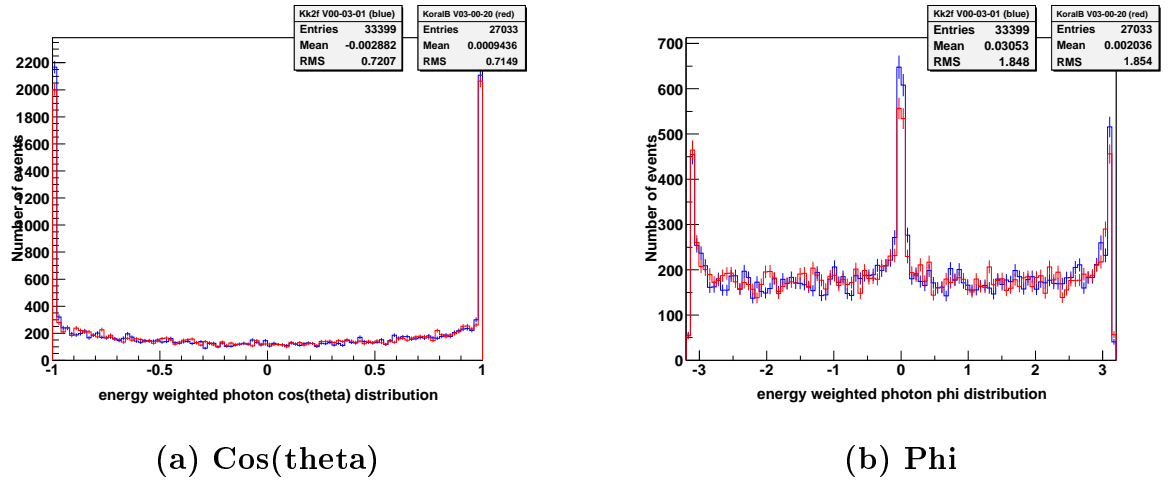


Figure 8.3: Cosine of Theta and Phi distributions weighted by Energy for Photons in KORALB(Red) and kk2f(Blue)

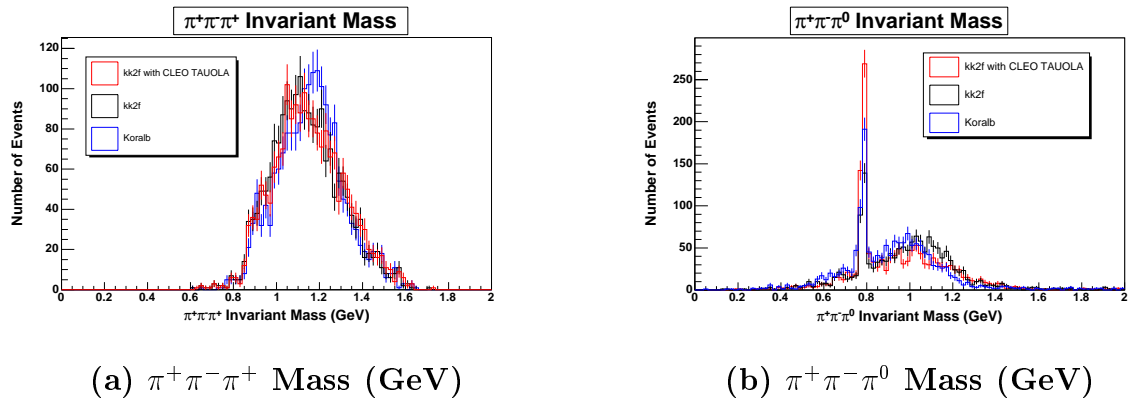


Figure 8.4: Comparison of Mass Plots for kk2f and KORALB using the default kk2f TAUOLA and kk2f using the CLEO TAUOLA

The default kk2f TAUOLA is the one that was chosen for production and these (and other) mass distributions will be tuned using the BaBar data set instead of trying to use another experiment's, such as CLEO's, parameterisation. Currently the  $\pi^+\pi^-\pi^0$  [52] mass spectrum is being studied at BaBar, and significant discrepancies in the simulation of 5-pronged tau decays have been found [53, 54]. Excess in the data of the  $K_S^0\pi$  mass spectrum have been observed at around 1400 MeV that are possibly due to decays into higher mass  $K^*$  resonances, which are not modeled in TAUOLA. This is to be expected - any differences improve our knowledge of physics.

In BaBar sequential MC production runs are undertaken which are labeled as SPx where x is an integer. A typical run lasts one year and no major changes may be made to the simulation during this time. The kk2f generator was installed into the BaBar framework in time for the SP5 run. The tau branching fractions were updated to reflect the PDG 2002 values. Using a unitarity constraint the branching fractions were recalculated [55] and rounded to 3 decimal places, and they are shown in Table 8. The rounding to 3 decimal places was due to unforeseen technical reasons, and has been corrected in SP6 [56].

A number of exotic modes were added to the TAUOLA package by Dr S.Banerjee. These include CP violating  $K^*$  decays, CP violating  $\rho$  decays and a large contingent of lepton flavour violating modes.

Br( $\times 10^{-2}$ )	Decay Mode
17.865	$e^-$
17.355	$\mu^-$
11.084	$\pi^-$
25.375	$\pi^- \pi^0$
18.357	$a1^-$
0.695	$K^-$
0.364	$K^{*-}$
4.365	$\pi^- \pi^- \pi^0 \pi^+$
1.262	$\pi^0 \pi^0 \pi^0 \pi^-$
0.501	$\pi^- \pi^- \pi^+ \pi^0 \pi^0$
0.079	$\pi^- \pi^- \pi^- \pi^+ \pi^+$
0.018	$\pi^- \pi^- \pi^- \pi^+ \pi^+ \pi^0$
0.025	$\pi^- \pi^- \pi^+ \pi^0 \pi^0 \pi^0$
0.159	$K^- \pi^- K^+$
0.167	$K^0 \pi^- K^0$
0.154	$K^- K^0 \pi^0$
0.068	$\pi^0 \pi^0 K^-$
0.301	$K^- \pi^- \pi^+$
0.377	$\pi^- K^0 \pi^0$
0.183	$\eta^0 \pi^- \pi^0$
0.080	$\pi^- \pi^0 \gamma$
0.165	$K^- K^0$

Table 8.2: Branching Fractions used in kk2f in SP5 [1]

## 8.1 Summary

The KORALB generator has been replaced by the kk2f generator which calculates matrix elements to higher orders in  $\alpha$ . The TAUOLA package has been modified to include many exotic decay modes including CP violating modes which are used for the data analysis described in this thesis. The next chapter describes the method of selecting events for the data analysis.

# Chapter 9

## Event Selection

The events are preselected using the TauNtuple package [57]. The cuts, which are used to select a general set of events of use in many tau analyses, may be divided into nano level and micro level cuts. The nano level cuts are as follows:

- The event is required to pass the L3EMC or L3DCH software trigger. These were defined at the end of Chapter 6.
- The event is required to pass at least one of five tagbits known as: BGFMultiHadron; BGFNeutralHadron; BGFTau; BGFMuMu and BGFTwoProng [58]. These are defined in Appendix B.
- The number of tracks must be less than or equal to 10 in order to suppress high multiplicity backgrounds, whilst keeping higher multiplicity tau decays (e.g. decays to seven pions).
- If there are more than two charged tracks in the event, R2 must be greater than 0.2. R2 is the ratio of the second Fox-Wolfram moment to the first

Fox-Wolfram moment and the  $l^{\text{th}}$  order moment is given by

$$H_l = \sum_{a,b} \frac{|\vec{p}_a||\vec{p}_b|}{s} P_l(\cos \theta_{ab}) \quad (9.1)$$

where the sum is over all final state particles,  $\vec{p}_a$  and  $\vec{p}_b$  are the momenta of final state particles,  $\theta_{ab}$  is the angle between them,  $s$  is the square of the center of mass energy and  $P_l$  are the Legendre polynomials. R2 is an event shape variable that can distinguish between tau events and  $q\bar{q}$  backgrounds. The cut is only applied to events with more than two events because low multiplicity events have large values of R2.

- Less than thirteen neutral candidates with energy above 100 MeV.
- The sum of the charged cluster energy (in the laboratory frame) and momentum magnitude divided by the beam momenta (in the laboratory frame) should be less than 0.85 in order to suppress Bhabha events.
- If one of the two highest momentum tracks in the event has no calorimetric energy associated to it and is very forward or backward, and the other track of the two is consistent with being an electron then the event is discarded. A track is considered to be consistent with being an electron if the track momentum divided by the associated calorimetric energy (both in the c.m. frame) is greater than 0.8. A track is considered highly forward or backward if the cosine of the track angle is greater than 0.91 which corresponds to being inside the calorimeter acceptance. This cut also helps to reject Bhabha events.
- If both the highest momentum tracks are consistent with the electron criteria defined in the previous cut then to further suppress Bhabha backgrounds the summed momenta magnitudes of the two highest momenta tracks must be

greater than 5.5 GeV or the following inequality must be satisfied:

$$\frac{thrustCosThAll}{0.9} + \frac{P1Mag - P2Mag}{\sqrt{s}} > 1 \quad (9.2)$$

where *thrustCosThAll* is the cosine of the theta component of the thrust axis (defined in terms of neutral and charged candidates). *P1Mag* and *P2Mag* are the momentum of the two highest momentum tracks in the event.

- Finally the missing mass (defined to be the invariant mass of the 4-vector representing the difference between the measured 4-vectors of particles and the null 4-vector) in the event divided by  $\sqrt{s}$  must be less than 0.2 or  $-\log(2Pt/\sqrt{s})$  must be less than 4 in order to suppress two-photon backgrounds.

At the micro level the following cuts must be passed:

- Number of charged tracks is less than or equal to 10. Tracks are defined with tighter criteria than at the nano level and so the cut on numbers of micro tracks is also set to ten.
- Using the thrust axis (defined in terms of charged tracks and neutrals with at least 50 MeV energy) to divide the event in the c.m frame into two hemispheres, no more than 6 neutrals with at least 50 MeV energy are allowed in each hemisphere.
- At least two GoodTracksVeryLoose (GTVL) and no more than 3 GTVL tracks in one hemisphere OR if one hemisphere has more than 3 GTVL tracks then the opposite hemisphere must have exactly one GTVL track. This helps to ensure tracks originate close to the primary interaction point in the event.

GoodTracksVeryLoose is defined as a track with a maximum momentum of 10 GeV, Distance of Closest Approach (DOCA) in  $z$  less than 10 cm and in the  $xy$  plane less than 1.5 cm

## 9.1 Event Selection

The ntuples made with TauNtuple are general purpose ntuples used in many analyses within the TauQED AWG. Once the ntuples are made, the procedure is to extract the signal events out of them using the ROOT [59] analysis package in conjunction with the TauCPAnalysis package.<sup>1</sup>

### 9.1.1 Signal Event Selection

First the event is divided into two hemispheres using the thrust (calculated using candidates both charged, from the ChargedTracks list, and neutral, from the CalorNeutral list with more than 50 MeV energy) axis of the event. It is required that in one hemisphere a tau decays to  $K^*$  followed by  $K^* \rightarrow K_S^0 \pi^-$  and  $K_S^0 \rightarrow \pi^+ \pi^-$  (here and throughout this thesis the charge conjugate is always implied). This is referred to as the signal hemisphere. The signal event contains the signal hemisphere and the tag hemisphere. An excellent way to reduce the non-tau backgrounds is to require the other tau to decay leptonically. Thus the tag hemisphere is required to contain a leptonic tau decay, illustrated in Figure 9.1. In the following analysis the lepton is referred to as the electron, because the analysis currently consists of only

---

<sup>1</sup>An analysis package, based on TauAnalysis written by the Author and Dr Andrew Lyon, is available on request from the author.

an electron tagged sample.

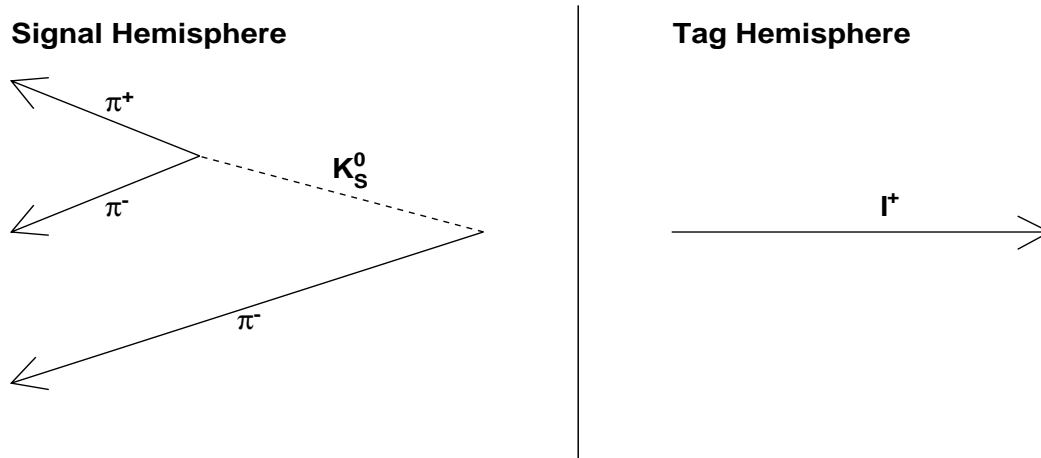


Figure 9.1: Event Hemispheres

### Initial Event Selection

Well reconstructed signal events are required to have exactly 4 charged tracks in them consisting of 1 charged track from the leptonic tau decay and 3 charged tracks from the signal decay. This is a good rejection of non-tau hadronic backgrounds, because these types of events tend to have higher multiplicities. Conversely Bhabha events are dominated by events involving 2 charged tracks.

Further requirements are:

- that the sum of the charges of the four tracks is zero.

- a  $K_S^0$  topology. This means that of the four tracks present one is contained in a separate hemisphere to the other three tracks. This track, known as the tag track, is required to pass the GoodTracksVeryLoose criteria. At this point no track quality criteria are imposed on the remaining three tracks.
- the tag track may not be the daughter of the selected  $K_S^0$  candidate. This is important because the tag track must be an electron to be effective in reducing hadronic backgrounds, but if the tag track is a daughter of a  $K_S^0$  then the tag track is a pion regardless of whether it passed an electron selection algorithm.
- the tag track is required to pass the electron LikelihoodTight [60] selector.

### $\pi^0$ and $K_L^0$ Suppression

The next requirement is a restriction on neutral energy in the signal hemisphere of the event. This is necessary because the largest tau background is  $\tau^\pm \rightarrow \pi^\pm \pi^\pm \pi^\pm \pi^0$ . A neutral is defined by the CalorNeutral list. The 3-vector of the neutral is added to a sum if it has energy greater than 50 MeV, is more than 40 cm from a charged track and is present in the signal hemisphere. The 40 cm cut is included to avoid inducing a fake CP asymmetry in the signal sample, discussed in the Detector Asymmetries section later in this chapter. Any event with less than 1 GeV of energy in this sum, shown for data and MC in Figure 9.2, is retained. This is a loose cut, but the Monte Carlo does not model the data at all well below 0.8 GeV and it is therefore too dangerous to place a tighter cut in this region below 1 GeV. The remaining backgrounds that contain  $\pi^0$ s are left to be subtracted off, based on estimates from the Monte Carlo, after all cuts are applied. An additional background is that of  $\tau \rightarrow K_S^0 \pi^\pm K_L^0$ . It is not possible to cut against this whilst increasing the significance,

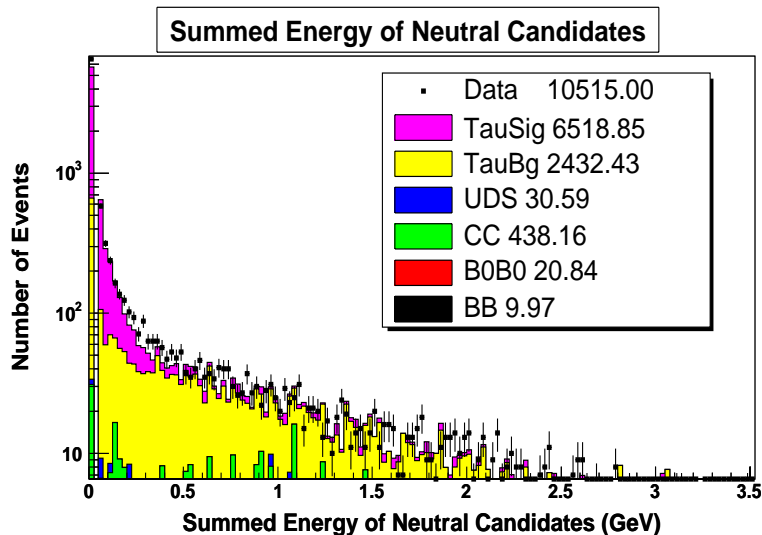
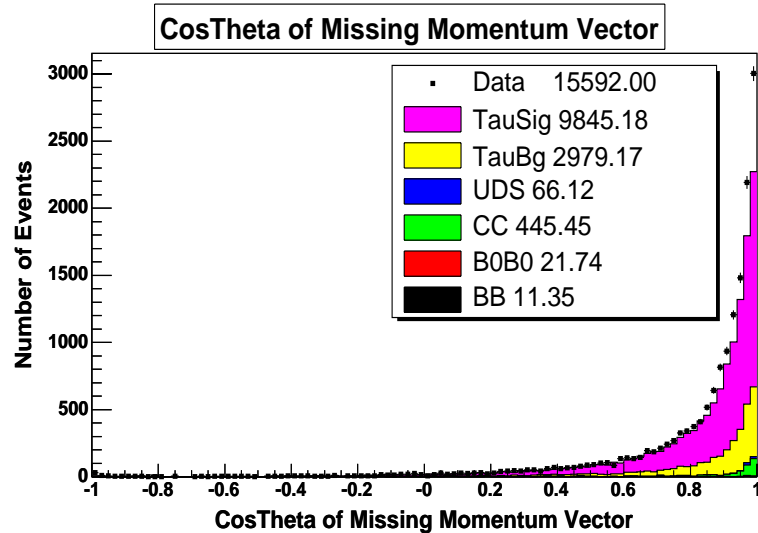


Figure 9.2: Neutral Energy with all other cuts applied.

efficiency and purity of this signal sample unless a very tight neutral energy cut is first applied. Therefore this background is not cut against and is left to be subtracted.

### Suppression of Radiative Events

If one of the beam particles radiates and the photon goes down the beam-pipe the missing momentum vector will be have a  $|\cos\theta|$  close to 1. These events are poorly modeled in the MC and a clear excess of data is seen at large  $\cos\theta_{Miss}$  (shown in Figure 9.3 ). Therefore  $\cos\theta_{Miss}$  is required to be in the range  $-0.76$  to  $0.95$ , roughly corresponding to the EMC acceptance, in order to reject this class of events.

Figure 9.3:  $\cos\theta_{Miss}$ 

### Suppression of Bhabha Events

In order to suppress Bhabha events, a further cut on the one prong momentum (in the c.m frame) is included. If a positron-electron pair is produced from the initial beam collision and a radiated photon converts a total of 4 leptons are present, which can fake a signal event. In this case the one-prong electron will have high momentum; a small excess of data is seen at high momentum in Figure 9.4.

### Suppression of $K_S^0 K^\pm$ events

The next  $\tau$  background to be cut is the mode  $\tau \rightarrow K^0 K^\pm$ . This is easily removed from the signal sample by requiring the track that is not from the  $K_S^0$  candidate and that is not the tag track should pass the pion LikeliHoodTight selector [61].

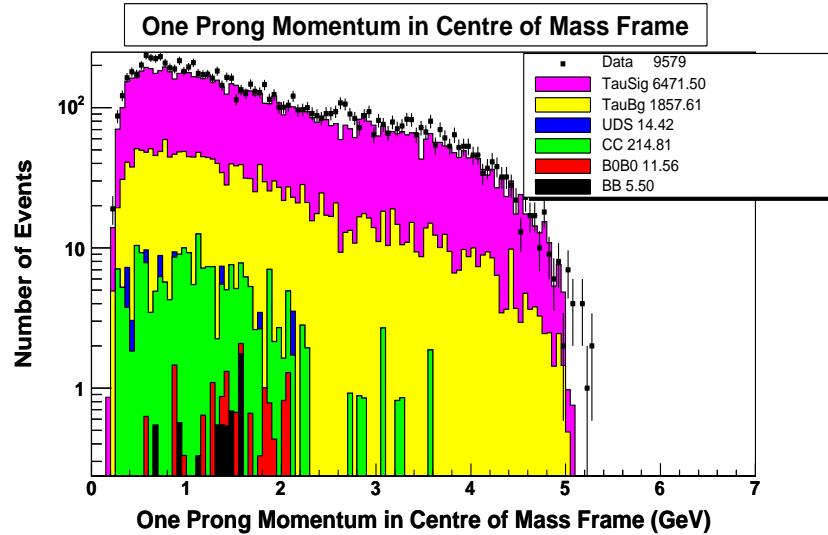


Figure 9.4: One Prong Momentum Spectrum

### Detector Asymmetries

Differences in performance of the detector with respect to  $\tau^+$  and  $\tau^-$  decays will contribute to any measured CP asymmetry. There are several asymmetries comprising asymmetries due to track reconstruction algorithms and due to calorimetric effects.

The calorimetric asymmetry can occur due to interactions between charged pions and protons in the Caesium Iodide crystals of the Electromagnetic Calorimeter. This is because the cross-sections for  $\pi^+p$  and  $\pi^-p$  interactions are not the same. These cross-sections are plotted in Figure 9.5. At low momentum the cross-sections differ significantly. This is expected to manifest itself in the number of photons seen in the vicinity of  $\pi^+$  and  $\pi^-$  tracks and so the neutrals asymmetry is considered

$$A_{neutrals} = \frac{N(d)^+ - N(d)^-}{N(d)^+ + N(d)^-} \quad (9.3)$$

where  $N(d)^\pm$  is the number of neutral candidates, defined to be in the CalorNeutral list and have at least 50 MeV energy (low energy candidates can be due to noise), at a distance  $d$  from a track with charge  $\pm 1$ . The calculation of the distance relies on knowledge of the theta and phi of an extrapolated track intersecting the front-face of the EMC. The theta and phi are calculated assuming tracks originated at the beamspot, so the asymmetry must be considered separately for daughter tracks of a  $K_S^0$  candidate, to those that really did originate at the beamspot. The distance threshold is chosen such that the measured asymmetry in the asymmetry plot above the threshold is reasonable without cutting too many events from the selected sample.

Figures 9.6, 9.7 and 9.8 show the data and MC distributions for the distance from a track to the nearest neutral for the three tracks on the signal side of the event. Events containing tracks within 40 cm of a neutral the MC simulation does not model the data particularly well and so a threshold of 40 cm is used (with a better MC simulation this could be lowered). Figure 9.9 shows the asymmetry for the bachelor track in data and Figure 9.10 shows the distribution of the distance from neutral to nearest track for positively and negatively charged tracks (in data) overlaid. The next two figures show the same plots for the tracks coming from the decay of the  $K_S^0$  candidate.

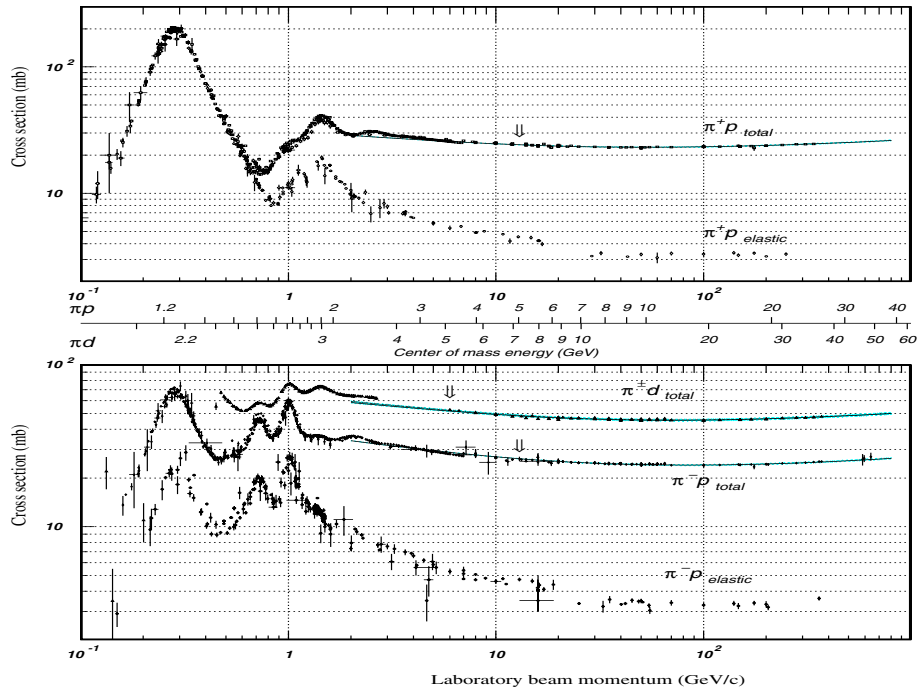
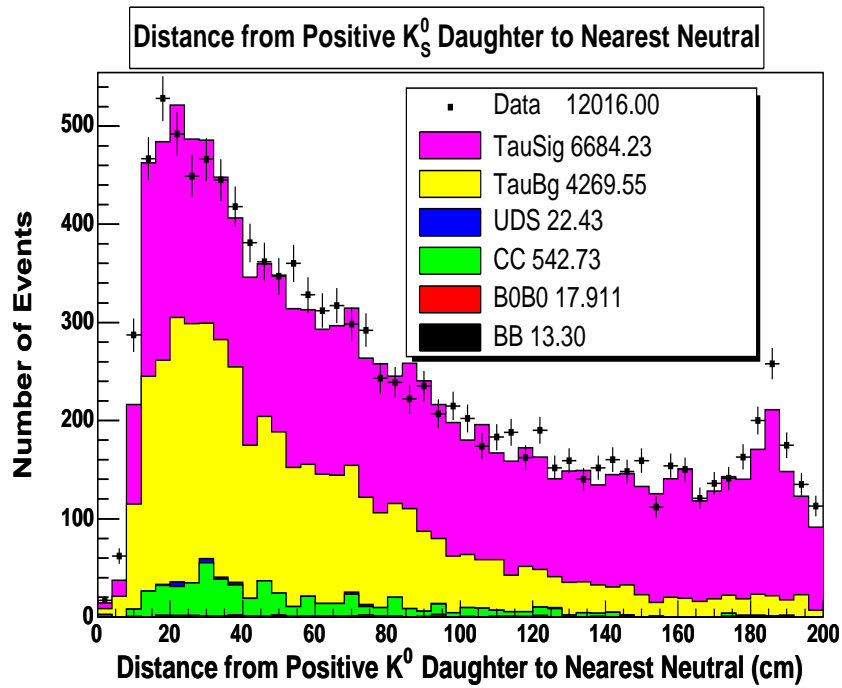


Figure 9.5: Cross-sections for Pion-Proton Interactions [1]

Figure 9.6: Distance from Positive  $K_S^0$  Daughter to Nearest Neutral

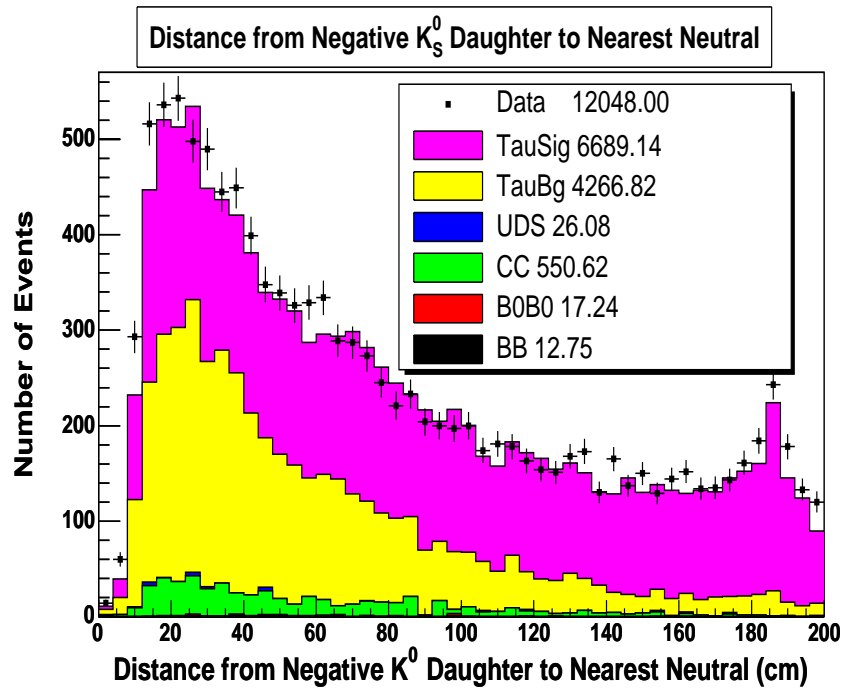
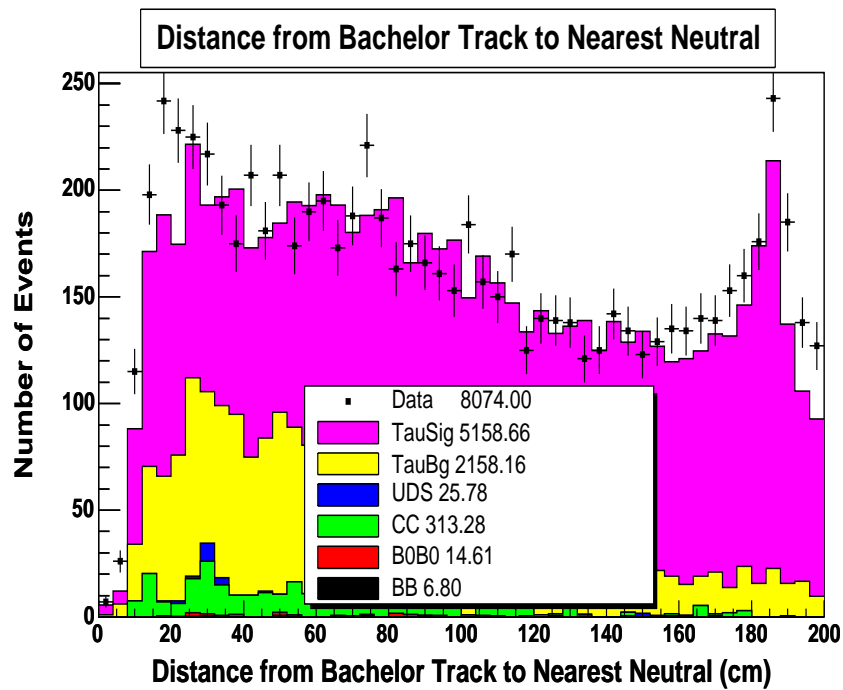
Figure 9.7: Distance from Negative  $K_s^0$  Daughter to Nearest Neutral

Figure 9.8: Distance from Bachelor Track to Nearest Neutral

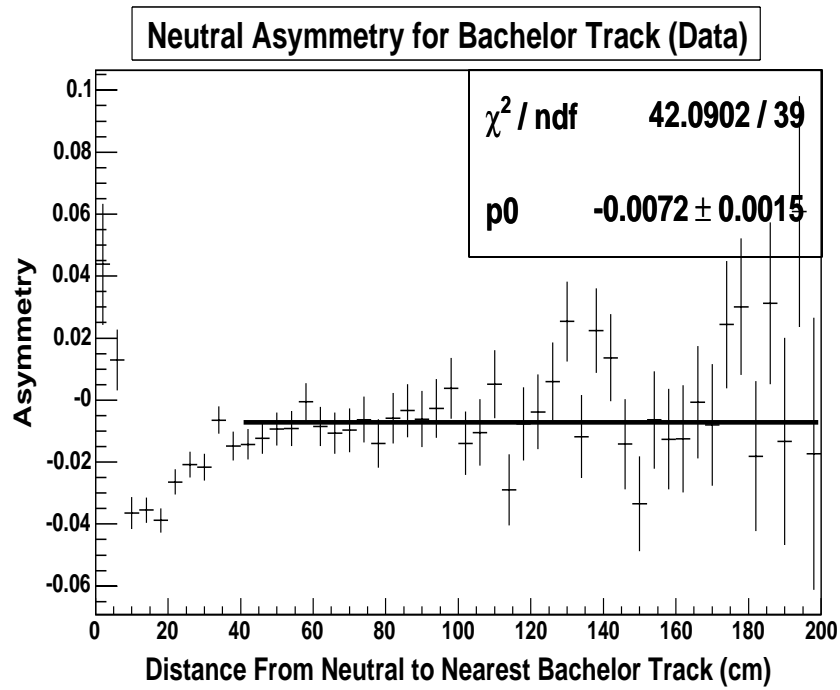


Figure 9.9: Neutral Asymmetry for Bachelor Track in Data

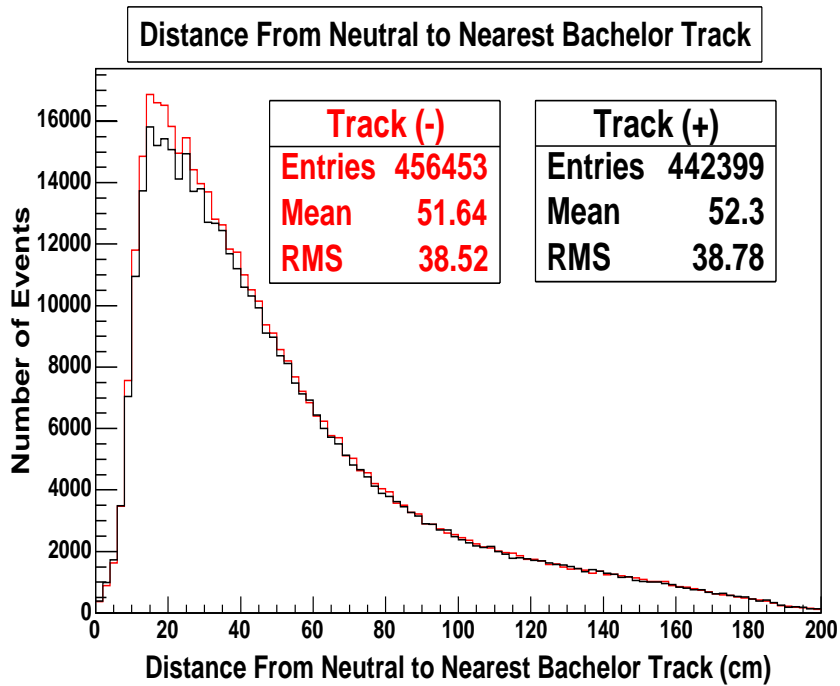
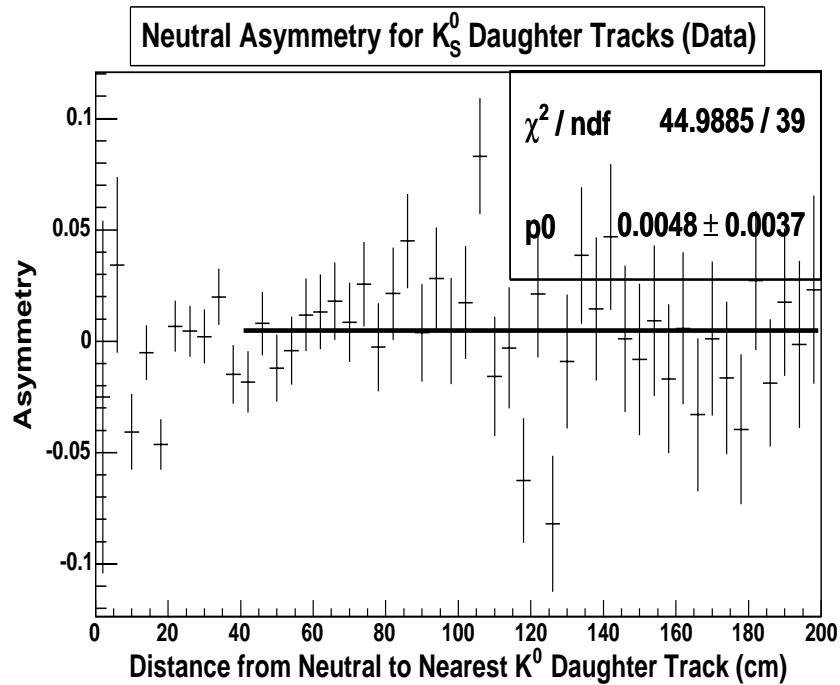
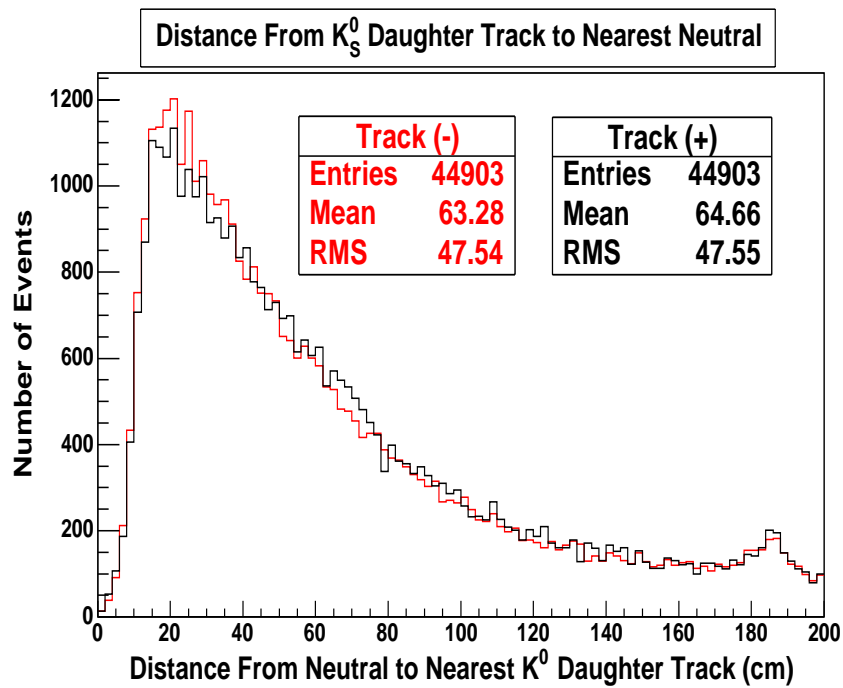
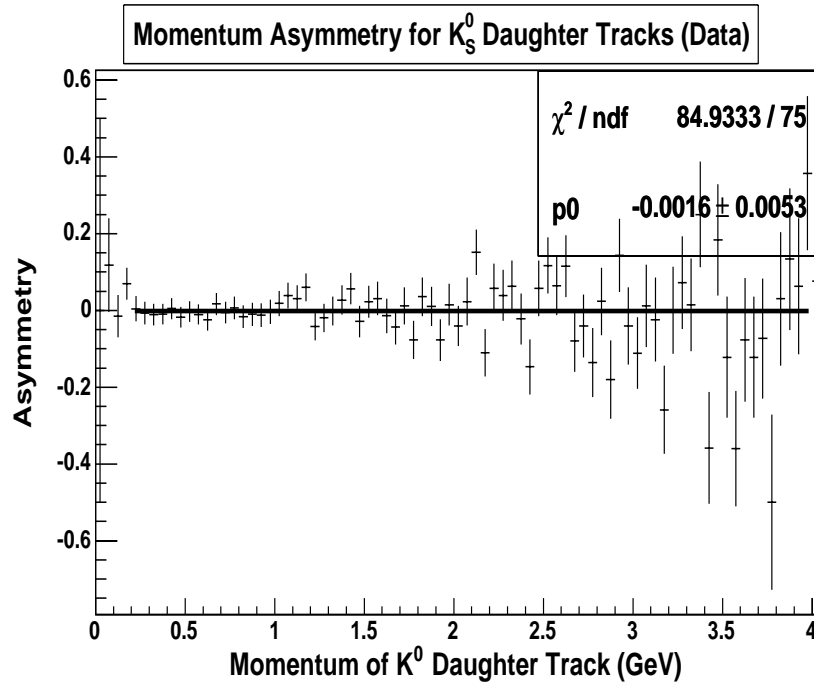
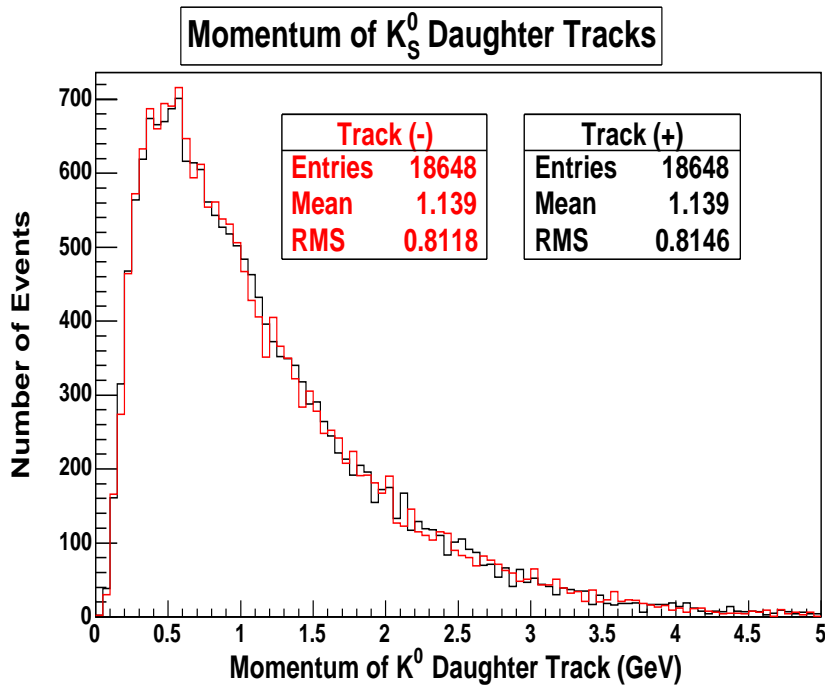


Figure 9.10: Neutral-Track Distance (cm) for Bachelor Track in Data

Figure 9.11: Neutral Asymmetry for  $K_S^0$  Daughter Tracks in DataFigure 9.12: Neutral-Track Distance (cm) for  $K_S^0$  Daughter Tracks in Data

Figure 9.13: Tracking Asymmetry for Fitted  $K_S^0$  Daughter Tracks in DataFigure 9.14: Momentum (GeV) for Fitted  $K_S^0$  Daughter Tracks in Data

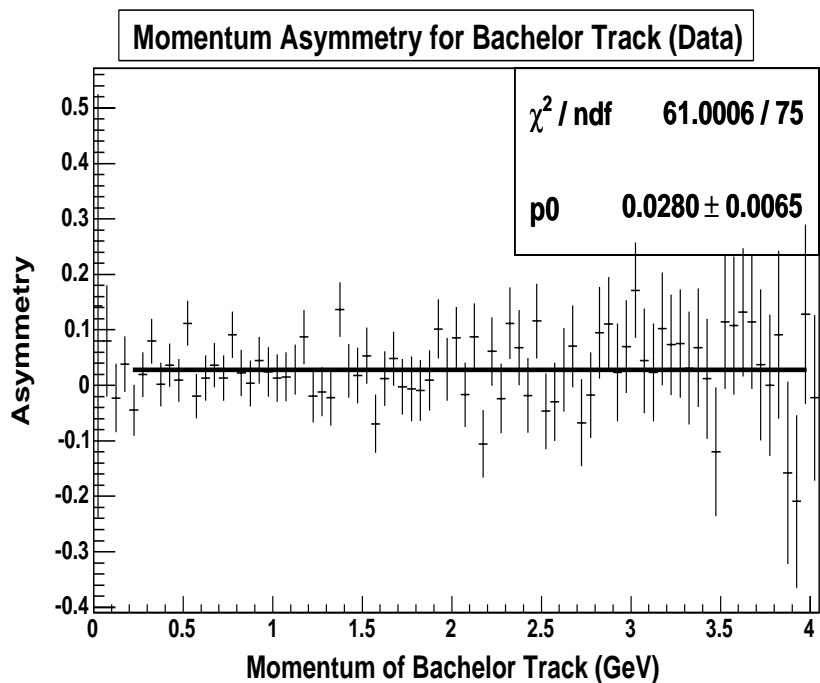


Figure 9.15: Tracking Asymmetry for Bachelor Track in Data

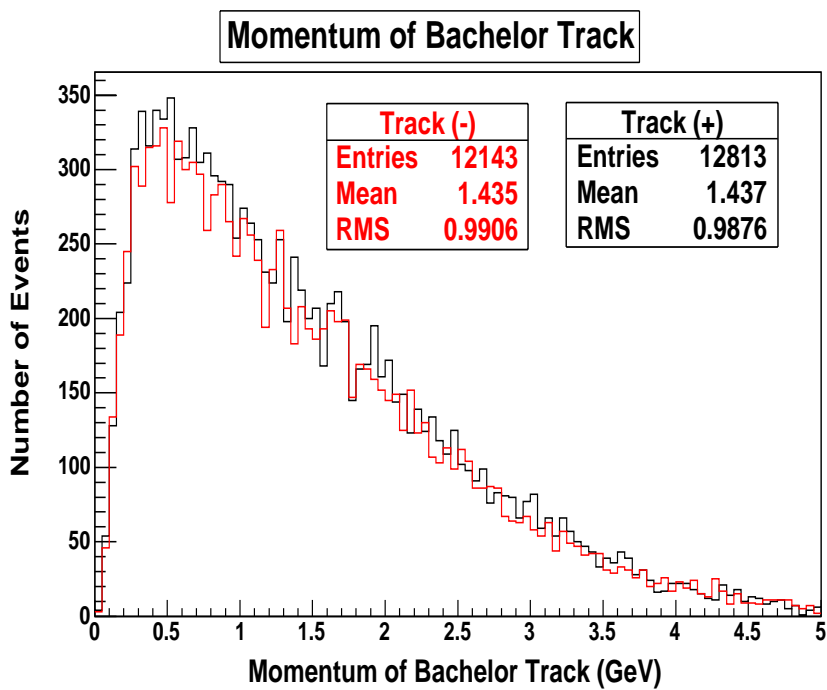


Figure 9.16: Momentum (GeV) for Bachelor Track in Data

The second possible asymmetry, due to differences in tracking efficiency, has been studied using both the charged pions from the  $K_S^0$  decay and the bachelor pion. This is

$$A_{charged} = \frac{N(p)^+ - N(p)^-}{N(p)^+ + N(p)^-} \quad (9.4)$$

where  $N(p)^\pm$  is the number of pions with laboratory momentum  $p$  and charge  $\pm 1$ .

To study this, first each track is required to be at least 40 cm from a neutral candidate. The momentum dependent asymmetry for the vertex-fitted  $K_S^0$  daughter tracks is shown in Figure 9.13 and a threshold of 0.2 GeV is applied to these tracks. The momentum distribution for positively and negatively charged  $K_S^0$  daughter tracks is shown in Figure 9.14. Figure 9.15 shows this asymmetry for the bachelor track and a 0.2 GeV threshold is also applied to this track. Figure 9.16 shows the momentum distribution for positively and negatively charged bachelor tracks overlaid.

### $K_S^0$ Candidate Selection

The previous cuts described are known as the event selection cuts. The subsequent cuts are known as the  $K_S^0$  selection cuts. To define a  $K_S^0$  the KsDefault candidate list is used. This is defined in the following way:

1. Find all oppositely charged track pairs with  $> 12$  DCH hits
2. Restrict the invariant mass to be in the range 0.3 to 0.7 GeV
3. Perform a vertex-constrained fit using the GeoKin fitter [62].
4. Restrict the fitted candidates mass to within 25 MeV of the PDG mass [1]

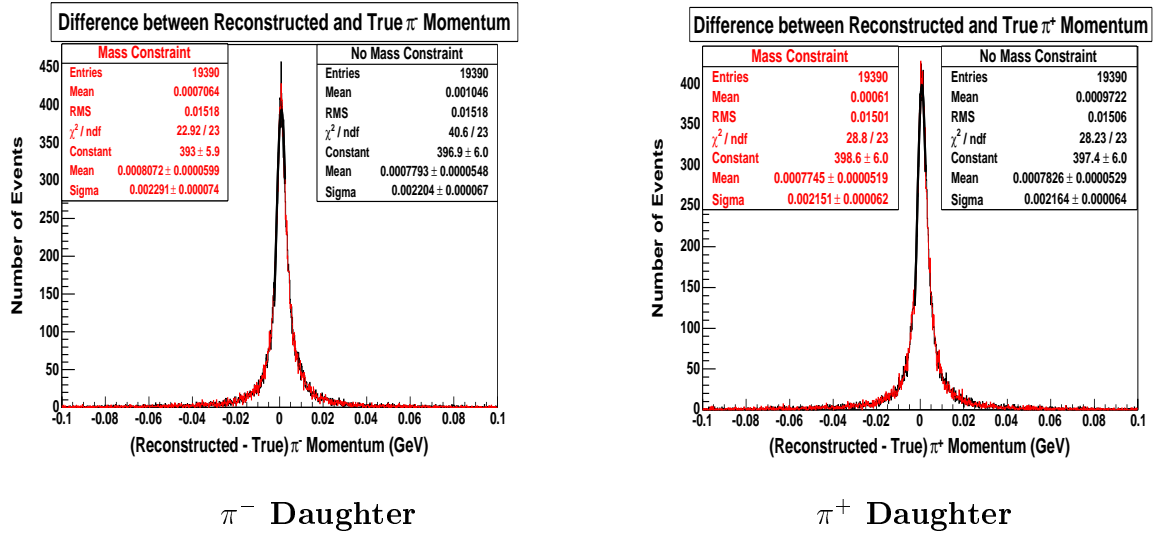


Figure 9.17: Fit of difference between the Reconstructed Momentum and the True Momentum for KsDefault (Red) and KsTight (Black) Candidates

There is a further option, namely to perform a mass-constrained fit on the KsDefault candidate; this produces the KsTight candidate list. Figure 9.17 shows the bias of the  $K_S^0$  candidates daughter momentum between reconstructed candidates in the tau MC and  $K_S^0$  truth candidates in the tau MC. The parameters of the fit are shown in Table 9.1. The negative and positive daughters are treated separately. There is little difference in the bias for KsDefault and KsTight candidates. Thus the KsDefault list is used.

Quantity	Vertex-Constrained Fit	Vertex And Mass-Constrained Fit
Mean ( $\pi^+$ )	$(7.79 \pm 0.55) \times 10^{-4}$ (GeV)	$(8.07 \pm 0.60) \times 10^{-4}$ (GeV)
Width ( $\pi^+$ )	$(22.04 \pm 0.67) \times 10^{-4}$ (GeV)	$(22.91 \pm 0.74) \times 10^{-4}$ (GeV)
Mean ( $\pi^-$ )	$(7.83 \pm 0.53) \times 10^{-4}$ (GeV)	$(7.75 \pm 0.52) \times 10^{-4}$ (GeV)
Width ( $\pi^-$ )	$(21.64 \pm 0.64) \times 10^{-4}$ (GeV)	$(21.51 \pm 0.62) \times 10^{-4}$ (GeV)

Table 9.1: Parameters of Fit to Momenta Spectra of Pions



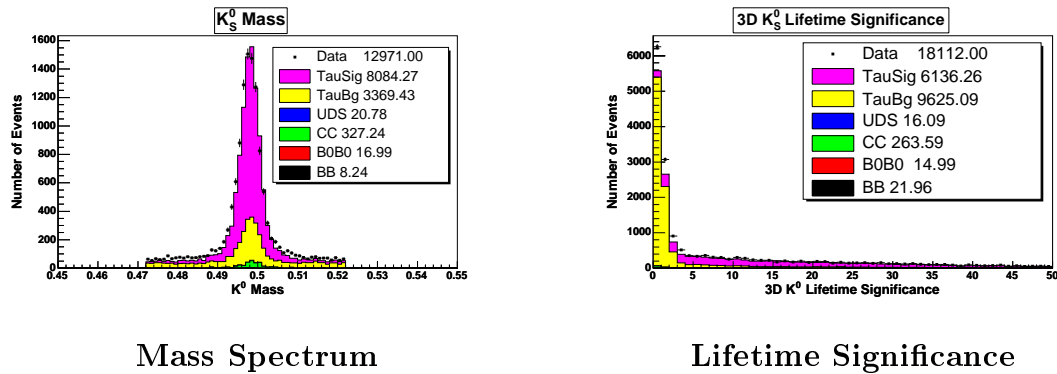


Figure 9.19: The  $K_S^0$  mass spectrum and lifetime significance with all cuts applied except the quantity plotted

## 9.2 Cut Summary

The cuts used are summarised as follows:

1. Nano and Micro level cuts.
2. Require exactly four charged tracks.
3. Require net charge of these four tracks to be zero.
4. Require the event to have a  $K_S^0$  Topology.
5. Require that the tag track is not the daughter of a  $K_S^0$  candidate.
6. Require the tag track to pass the electronLikeliHoodTight selector.
7. Require that there is less than 1 GeV of energy attributed to neutral particles, in the signal hemisphere, that have at least 50 MeV of energy and are more than 40 cm from a track.
8. Require the tag track to have less than 4.9 GeV momentum in the c.m. frame.

9. Require  $\cos \theta$  of the missing momentum vector to be between -0.75 and 0.95
10. Require the daughters of a  $K_S^0$  candidate to be more than 40 cm from a neutral candidate.
11. Require the track in the signal hemisphere that does not originate from the  $K_S^0$  decay to be more than 40 cm from a neutral candidate.
12. Require the daughters of a  $K_S^0$  candidate to have at least 0.2 GeV energy.
13. Require the track in the signal hemisphere that does not originate from the  $K_S^0$  decay to have at least 0.2 GeV energy.
14. Require the track in the signal hemisphere, that is not from the decay of a  $K_S^0$  candidate, to pass the pion LikeliHoodTight selector.
15. Require the track in the signal hemisphere, that is not from the decay of a  $K_S^0$  candidate, to pass the GTVL criteria.
16. Require both the tracks originating from the decay of the  $K_S^0$  candidate to have at least 12 DCH hits.
17. Require the  $K_S^0$  candidate to have a mass in the range 0.492 to 0.503 GeV.
18. Require the  $K_S^0$  candidate to have a 3D lifetime significance greater than 3.

The efficiencies of the selection criteria are shown in Table 9.2 and 9.3. After all cuts are applied the signal efficiency is 6.28% with a purity of 71.16% where the efficiency is given by

$$\epsilon = \frac{N_{Sig}^{Sel}}{N_{Sig}^{Gen}} \quad (9.6)$$

where  $N_{Sig}^{Sel}$  is the number of signal events selected in the MC and  $N_{Sig}^{Gen}$  is the number of signal events generated in the MC. The purity is

$$pur = \frac{N_{Sig}^{Sel}}{N_{MC}^{Sel}} \quad (9.7)$$

where  $N_{MC}^{Sel}$  is the number of MC events selected.

Cut	CumEff	MargEff	Pur	Sig	Eff(n-1)	Pur(n-1)	Sig(n-1)
1.	68.22	68.22	0.03	0.02	6.28	5.93	0.37
2.	44.34	65.00	0.11	0.05	6.28	71.16	4.47
3.	43.04	97.06	0.13	0.06	6.28	71.16	4.47
4.	36.51	84.83	0.20	0.07	6.28	71.16	4.47
5.	35.01	95.90	0.64	0.23	6.28	71.16	4.47
6.	31.03	88.65	5.16	1.60	6.28	71.16	4.47
7.	30.78	99.18	6.09	1.87	6.36	62.85	4.00
8.	30.75	99.90	6.09	1.87	6.29	71.17	4.48
9.	17.27	56.15	5.59	0.97	11.52	69.77	8.03
10.	10.85	62.84	11.54	1.25	8.27	62.53	5.17
11.	9.22	84.95	11.56	1.06	6.41	70.67	4.53
12.	8.18	88.76	12.75	1.04	7.02	69.16	4.86
13.	8.04	98.27	12.82	1.03	6.39	71.18	4.54
14.	7.87	97.91	14.26	1.12	6.41	58.98	3.78
15.	7.79	98.92	14.40	1.12	6.31	70.72	4.46
16.	7.73	99.32	14.44	1.12	6.29	71.01	4.47
17.	7.01	90.58	34.60	2.42	6.96	71.01	4.94
18.	6.28	89.68	71.16	4.47	6.93	64.18	4.45

Table 9.2: Efficiencies (%), Purities (%) and Significance of Selection Criteria  
**CumEff** Cumulative Efficiency; **MargEff** cut(n)/cut(n-1); **Eff(n-1)** Efficiency of all cuts except cut n; **Pur** Purity; **Sig** Significance (Efficiency\*Purity); **Pur(n-1)** Purity of n-1 cuts **Sig(n-1)** Significance of n-1 cuts

Cut	S17	T	Data	uds	b0b0	bb	cc
1.	68.21	64.89	23.65	26.87	3.40	3.67	16.40
2.	44.34	14.83	3.22	4.67	0.28	0.29	1.89
3.	43.04	13.84	2.32	3.87	0.20	0.21	1.43
4.	36.51	11.22	1.22	1.59	0.08	0.09	0.60
5.	35.01	3.26	0.36	0.47	0.02	0.02	0.20
6.	31.03	0.59	0.04	$1.40 \times 10^{-3}$	$4.31 \times 10^{-3}$	$3.80 \times 10^{-3}$	0.02
7.	30.78	0.50	0.04	$0.81 \times 10^{-3}$	$2.41 \times 10^{-3}$	$1.99 \times 10^{-3}$	0.01
8.	30.75	0.50	0.04	$0.81 \times 10^{-3}$	$2.41 \times 10^{-3}$	$1.99 \times 10^{-3}$	0.01
9.	17.27	0.31	0.02	$0.27 \times 10^{-3}$	$0.94 \times 10^{-3}$	$0.91 \times 10^{-3}$	$4.47 \times 10^{-3}$
10.	10.85	0.09	0.01	$8.06 \times 10^{-5}$	$0.34 \times 10^{-3}$	$0.29 \times 10^{-3}$	$2.07 \times 10^{-3}$
11.	9.22	0.07	0.01	$5.37 \times 10^{-5}$	$0.22 \times 10^{-3}$	$0.22 \times 10^{-3}$	$1.85 \times 10^{-3}$
12.	8.18	0.06	$4.37 \times 10^{-3}$	$5.37 \times 10^{-5}$	$0.18 \times 10^{-3}$	$0.17 \times 10^{-3}$	$1.15 \times 10^{-3}$
13.	8.04	0.06	$4.28 \times 10^{-3}$	$5.37 \times 10^{-5}$	$0.17 \times 10^{-3}$	$0.16 \times 10^{-3}$	$1.03 \times 10^{-3}$
14.	7.87	0.05	$3.74 \times 10^{-3}$	$2.69 \times 10^{-5}$	$9.86 \times 10^{-5}$	$0.13 \times 10^{-3}$	$0.74 \times 10^{-3}$
15.	7.79	0.05	$3.64 \times 10^{-3}$	$2.69 \times 10^{-5}$	$9.86 \times 10^{-5}$	$0.12 \times 10^{-3}$	$0.44 \times 10^{-3}$
16.	7.73	0.04	$3.59 \times 10^{-3}$	$2.69 \times 10^{-5}$	$9.86 \times 10^{-5}$	$0.12 \times 10^{-3}$	$0.44 \times 10^{-3}$
17.	7.00	0.01	$1.35 \times 10^{-3}$	0.00	$3.74 \times 10^{-5}$	$5.14 \times 10^{-5}$	$1.80 \times 10^{-3}$
18.	6.28	$2.70 \times 10^{-3}$	$0.59 \times 10^{-3}$	0.00	$2.04 \times 10^{-5}$	$1.84 \times 10^{-5}$	$8.20 \times 10^{-5}$

Table 9.3: Efficiencies of Selection Criteria

**S17** SP5 Tau Signal Decays in Tau MC; **T** SP5 Generic Tau MC; **Data** Runs 1-3 Data; **uds** SP5 uds MC; **b0b0** SP5 b0b0 MC; **cc** SP5 cc MC;

# Chapter 10

## Monte Carlo Corrections and the $K_S^0$ Mass Spectrum

The BaBar detector simulation does not describe the data adequately. Therefore several corrections to the MC are applied as follows so that the simulation describes the data:

- Corrections to the PID selectors in the MC;
- Corrections for the tracking efficiency;
- Corrections for the  $K_S^0$  selection efficiency.

The plots in the previous chapter all have the MC weights applied. If the weight for an effect is the same for  $\tau^+$  and  $\tau^-$  decays then the weights need not be applied to an asymmetry measurement because they cancel out.

## 10.1 PID Efficiency Corrections

Each event uses both the electron LikelihoodTight and Pion LikelihoodVeryTight selectors. The weight used for each track in each event is determined by the particle's momenta, theta and phi coordinates using the SP5 data/MC ratio tables for the selectors used in the analysis [63]. The total correction in an event is the product of the correction for each selector used in the event.

## 10.2 $K_S^0$ Efficiency Corrections

The standard  $K_S^0$  efficiency corrections [64] method is used in this analysis. The  $K_S^0$  reconstruction efficiency is binned in transverse momentum ( $P_T$ ), polar angle ( $\theta_{LAB}$ ) and transverse decay length ( $d_{XY}$ ). The correction factor for a given bin is the ratio of the number of  $K_S^0$  in a MC control sample to the number of  $K_S^0$  in a data control sample normalised to the correction factor in the first bin of  $d_{XY}$  which is 1.00 because for  $d_{XY} < 15$  mm the data and MC agree. The global correction is then

$$C_{orr} = \frac{1}{H_{Tot}} \sum_{ijk} H_{ijk} C_{ijk} \quad (10.1)$$

where  $H_{Tot} = \sum_{ijk} H_{ijk}$ ,  $C_{ijk}$  is the correction factor in bin  $ijk$  and  $H_{ijk}$  is the number of events in the MC in bin  $ijk$  in this analysis. This gives a global correction of 0.976. In addition a correction to the  $K_S^0$  line shape is also calculated where the efficiencies in data and MC are determined by numerical integration of the  $K_S^0$  mass spectrum in between the edges of the mass window used in this analysis. This gives a correction of 0.962. A global correction is applied which is the product of these

two corrections.

### 10.3 Tracking Efficiency Corrections

Both the tag track and bachelor pion track are required to pass GTVL. The Tracking Efficiency Task Force have estimated [65] a correction of 0.995 should be applied to each track passing GTVL.

### 10.4 Total Correction

The total global correction for each event is therefore the product of the tracking and  $K_S^0$  corrections. In addition the PID correction is applied by event by event (i.e it is different for each event considered).

### 10.5 Summary

Corrections have been applied to the MC so that it describes the data adequately. Global corrections are applied for tracking efficiency differences and  $K_S^0$  selection efficiency differences. Event by event corrections are applied to account for differences in particle identification efficiency between the data and MC.

## 10.6 The $K_S^0\pi$ Mass Spectrum

After applying the PID weights and efficiency corrections the  $K_S^0\pi$  mass spectrum is plotted. There is reasonable agreement generally although excess data is observed in the 1400 MeV area of the spectrum. This is suspected to be due to tau decays into as yet unobserved (in tau decays)  $K^*$  resonances which could be scalar or vector. [66]

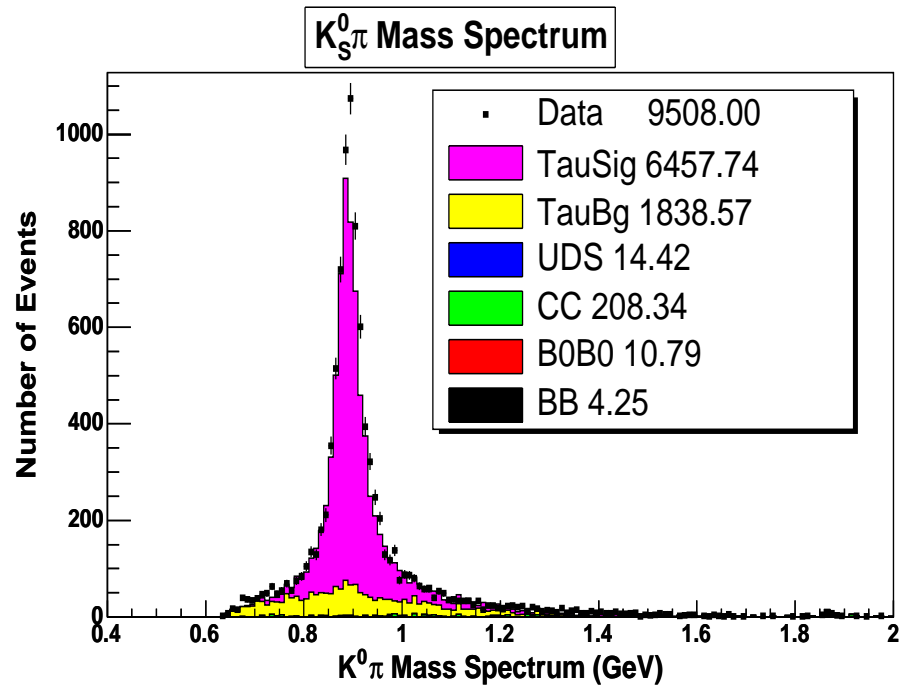


Figure 10.1: The  $K_S^0\pi$  mass spectrum with all cuts applied.

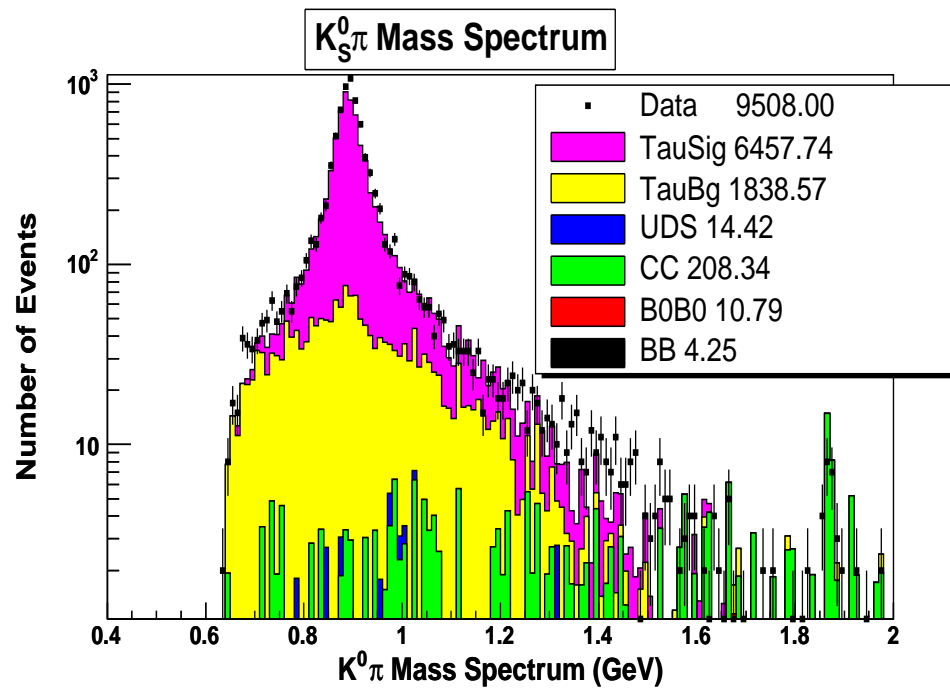


Figure 10.2: The  $K_S^0\pi$  mass spectrum with all cuts applied.

# Chapter 11

## CP Observable

To observe a CP violating effect one can in general construct a CP odd observable. An even better measurement may be done by constructing an observable that has a minimal statistical error by construction. This was described in Chapter 5.

This observable can be calculated for each signal event and this is described in Appendix A.

The coupling of the Higgs boson,  $\Im\Lambda$ , is not known. Each CP odd term has a factor of  $\Im\Lambda$  and so this is factored out and  $\epsilon$  is given by

$$\epsilon = \frac{P_{odd}(1)}{P_{even}} \quad (11.1)$$

where

$$P_{odd}(\Im\Lambda) = \Im\Lambda P_{odd}(1). \quad (11.2)$$

The sensitivity to CP violation is unaffected by scaling by a constant factor. The

mean of the observable is then easily calculated from the events in the data.

The mean may be formulated

$$\langle \epsilon \rangle = \int \frac{P_{odd}(1)}{P_{even}} \times [P_{even} + P_{odd}(\mathfrak{S}\Lambda)] DLIPS \quad (11.3)$$

where P is the probability density. The average may be approximated by (assuming small  $\mathfrak{S}\Lambda$ )

$$\langle \epsilon \rangle = C_1 \mathfrak{S}\Lambda + C_3 \mathfrak{S}\Lambda^3 \quad (11.4)$$

The CP violation can be seen by plotting  $\langle \epsilon^+ \rangle$  and  $\langle \epsilon^- \rangle$  against the  $K_S^0 \pi$  mass for a Monte Carlo sample with  $\mathfrak{S}\Lambda$  equal to unity.. These are

$$\langle \epsilon^\pm \rangle = \frac{\sum_i \epsilon_i^\pm}{N^\pm} \quad (11.5)$$

where  $\epsilon_i$  is the observable for event  $i$  with signal hemisphere charge  $\pm$  and  $N$  is the number of events. Figure 11.1 illustrates the observable becomes largest in the region 0.9 to 1.5 GeV and therefore this region is defined to be the signal region from which the measurement will be done.

The parameters  $C_1$  and  $C_3$  may be extracted by generating Monte Carlo samples with different values of  $\mathfrak{S}\Lambda$  in the range -1 to +1. This is done using the GeneratorsQA package to analyse events generated with kk2f and TAUOLA. TAUOLA is modified to simulate CP violating  $K^*$  decays by including a vector current with the charged Higgs decaying to the  $K^*(1430)$  resonance. This is illustrated in Figure 11.2 where  $\langle \epsilon \rangle$  is plotted against  $\mathfrak{S}\Lambda$ .  $\langle \epsilon \rangle$  is given by

$$\langle \epsilon \rangle = \frac{\sum_i \epsilon_i^+ - \sum_j \epsilon_j^-}{N^+ + N^-} \quad (11.6)$$

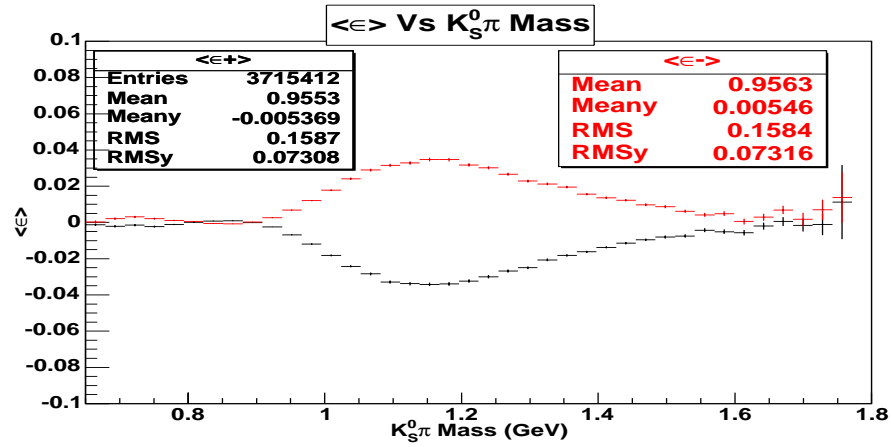


Figure 11.1:  $\langle \epsilon \rangle$  Vs  $K_S^0 \pi$  Mass for  $\Im\Lambda = 1$  (Red represents  $\tau^-$  decays and black  $\tau^+$  decays)

where  $i$  runs over events with a net positive charge in the signal hemisphere and  $j$  over events with a net negative charge in the signal hemisphere. For each MC sample (i.e each value of  $\Im\Lambda$ ) the random seed is changed.

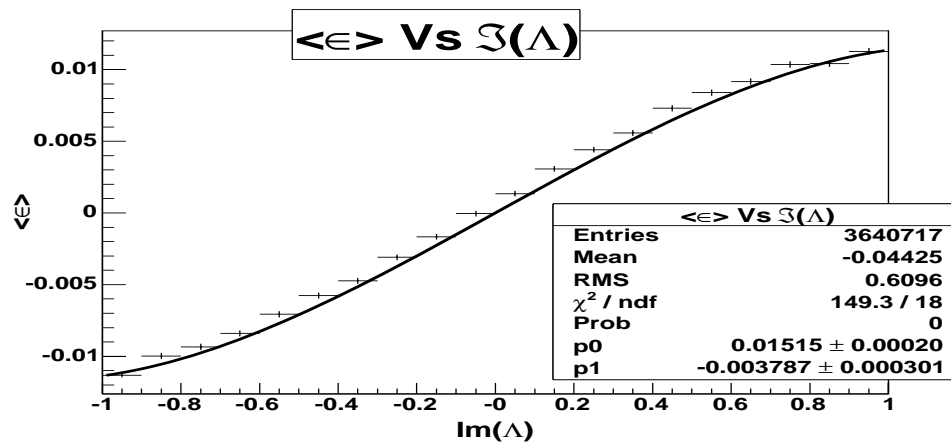


Figure 11.2:  $\langle \epsilon \rangle$  Vs  $\Im\Lambda$

## 11.1 Summary

The TAUOLA MC software has been modified to include CP violating tau decay modes. This is used to parameterise the relationship between  $\mathfrak{S}\Lambda$  and the optimal observable which is calculated using measured particle 4-vectors.

# Chapter 12

## Systematic Checks

Here checks for biases and the systematic errors are described. To obtain an estimate of the true observable the asymmetry due to the background must be subtracted off; this is estimated using MC. If the MC weights for  $\tau^+$  and  $\tau^-$  in the background are not the same then there is a systematic error. If they are the same they trivially cancel and need not be considered. However because the plots comparing data-MC in the thesis include MC weighting the systematic error on the MC weights used in the plots is also quoted to allow proper interpretation of the data-MC comparison.

### 12.1 Systematic Uncertainties on PID Weights

The Monte Carlo has been corrected so that the particle selectors in the Monte Carlo match the performance of the selectors in the data. The errors on the weights of the electron LikelihoodTight and pion LikelihoodVeryTight particle selectors are combined in quadrature to get the error for each event. To estimate the error due

to the PID corrections scheme the statistically-weighted mean is calculated and the error on that is taken as a measure of the systematic error on the MC correction.

The mean is thus

$$\langle c \rangle = \frac{1}{\sum_i 1/s_i^2} * \sum_i \frac{c_i}{s_i^2} \quad (12.1)$$

where  $\langle c \rangle$  is the mean correction,  $s_i$  is the error on the correction in bin  $i$  due to the statistics in that bin and  $c_i$  is the correction in bin  $i$ . The error in  $\langle c \rangle$  is

$$\sigma_{\langle c \rangle} = \sqrt{\frac{1}{\sum_i 1/s_i^2}} \quad (12.2)$$

The mean and its error is  $0.995 \pm (0.639 \times 10^{-4})$  Estimating this separately for  $\tau^-$  and  $\tau^+$  events gives  $0.995 \pm (0.848 \times 10^{-4})$  and  $0.994 \pm (0.964 \times 10^{-4})$  respectively.

## 12.2 Systematic Uncertainties on $K_S^0$ Corrections

The systematic uncertainty on the correction used in data-MC plots is derived from the statistical error on the correction. This can be calculated taking the error on  $H_{ijk}$  (the number of events in the MC in this analysis in bin  $ijk$ ) to be

$$\sqrt{H_{ijk}} \quad (12.3)$$

and the error on an individual bins correction is

$$\sigma_{C_{ijk}} = C_{ijk} \sqrt{\left(\frac{\sigma_{N_{ijk}}}{N_{ijk}}\right)^2 + \left(\frac{\sigma_{M_{ijk}}}{M_{ijk}}\right)^2} \quad (12.4)$$

where  $N_{ijk}$  is the number of events in the data control sample in bin  $ijk$  and  $M_{ijk}$  is the number of events in the MC control sample in bin  $ijk$ . The error on the global

correction is therefore

$$\sigma_C = \frac{1}{H_{Tot}} \sqrt{\sum_{ij} \left( \sum_k H_{ijk} C_{ijk}^2 + \sum_{k \neq 1} (H_{ijk} \sigma_{C_{ijk}})^2 + \sigma_{C_{ij1}}^2 \left( \sum_{k \neq 1} H_{ijk} C_{ijk} \right)^2 \right)} \quad (12.5)$$

The error on the  $K_S^0$  efficiency correction factor is 0.013 which includes a 1% systematic uncertainty due to the lineshape correction. The efficiency correction is not quite the same for decays with  $K^{*+}$  and  $K^{*-}$  and so the respective corrections and errors are  $0.975 \pm 0.014$  and  $0.976 \pm 0.014$ . The respective mass corrections are 0.962 and 0.963.

## 12.3 Systematic Uncertainty on $K_S^0$ Candidate Selection

There is an additional systematic error [65] because tracks with DCH hit requirements are more likely to form a  $K_S^0$  candidate that passes the mass cuts. To estimate this first the number of events selected in MC is taken and then recalculated using the GoodTracksLoose (GTL) corrections for every track that passes the GTL selection criteria and the difference is taken.

$$D = N_{Sel} - N_{Sel}^{GTL}. \quad (12.6)$$

The GoodTracksLoose requirements are identical to that of GoodTracksVeryLoose with the additional requirement that the number of DCH hits is at least 12.

Then the sample is split into four sub-samples as follows:

1.  $K_S^0$  candidates without the final mass cut applied that have both daughter tracks pass GTL (A1).
2.  $K_S^0$  candidates in sample A1 that pass the final mass cut.(A2)
3.  $K_S^0$  candidates without the final mass cut applied that have one or more daughter tracks fail GTL (B1)
4.  $K_S^0$  candidates in sample B1 that pass the final mass cut.(B2)

Finally

$$\sigma_{DCH} = D * \left( 1 - \frac{\frac{B2}{A2}}{\frac{B1}{A1}} \right) \quad (12.7)$$

is calculated. The systematic error is then  $\frac{\sigma_{DCH}}{N_{Sel}}$  where  $N_{Sel}$  is the number of events selected in MC and is evaluated as 0.15%. For  $\tau^+$  this is 0.17% and for  $\tau^-$  0.13%.

## 12.4 Errors on Tracking Efficiency Corrections

The signal events have fewer than five tracks in them and therefore the systematic error due to the GTVL corrections, as estimated by the Tracking Efficiency Task Force [65], is 1.2% per track. The corrections are identical for  $\tau^+$  and  $\tau^-$  decays and so there is no systematic error on the asymmetry due to these weights.

## 12.5 Errors due to background subtraction

The branching fractions used in the tau MC have uncertainties associated with them. Therefore when the background asymmetry  $A_{Background}$  is calculated the number of

events subtracted must be given an error

$$\Delta N_{\tau}^{BG} = \sqrt{\sum_i w_i \frac{\sigma_i}{Br_i}} \quad (12.8)$$

where  $w_i$  is the fraction of mode  $i$  found in the selected tau MC sample,  $Br_i$  is the PDG 2002 [1] branching fraction and  $\sigma_i$  is the error on  $Br_i$ .

$\Delta N_{\tau}^{BG}$  is found to be  $3.46\% * N_{BKG}$ . There is no systematic on the asymmetry due to this however because the error on the branching fractions are the same for  $\tau^+$  and  $\tau^-$  decays.

## 12.6 Uncertainties due to Selection Criteria

The neutral energy spectrum has poor data-MC agreement in the shape of the spectrum. To estimate the error due to this the cut is turned off and  $\langle \epsilon_{true} \rangle$  recalculated.  $\Delta \langle \epsilon \rangle / \langle \epsilon \rangle$  is 0.44 where  $\Delta \langle \epsilon \rangle$  is the shift in  $\langle \epsilon_{true} \rangle$  when the cut is turned off.

The cosine of the theta component of the missing momentum vector was also observed to have significant differences between data and MC. Therefore the same procedure is applied and  $\Delta \langle \epsilon \rangle / \langle \epsilon \rangle$  is 1.17.

## 12.7 Errors on $c_1$

The value of  $c_1$  is estimated from the MC simulation. The  $K_{1430}^*$  scalar resonance influences this, yet its couplings and parameters are poorly known. Therefore the mass and width of the resonance are varied by  $\pm 5\sigma$  and the variation in  $c_1$  is taken as the systematic error due to this. The maximum deviation from the value of  $c_1$  due to varying the parameters used in this analysis is 7.79%. Therefore a systematic uncertainty of  $7.79\% * c_1$  is used. In addition the statistical error on  $c_1$  is included in the systematic uncertainty.

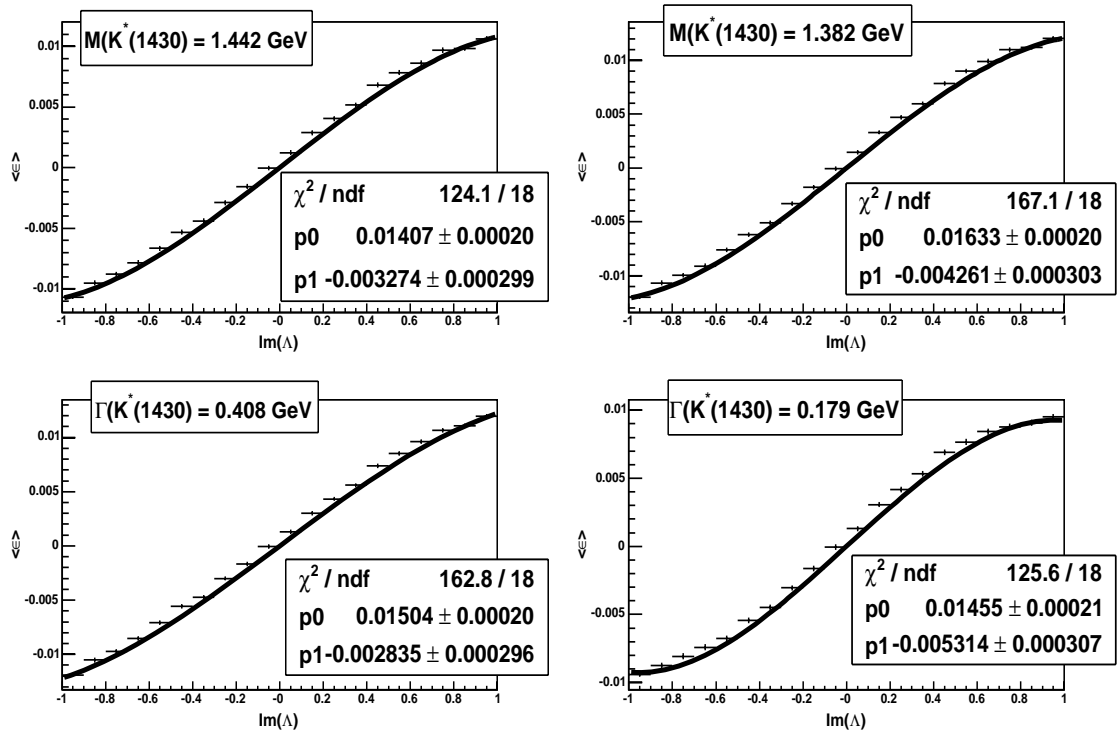


Figure 12.1: Effect of varying  $K^*(1430)$  parameters

## 12.8 Summary

Systematic errors are applied to  $\langle \epsilon \rangle$  due to uncertainties in the corrections applied to the MC. These are summarised in Table 12.1. Table 12.2 shows the systematic uncertainties on the value of  $\mathfrak{S}(\Lambda)$ . The largest uncertainty is due to the statistical error on the background asymmetry, the Correction factor also contributes a sizable uncertainty mainly due to MC statistics (though the errors on the MC corrections give a small contribution here also). The uncertainty due to the selection criteria is also significant. The error due to the parameter  $c_1$  is small compared to the other uncertainties.

Systematic	Data-MC Correction
PID	$0.006 \times 10^{-2}$
Ks0Eff	0.0133
DCH	0.0015

Table 12.1: Summary of Systematic Errors on MC corrections

Systematic	$\Delta \langle \mathfrak{S}(\Lambda) \rangle / \langle \mathfrak{S}(\Lambda) \rangle$
Background Asymmetry	1.88
Error on Correction Factor	1.57
Selection Criteria	1.25
$c_1$	0.013

Table 12.2: Summary of Systematic Errors on  $\mathfrak{S}(\Lambda)$

# Chapter 13

## Measurement of CP Asymmetry

In the signal region the raw uncorrected  $\langle \epsilon \rangle$  is found to be  $(0.129 \pm 0.14)\%$ . First of all the asymmetry in the background modes is subtracted off.  $\langle \epsilon \rangle$  can be decomposed into signal and background components [67]

$$\langle \epsilon \rangle_{Obs} = \frac{\sum_i \epsilon_i + \sum_j \epsilon_j}{N_{Sig} + N_{Bkg}} \quad (13.1)$$

where  $\langle \epsilon \rangle_{obs}$  is the observed  $\langle \epsilon \rangle$ ,  $i$  is summed over signal events and  $j$  over background events,  $N_{Sig}$  is the number of signal events selected and  $N_{Bkg}$  is the number of background events selected. Ultimately an expression for

$$\langle \epsilon \rangle_{Sig} = \frac{\sum_i \epsilon_i}{N_{Sig}} \quad (13.2)$$

is sought and rearranging 13.1 this is

$$\langle \epsilon \rangle_{Sig} = \left( 1 + \frac{N_{Bkg}}{N_{Sig}} \right) \langle \epsilon \rangle_{Obs} - \frac{\sum_j \epsilon_j}{N_{Sig}}. \quad (13.3)$$

Using

$$\langle \epsilon \rangle_{Bkg} = \frac{\sum_j \epsilon_j}{N_{Bkg}} \quad (13.4)$$

the background subtracted  $\langle \epsilon \rangle$  is

$$\langle \epsilon \rangle_{Obs} + C \quad (13.5)$$

where  $C$  is the correction which is

$$(\langle \epsilon \rangle_{Obs} - \langle \epsilon \rangle_{Bkg}) \times \frac{N_{Bkg}}{N_{Sig}}. \quad (13.6)$$

The correction factor can be calculated from the MC and is  $(-0.083 \pm 0.099)\%$ . The error includes MC statistics, PID weight errors and  $K_S^0$  efficiency correction errors.

Finally  $\langle \epsilon_{True} \rangle$  is calculate using

$$\langle \epsilon_{True} \rangle = \langle \epsilon_{Obs} \rangle + C - \epsilon_{MC}^{Sig} \quad (13.7)$$

where  $\epsilon_{MC}^{Sig}$  is the mean value of  $\epsilon$  in the signal MC and takes account of any residual detector asymmetries; it is found to be  $(0.109 \pm 0.119)\%$ . Therefore  $\langle \epsilon_{True} \rangle$  is  $(-0.063 \pm 0.140 \pm 0.174)\%$  where the first error is the statistical error from the data and the second the systematic error. To get  $\mathfrak{S}\Lambda$  in the context of the MHDM the relation

$$\langle \epsilon_{True} \rangle = c_1 \mathfrak{S}\Lambda \quad (13.8)$$

where  $c_1$  is  $0.015 \pm 0.00020$ . Thus  $\mathfrak{S}(\Lambda)$  is  $-0.042 \pm 0.093 \pm 0.115$  where the first error is statistical and the second systematic which includes uncertainties due to  $c_1$ .

Therefore at 90 % C.L  $-0.284 < \mathfrak{S}(\Lambda) < 0.200$ .

# Chapter 14

## Conclusions

This thesis has first introduced the Standard Model of particle physics, followed by the possibility of CP asymmetries originating in physics not included in the Standard Model. The BaBar detector was then introduced along with the associated software necessary in a modern particle physics experiment. Studies of the TAUOLA and kk2f Monte Carlo packages were described, before finally the measurement of the imaginary part of the charged Higgs coupling in a MHDM model.

At 90% C.L. the imaginary part of the charged Higgs coupling in the MHDM is found to be  $-0.284 < \Im(\Lambda) < 0.200$  using the BaBar detector. This is the first independent measurement of this to be made and it is consistent with all previous measurements performed by the CLEO collaboration. The measurement in this thesis is compared with previous measurements in Figure 14.1 where the length of the line represents the allowed region of  $\Im\Lambda$  at 90% C.L. The correlated  $\tau$  to  $\rho$  decays analyses show an enhanced sensitivity with respect to the decay modes studied in this thesis.

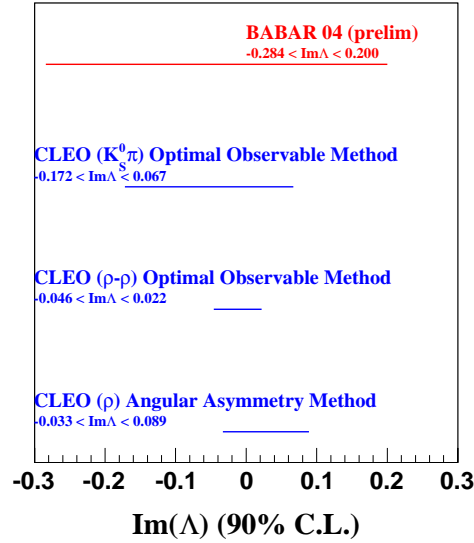


Figure 14.1: Summary of current measurements of  $\Im\Lambda$

The measurement presented in this thesis only uses electron-tagged data and this has fewer (around 2000 less) events than the number used in the CLEO analysis which made use of an electron-tagged sample, a muon-tagged sample and hadron-tagged sample. Collaborators from BaBar intend to repeat the analysis using the data taking in Runs 1 to 5, which will comprise around  $500 \text{ fb}^{-1}$  of data, and this should reduce the statistical errors on the measurement significantly.

*Annapurna, to which we had gone, is a treasure on which we should live the rest of our days. With this realisation we turn the page: a new life begins. There are other Annapurnas in the lives of men.*

Maurice Herzog, Annapurna

# Appendix A

## Calculation of CP Optimal Observable

The amplitude for the vector current is [68]

$$M_W = \frac{G_F}{\sqrt{2}} \bar{u}(k) \gamma_\mu (1 - \gamma_5) u(q) V_{sd} f_V Q^\mu \quad (\text{A.1})$$

where  $G_F$  is the Fermi constant, the  $\gamma$ s are the Dirac matrices,  $u$  is a Dirac spinor,  $q$  is the four-momentum of the tau,  $k$  is the four-momentum of the neutrino,  $V_{sd}$  is a CKM matrix element,  $f_V$  is the  $K^*(892)$  form factor and  $Q^\mu$  is given by

$$Q^\mu = \left[ (p_\pi - p_k)^\mu - \frac{m_\pi^2 - m_k^2}{(p_\pi + p_k)^2} (p_\pi + p_k)^\mu \right] \quad (\text{A.2})$$

where  $p_\pi$ ,  $p_k$ ,  $m_\pi$  and  $m_k$  are the pion and kaon momenta and masses. The scalar current is

$$M_H = \frac{G_F}{\sqrt{2}} \bar{u}(k) (1 - \gamma_5) u(q) \Lambda V_{sd} f_s M \quad (\text{A.3})$$

where  $\Lambda$  is the charged Higgs coupling,  $f_s$  is the  $K^*(1430)$  form factor and  $M$  is a dimensional quantity ( $1 \text{ GeV}/c^2$ ) providing overall normalisation. Thus the total amplitude is

$$M = \frac{G_F}{\sqrt{2}} V_{sd} [\bar{u}(k) \gamma_\mu (1 - \gamma_5) u(q) f_V Q^\mu + \bar{u}(k) (1 - \gamma_5) u(q) \Lambda V_{sd} f_s M] \quad (\text{A.4})$$

Squaring the matrix element gives

$$\begin{aligned} |M^2| = & \frac{G_F^2}{2} V_{sd}^2 [|f_V|^2 Q^\mu Q^\nu (q^\alpha \gamma_\alpha + m_\tau) \gamma_\mu (1 - \gamma_5) k^\rho \gamma_\rho \gamma_\nu (1 - \gamma_5) \\ & + |\Lambda|^2 |f_S|^2 M^2 (q^\alpha \gamma_\alpha + m_\tau) (1 - \gamma_5) k^\rho \gamma_\rho (1 + \gamma_5) \\ & + \Lambda f_S f_V^* M Q^\mu (q^\alpha \gamma_\alpha + m_\tau) \gamma_\mu (1 - \gamma_5) k^\rho \gamma_\rho (1 + \gamma_5) \\ & + \Lambda^* f_S^* f_V M Q^\mu (q^\alpha \gamma_\alpha + m_\tau) (1 - \gamma_5) k^\rho \gamma_\rho \gamma_\mu (1 - \gamma_5)] \end{aligned} \quad (\text{A.5})$$

where the relation for a particle  $A$ ,

$$u(A) \bar{u}(A) = q^\alpha \gamma_\alpha + m_A, \quad (\text{A.6})$$

is used. Using the standard trace relations  $|M|^2$  reduces to

$$\begin{aligned} & \frac{G_F^2}{2} V_{sd}^2 [2|f_V|^2 [2(q \cdot Q)(k \cdot Q) - (q \cdot k)Q^2] + 2|\Lambda|^2 |f_S|^2 M^2 (q \cdot k)] \\ & + 4\Re(\Lambda f_S f_V^*) M m_\tau (Q \cdot k) \end{aligned} \quad (\text{A.7})$$

The CP conjugate amplitude,

$$\bar{M} = \frac{G_F}{\sqrt{2}} V_{sd} [\bar{v}(q) \gamma_\mu (1 - \gamma_5) v(k) (-1) f_V Q^\mu + \bar{v}(q) (1 - \gamma_5) v(k) \Lambda^* V_{sd} f_s M], \quad (\text{A.8})$$

similarly gives when squared

$$\begin{aligned} & \frac{G_F^2}{2} V_{sd}^2 [2|f_V|^2 [2(q \cdot Q)(k \cdot Q) - (q \cdot k)Q^2] + 2|\Lambda|^2 |f_S|^2 M^2(q \cdot k)] \\ & + 4\Re(\Lambda f_S f_V^*) M m_\tau(Q \cdot k) \end{aligned} \quad (\text{A.9})$$

Therefore the matrix element squared for  $\tau^\pm \rightarrow K^0 \pi^\pm \nu_\tau$  is

$$\begin{aligned} & \frac{G_F^2}{2} V_{sd}^2 [2|f_V|^2 [2(q \cdot Q)(k \cdot Q) - (q \cdot k)Q^2] + 2|\Lambda|^2 |f_S|^2 M^2(q \cdot k)] \\ & + 4\Re(\Lambda^+ f_S f_V^*) M m_\tau(Q \cdot k) \end{aligned} \quad (\text{A.10})$$

where for the  $\tau^-$  decay  $\Lambda^+ \equiv \Lambda$  and for the  $\tau^+$  decay  $\Lambda^+ \equiv \Lambda^*$ . Finally this is separated into CP even and odd components making use of the relations

$$\Re(\Lambda^+ f_S f_V^*) = \Re(\Lambda) \Re(f_S f_V^*) \mp \Im(\Lambda) \Im(f_S f_V^*) \quad (\text{A.11})$$

and

$$\Im(\Lambda^+ f_S f_V^*) = \Re(\Lambda) \Im(f_S f_V^*) \pm \Im(\Lambda) \Re(f_S f_V^*), \quad (\text{A.12})$$

and so  $|M|^2$  is

$$\begin{aligned} & \frac{G_F^2}{2} V_{sd}^2 [2|f_V|^2 [2(q \cdot Q)(k \cdot Q) - (q \cdot k)Q^2] + 2|\Lambda|^2 |f_S|^2 M^2(q \cdot k)] \\ & + 2\Re(\Lambda) \Re(f_S f_V^*) M m_\tau(Q \cdot k) - 2\Im(\Lambda^+) \Im(f_S f_V^*) M m_\tau(Q \cdot k). \end{aligned} \quad (\text{A.13})$$

The optimal observable is

$$\epsilon = \frac{-2\Im(\Lambda^+) \Im(f_S f_V^*) M m_\tau(Q \cdot k)}{[2|f_V|^2 [2(q \cdot Q)(k \cdot Q) - (q \cdot k)Q^2] + 2|\Lambda|^2 |f_S|^2 M^2(q \cdot k)] + 2\Re(\Lambda) \Re(f_S f_V^*) M m_\tau(Q \cdot k)} \quad (\text{A.14})$$

To measure  $\epsilon$  it must be expressed in terms of experimentally measurable quantities [68]. The quantities  $(q \cdot Q)$  and  $(k \cdot Q)$  are given by

$$-2|p_\pi||p'_\tau|\cos\psi\cos\beta \quad (\text{A.15})$$

where  $\cos\psi$  is the angle between the pion and the hadronic system,  $\cos\beta$  is the angle between the  $\tau$  and the hadronic system and  $p'_\tau$  is the tau momentum in the  $K_S^0\pi$  rest frame. The quantity  $(q \cdot k)$  is

$$m_\tau^2 - E'_\tau m_h \quad (\text{A.16})$$

where  $E'_\tau$  is the tau energy (which is approximated by the beam energy in the c.m frame) in the  $K_S^0\pi$  rest frame and  $m_h$  is the mass of the  $K_S^0\pi$  system. The third quantity  $Q^2$  is

$$2m_\pi^2 + 2m_K^2 - m_h^2(1 + D^2) \quad (\text{A.17})$$

where  $D$  is defined as

$$D \equiv \frac{m^2 - m_K^2}{m_h^2} \quad (\text{A.18})$$

# Appendix B

## Definitions of Nano Level TagBits

The subscripts 1 and 2 refer to the two highest momentum tracks in the event where track 1 has the higher momentum.

BGFMultiHadron:

- At least 3 Charged Tracks
- $R2 < 0.98$

BGFNeutralHadron:

- $R2 < 0.95$
- (No more than 2 GTVL and at least 2 unmatched EMC clusters AND 3 50 MeV neutral candidates) OR (No more than 1 GTVL and at least 2 unmatched EMC clusters AND 4 50 MeV neutral candidates with  $-0.75 < \cos \theta < 0.95$ )

OR (No GTVL and at least 3 unmatched EMC clusters AND 6 50 MeV neutral candidates)

BGFTau:

- Exactly two Charged Tracks
- Net Charge = 0
- $(P_1 + P_2) < 9$  GeV
- $(E_1 + E_2) < 5$  GeV
- $\frac{E_1}{P_1}$  OR  $\frac{E_2}{P_2} < 0.8$
- $E_{CM} - P_1 - P_2 > 0$
- $\frac{Pt_1 + Pt_2}{E_{CM} - P_1 - P_2} > 0.07$

BGFMuMu:

- $P_1 > 4$  GeV
- $P_2 > 2$  GeV
- $\theta_1 < 2.8$  radians
- $\theta_2 > 3.5$  radians
- $(E_1 + E_2) < 2$  GeV

BGFTwoProng:

- Exactly two Charged Tracks
- Net Charge = 0
- $(P_1 \text{ OR } P_2) > 1 \text{ GeV}$
- $(E_1 \text{ AND } E_2) < 3 \text{ GeV}$
- $|\cos \theta_1 + \cos \theta_2| > 0.1$
- $\cos \theta_1 > -0.75$
- $P_1 \text{ OR } P_2 > 4 \text{ GeV OR } |Pt_1 - Pt_2| \geq 0.3$

# Bibliography

- [1] K. Hagiwara et al., Phys. Rev. D 66 (2002).
- [2] S. Anderson et al., Phys.Rev.Lett 81 (1998) 3823, hep-ex/9805027.
- [3] H. Hayashii, Nucl.Phys.B(Proc.Suppl) 98 (2001) 141.
- [4] J. Williams, Tauuser - Run 1-3 Data and SP5 Production Ntuples, 2004, BAD 898, Version 2.
- [5] M.B. Gavela et al., Nucl. Phys. N (1994).
- [6] A. Stahl, Physics with Tau Leptons (Springer, 2000).
- [7] M.L. Perl et al., Phys. Rev. Lett. 35 (1975) 1489.
- [8] F. Halzen and A.D. Martin, Quarks and Leptons: An Introductory Course in Modern Particle Physics (Wiley, New York, USA, 1984).
- [9] G. Arnison et al., Phys. Lett. B (1983) 103.
- [10] G. Arnison et al., Phys. Lett B (1983).
- [11] J.W. Cronin et al., Phys. Rev. Lett 13 (1964) 138.
- [12] T.T. Wu and C.N. Yang, Phys. Rev. Lett 13 (1964) 380.

- [13] E. Leader and E. Predazzi, *An Introduction to Gauge Theories and Modern Particle Physics*, Second ed. (Cambridge University Press, 1996).
- [14] B. Aubert et al., *Phys.Rev.Lett* 89 (2002).
- [15] K. Abe et al., *Lepton-Photon Conference* (2003).
- [16] A. Ritto, *Theories of BaryoGenesis* (Summer School in High Energy Physics and Cosmology, Miramare-Triests, Italy, 1998), hep-ph/9807454.
- [17] S. Choi, K. Hagiwara and M. Tanabashi, *Phys. Rev. D* 52 (1993) 1614.
- [18] S. Eidelman et al., *Phys. Lett. B* 592 (2002) 1.
- [19] S. Anderson et al., *Phys.Rev.D* 64 (2001).
- [20] G. BonVicini et al., *Phys.Rev.Lett* 88 (2001) 111803, hep-ex/0111095.
- [21] B. Aubert et al., *Nucl.Instrum.Meth A*479 (2002) 1, hep-ex/0105044.
- [22] Particle Data Group, K. Hagiwara et al., *Phys. Rev. D*66 (2002) 010001.
- [23] M. Weaver, Operational overview,  
<http://www.slac.stanford.edu/BFROOT/www/Organization/CollabMtgs/2004/detFeb04/Sat4/weaver.pdf>.
- [24] P. Billoir, *Nucl. Instr. Meth A*225 (1984) 352.
- [25] LST Team, A Barrel IFR Instrumented with Limited Streamer Tubes,  
<http://www.slac.stanford.edu/BFROOT/www/Detector/LST/documentation/LST-prop-A4-May30-ajss.pdf>.
- [26] DCT Upgrade Team, L1 Drift-Chamber Trigger Upgrade Conceptual Design Requirements, <http://www.slac.stanford.edu/BFROOT/www/Detector/Trigger/upgrade/cdr/requirements.pdf>.

- [27] J. Williams, Workbook for BaBar Offline Users,  
<http://www.slac.stanford.edu/BFROOT/www/doc/workbook/workbook.html>.
- [28] <http://www.redhat.com/>.
- [29] S. Microsystems, Solaris Common Desktop Environment: Advanced Users and System Administrators Guide (Sun Microsystems, 2002).
- [30] <http://www.openafs.org/>.
- [31] H. Stern, Managing NFS and NIS (O'Reilly UK, 2001).
- [32] <http://www.cvshome.org>.
- [33] S. Rahatlou, Elf: Babar Event Reconstruction Algorithm, 2004,  
[http://www.slac.stanford.edu/BFROOT/www/Computing/Documentation/CM2/intro/030\\_run\\_executables/Elf.html](http://www.slac.stanford.edu/BFROOT/www/Computing/Documentation/CM2/intro/030_run_executables/Elf.html).
- [34] <http://www.objectivity.com>.
- [35] D. Kirkby et al.,  
<http://www.slac.stanford.edu/BFROOT/www/Computing/Offline/Kanga/index.html>.
- [36] P. Elmer,  
<http://www.slac.stanford.edu/BFROOT/www/Computing/Documentation/CM2/intro/>.
- [37] J. Williams,  
<http://www.slac.stanford.edu/BFROOT/www/doc/workbook/framework1/framework1.html>.
- [38] S. Banerjee, Some Info About TauNtuple Package, 2004,  
<http://www.slac.stanford.edu/BFROOT/www/Physics/Analysis/tauqed/TauNtuple/index.html>.

- [39] <http://tcl.sourceforge.net/>.
- [40] D. Lange and A. Ryd, CHEP 1998 Proceedings, 1998.
- [41] T. Sjöstrand, *Comp.Phys.Commun* 82 (1994) 74.
- [42] S. Jadach, B. Ward and Z. Was, *Comp.Phys.Commun* 130 (2000) 260.
- [43] D. Wright, [http://www.slac.stanford.edu/BFROOT/www/Computing/Offline/Simulation/web/simover/simover\\_main.html](http://www.slac.stanford.edu/BFROOT/www/Computing/Offline/Simulation/web/simover/simover_main.html).
- [44] S. Agostinelli et al., *Nuc.Meth. and Instr. A506* (2003) 250 .
- [45] S. Jadach and Z. Was, *Comp.Phys.Commun* 85 (1995) 453.
- [46] S. Jadach, B. Ward and Z. Was, *Eur.Phys.J C22* (2001) 423, hep-ph/9905452.
- [47] S. Jadach, B. Ward and Z. Was, *Phys.Rev.D* 63 (2001) 113009, hep-ph/0006359.
- [48] D. Bardin et al., *Comput. Phys. Commun* 59 (1990) 313.
- [49] P. Golonka et al., Submitted to *Comp.Phys.Commun* (2004), hep-ph/0312240.
- [50] T. Sjöstrand et al., *Pythia 6.3: Physics and manual*, 2003, hep-ph/0308153.
- [51] S. Jadach, <http://jadach.home.cern.ch/jadach/KKindex.html>.
- [52] R. Barlow, M. Hodgkinson and J. Williams, *Second Class Currents in Tau Decays*, 2002, BAD 327 Version 3.
- [53] G. Lafferty and J. Williams, *Study of the Decay  $\tau^- \rightarrow \pi^- \pi^- \pi^+ \pi^0 \pi^0$* , 2004, BAD 900 Version 4.
- [54] R. Sobie, *Study of Five Prong Tau Decays*, 2004, BAD 887 Version 3.

- [55] M. Roney, 2000, <http://babar-hn.slac.stanford.edu:5090/HyperNews/get/TauQED/279/2.html>.
- [56] M. Hodgkinson, TauQED AWG kk2f Monte Carlo Webpage, 2004, <http://www.slac.stanford.edu/>
- [57] S. Banerjee, M. Roney and M. Hodgkinson, Nano and Micro Preselection in  $e^-e^+ \rightarrow \mu^-\mu^+$  and  $e^-e^+ \rightarrow \tau^-\tau^+$  events, BAD 739 Version 2.
- [58] Background Filter Information in the Nano(Tag) Database, 2002, [http://www.slac.stanford.edu/BFROOT/www/doc/workbook/nanomicro/v8.6/Nano/BGF+DigiF\\_Flags.html](http://www.slac.stanford.edu/BFROOT/www/doc/workbook/nanomicro/v8.6/Nano/BGF+DigiF_Flags.html).
- [59] ROOT: An Object-Oriented Data Analysis Framework, <http://root.cern.ch>.
- [60] T. Brandt, Likelihood Based Electron Identification, 2002, <http://hep.phy.tu-dresden.de/tbrandt/electronid/>.
- [61] A. Roodman, A Short Description of the LH Selectors, [http://www.slac.stanford.edu/BFROOT/www/Physics/Tools/Pid/Hadrons/Description\\_of\\_the\\_LH\\_selectors.html](http://www.slac.stanford.edu/BFROOT/www/Physics/Tools/Pid/Hadrons/Description_of_the_LH_selectors.html).
- [62] F. Martinez-Vidal, Vertexing/kinematic fitting user's guide, <http://www.slac.stanford.edu/BFROOT/www/Physics/Tools/Vertex/VtxGuide/vtxguideold.html>.
- [63] T. Brandt, The PID Table Inventory, 2004, <http://www.slac.stanford.edu/BFROOT/www/Physics/Tools/Pid/PidTables/inventory.html>.

- [64] B. Bhuyan, Ks Reconstruction Efficiency Study using Series 12-Data and SP5 MC, 2004, [http://www.slac.stanford.edu/BFROOT/www/Physics/TrackEfficTaskForce/Recipe/R12/KsEff\\_R12.html](http://www.slac.stanford.edu/BFROOT/www/Physics/TrackEfficTaskForce/Recipe/R12/KsEff_R12.html).
- [65] T. Allmendinger and E. Varnes, The Tracking Efficiency Task Force 2004, <http://www.slac.stanford.edu/BFROOT/www/Physics/TrackEfficTaskForce/TrackingTaskForce-2004.html>.
- [66] A. Lyon, Studies of the Strange Hadronic  $\tau$  Decay  $\tau^- \rightarrow K_S^0 \pi^- \nu_\tau$  using the BaBar Detector, PhD thesis, University of Manchester, Manchester, UK, 2004.
- [67] J. Allison, 2004, Private communication by email.
- [68] Y. Maravin, Search for CP Violation in Tau Lepton Decays, PhD thesis, Southern Methodist University, 2002.